Asteroid gravity field estimation below the Brillouin sphere

MSc Thesis

S.J.H. Spee

Asteroid gravity field estimation below the Brillouin sphere

MSc Thesis

by

S.J.H. Spee

in partial fulfillment of obtaining the degree of Master of Science
at the Delft University of Technology,
to be defended publicly on Tuesday March 8, 2022 at 02:00 PM.

Student number:	5040108	
Thesis committee:	Dr. ir. B.C. Root,	TU Delft, supervisor
	Dr. ir. E. Mooij,	TU Delft, chair/supervisor
	Dr. ir. S. Speretta	TU Delft, external examiner

Cover image: NASA/JPL

Abstract

The history of space exploration shows a widespread interest in asteroids. These small bodies were visited by multiple spacecrafts made by different space organizations through time. The asteroids give us information about the history of the solar system, due to their unchanged state since the early beginning of the Solar System. In the future, these rocky bodies could provide resources for use on Earth or during human spaceflight. Besides these benefits, so-called near-Earth asteroids can be of danger by the possibility of collision. In the history of Earth, asteroid impacts had large consequences for life on Earth.

During missions towards asteroids, navigation is challenged by the gravity field of the asteroid. Asteroids are relatively small and often have a very irregular shape. The relatively small and irregular gravity field of the asteroid on the spacecraft, makes the acceleration difficult to predict. Therefore, gaining knowledge about this gravity field during the mission improves the safety of the spacecraft.

Gravity fields of celestial bodies often modeled and estimated using the spherical harmonics model. This model has the disadvantaged that its convergence is limited to the body's circumscribing sphere, called the Brillouin sphere. Because of their often irregular shape, this model is not suitable for orbits close to the asteroid, reaching inside this reference sphere. To eliminate this problem, the alternative mascon (mass concentration) gravity model is implemented in an extended Kalman filter (EKF). This model distributes point-masses along the asteroid's body. The gravitational parameters of each defined mascon are estimated by the EKF using noisy position measurements.

To test the performance of the EKF, a spacecraft is simulated in an asteroid environment. For this simulator, the polyhedron gravity model using the 433 Eros shape model is defined as the real-world gravity field. This high-precision and non-diverging gravity field model assumes a constant density in the asteroid. The model is adjusted such that it also can include density differences inside the asteroid shape by dividing the surface shape model into numerous volume elements. Each element is assigned a density according to the smoothing Mátern Covariance function, which depends on the Euclidean distance between the elements.

The EKF is capable of handling asteroids with a heterogeneous density distribution with the same accuracy as for homogeneous asteroids. Its performance depended highly on the chosen mascon positions, as point masses can be highly correlated. The EKF can estimate the gravity field as accurate as the spherical harmonics degree 8 using noisy position measurements with 10 meter standard deviation.

Preface

This thesis will finalize the special time I had during my study in Delft. The decision to move to Delft and start the MSc Aerospace Engineering with a specialization in Space Exploration, surely is one of the best I have made in my life till now. The Delft University of Technology knew to increase my enthusiasm for space exploration even further, and despite the global pandemic, I have met people which made living in Delft an absolute blast.

Studying the concept of asteroid navigation, forced me to step out of my comfort zone. It definitely increased my engineering skills. Thereby, it is a relevant topic in the present day developments in space exploration. I believe that from now on, I will always make a little jump when asteroid mission developments are in the news.

Before diving into the thesis work, I would like to thank some people that helped me during this moving time. First of all, I want to thank my supervisors Bart and Erwin for their guidance. Although the system has no guidance and control system yet, under their wings, the spacecraft will definitely reach the desired state in the end. I also would like to thank my family and friends for their support, and my housemates for heavily contributing to the enjoyment I experienced living in Delft. Finally, I want to give a special shout-out to my dear friend Niels and my girlfriend Josje. These two were always there for me when things became difficult.

S.J.H. Spee
Delft, Febrary 2022

Contents

Nomenclature

Abbreviations

AIM	Asteroid Impact Mission
AIDA	Asteroid Impact & Deflection Assessment
COF	Center-Of-Figure
COM	Center-Of-Mass
CPU	Central Processing Unit
DART	Double Asteroid Redirection Test
DCM	Direction Cosine Matrix
DNA	Deoxyribonucleic acid
DSN	Deep Space Network
EKF	Extended Kalman Filter
ESA	European Space Agency
GCR	Galactic Cosmic Ray
GG	Gravity Gradient
GNC	Guidance Navigation and Control
GPS	Global Positioning System
IMU	Inertial Measurement Unit
KF	Kalman Filter
LIDAR	Light Detection And Ranging
LKF	Linear Kalman Filter
mascon	Mass concentration
MBA	Main Belt Asteroid
NEAR	Near Earth Asteroid Rendezvous
NEO	Near Earth Object
OSIRIS-REx	Origins, Spectral, Interpretation, Resource Identification, Security, Regolith Explorer
RSI	Radio Science Investigation
SH	Spherical Harmonics
SMASS	Small Main-Belt Asteroid Spectroscopic Survey
SRIF	Square root information weighted least squares filter
SRP	Solar Radiation Pressure
TAG	Touch-And-Go
UKF	Unscented Kalman Filter
UT	Unscented Transformation

Greek symbols

ϵ	Reflectivity coefficient
Γ	Gamma function
μ	Gravitational parameter [m^{3}s^{-2}]
ν	Smoothing parameter
λ	Longitude [rad]
ω_f	Dimensionless per-face factor
ϕ	Latitude [rad]
ρ	Density [kg/m^3]
ρ_b	Bulk Density [g/cm^3]
ρ_g	Grain Density [g/cm^3]
σ	Standard deviation
$\boldsymbol{\chi}$	Sigma vector
$\boldsymbol{\nu}_x$	Gaussian position noise vector
$\boldsymbol{\omega}$	angular velocity vector [rad/s]
$\boldsymbol{\Phi}$	State-transition matrix
$\boldsymbol{\tau}$	Torque

Latin symbols

A	Area [m^2]
$\mathbf{a}$	Acceleration [m/s^2]
$\mathbf{C}$	Direction Cosine Matrix
C_{nm},S_{nm}	Spherical harmonics coefficients
$\bar{C}_{nm}$,$\bar{S}_{nm}$	Normalized spherical harmonics coefficients
e_{ij}	Length between vertices P_i and P_j [m]
$\mathbf{e}_{xk}^-$	*a-priori* estimation error
$\mathbf{e}_{xk}$	*a-posteriori* estimation error
$\mathbf{e}_{zk}^-$	measurement residual
$\mathbf{e}_{S/B}$	Unit vector from spacecraft towards the Sun
$\mathbf{E}_e$,$\mathbf{F}_f$	Dyadic products for edges and faces
$\mathbf{F}$	Force vector [N]
G	Gravitational constant [m^{3}kg^{-1}s^{-2}]
$\mathbf{g}$	Gravitational acceleration [m/s^2]
$\mathbf{G}$	Jacobian matrix of state derivative
$\mathbf{H}$	Measurement matrix
i	Inclination [rad]
I	Moment of inertia tensor
$\mathcal{K}$	Bessel function
$\mathbf{K}$	Kalman gain
l	Scale parameter
L_e	Dimensionless per-edge factor
M	Mass [kg]
m	Order
n	Degree
$\mathbf{n}$	Euler axis of rotation
$\hat{\mathbf{n}}$	Normal vector
$P_\odot$	Solar radiation pressure [N m^{-2}]
P_{nm}	Legendre's function
P_i	Vertex
$\bar{P}_{nm}$	Normalized Legendre's function
$\mathbf{P}$	Covariance matrix
$\mathcal{P}$	Porosity [%]
$\mathbf{q}$	Quaternion
$\mathbf{Q}$	Process noise covariance matrix
r	Distance [m]
R	Radius [m]
$\mathbf{r}$	Position [m]
$\mathbf{R}$	Measurement covariance matrix
U	Gravitational Potential [m^3 kg^{-1} s^{-2}]
$\mathbf{u}$	Control input
$\mathbf{V}$	Jacobian matrix of measurement system with respect to measurement noise
$\mathbf{v}$	Velocity vector [m/s]

W	Weights
$\mathbf{W}$	Jacobian of dynamical system with respect to system noise
$\mathbf{x}$	State
$\hat{\mathbf{x}}^-$	*a-priori* estimate
$\hat{\mathbf{x}}$	*a-posteriori* estimate
$\mathbf{z}$	Measurements

Subscripts

I	Inertial reference frame
A	Asteroid reference frame
B	Body reference frame
S	Sun
g	Gravitational
e	Edge
f	Face

1

Introduction

The thesis work is introduced in this chapter. In section 1.1, arguments are given for studying and heading towards asteroids. After which, section 1.3 gives an overview of the problems that are faced during missions towards asteroids. Subsequently, the research objective and questions are given in section 1.5. Finally, in section 1.6 the structure of the report is highlighted.

1.1. Interest in asteroids

An asteroid is a term generally used for rocky minor planets that orbit the Sun at distances ranging from interior to Earth's orbit to a bit exterior to the orbit of Jupiter (Lissauer and de Pater, 2013). The term asteroid could be confused with comets. Lissauer and de Pater refer to comets, when a coma and/or tail has been detected. Asteroids vary in sizes from a single meter in diameter till the largest asteroid Ceres, which has a radius of about 475 km. Objects smaller than 1 meter in diameter are called meteoroids. When a meteoroid or an asteroid enters Earth's atmosphere it is called a meteor and when it survives the trip it is called a meteorite (Lissauer and de Pater, 2013).

Space organizations such as NASA, ESA and JAXA have shown their common interest in small celestial bodies. Multiple missions towards asteroids or comets have resulted in groundbreaking scientific returns. But what makes these small bodies such as asteroids so interesting? Multiple arguments can explain this common interest in these small bodies, as in particular asteroids.

First, so-called near-Earth asteroids can be of danger by the possibility of collision. In the history of Earth, asteroid impacts had large consequences for life on Earth. Such large impacts can occur again in the future, what argues for monitoring and understanding near-Earth objects (Lissauer and de Pater, 2013). The upcoming Asteroid Impact & Deflection Assesment (AIDA) collaboration between NASA and ESA illustrates the desires of humanity for a planetary defense system (Michel et al., 2018). This mission consists of a first spacecraft, the Double Asteroid Redirection Test (DART) Mission, led by NASA, and a second spacecraft, Hera, led by ESA. The first spacecraft will hit the asteroid called Didymos, after which Hera will analyze the impact by DART on the asteroid its geophysical and dynamical properties (Michel et al., 2018).

Second, asteroid mining is a hot topic. The scarcity of some raw materials on Earth could be decreased by mining it in space (Michel et al., 2015). It could generate a completely new commercial space market, providing data from mining missions of which science could benefit. Also, asteroid mining is mentioned as a technique by which human spaceflight would benefit. Mining resources in space instead of taking it with us from Earth could increase the capabilities of interplanetary travel. For example, the asteroid material could help in protecting astronauts against galactic cosmic ray (GCR) radiation (Brophy et al., 2014).

Besides these arguments, the interest in asteroids is mainly caused by the fact that asteroids are leftovers of the Solar System formation process. This means the asteroids, whose composition has not

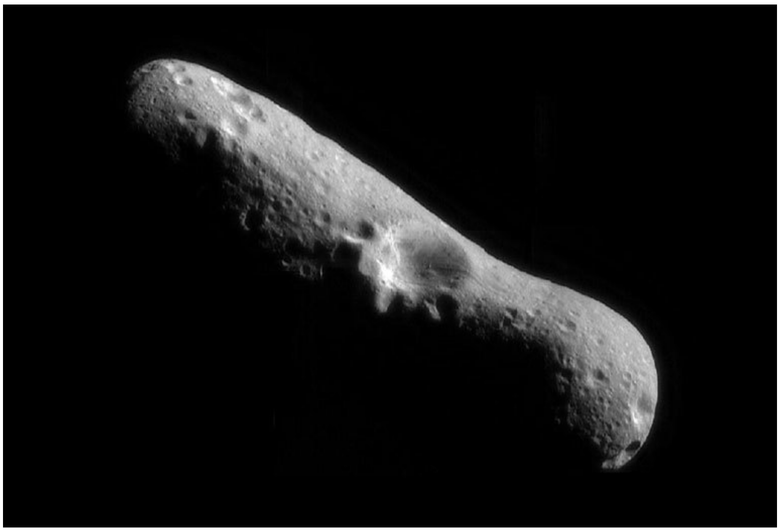

Figure 1.1: A picture of asteroid (433) Eros taken by the NEAR spacecraft. Credit: NASA

altered since the beginning of the Solar System, can give us more information about the solar nebula in which the planet in the Solar System are formed. They can give insights in how life was formed on Earth by searching for building blocks of life in these asteroids (Michel et al., 2015). This curiosity is expressed by the multiple recent asteroid-focused sample and return missions (Siddiqi, 2018).

1.2. Asteroid missions

As stated, there have been multiple missions towards asteroids. Below, some of these missions are highlighted.

1.2.1. NEAR-Shoemaker

The NEAR-Shoemaker mission was launched in 1996. The primary objective was to obtain information on the physical properties, mineral components, morphology, internal mass distribution, and magnetic field of asteroid 433 Eros (Siddiqi, 2018). A picture taken by NEAR is shown in Figure 1.1. On its way to Eros, it also gathered information about asteroid 253 Mathilde during a flyby. The spacecraft became the first human-made object in orbit around a minor planet on 14 February 2000. The initial orbit was an eccentric orbit with a minimum periapsis radius of 321 km and maximum apoapsis radius of 366 km (Williams, 2002). The altitude decreased gradually to be able to do scientific research, which led to improvements of the physical model of the Eros environment.

The spacecraft had lost control with its inertial guidance system for some time. To compensate for this, the rocket propulsion system was fired to correct its orbit. This caused an extensive amount of fuel loss, which was not taken into account in the mission design. Because of the low propellant margin and expiration of an already extended funding, the idea of landing the spacecraft on Eros became a realistic end-of-mission scenario (Antreasian et al., 2002). On 12 February 2001 the NEAR Shoemaker spacecraft became the first spacecraft to land on an asteroid (Siddiqi, 2018). To the suprise of NASA, the spacecraft survived the touch down, what lead to even more scientific results.

1.2.2. Hayabusa

The Hayabusa was a sample return mission by JAXA towards irregular shaped asteroid (25143) Itokawa, launched on 9 May 2003. The mission aimed to be the first to visit a minor planet and return samples from it. The lifetime of the Hayabusa spacecraft resembles the ingenuity of mankind, since the team faced some setbacks during its journey towards the asteroid and back to Earth. With malfunctioning ion thrusters and degraded solar cells, the team managed to let the spacecraft collect 1500 grains of

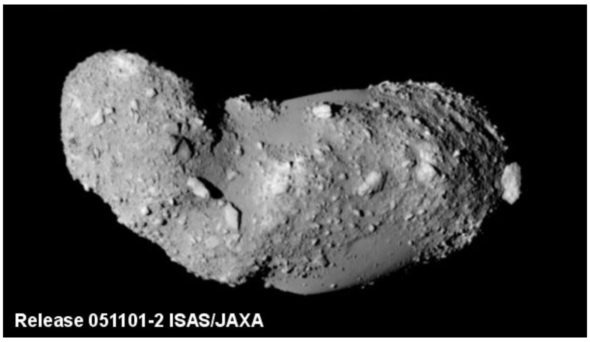

Figure 1.2: Image of asteroid (25143) Itokawa taken by the Hayabusa spacecraft. Credit: JAXA

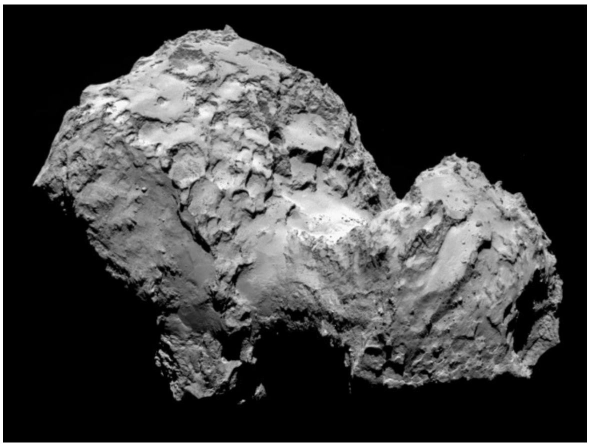

Figure 1.3: Image of comet 67P/Churyumov-Gerasimenko taken by Rosetta's OSIRIS narrow-angle camera on 3 august 2014. Credit: ESA

dust from Itokawa. On 13 June 2010, this became the second sample ever returned to Earth from a different celestial body than the Moon (Siddiqi, 2018). This was three years later than anticipated.

An observation image taken by Hayabusa of Itokawa is shown Figure 1.2. The asteroid is a so-called rubble pile. Such rubble pile is defined as a gravitationally bound collection of smaller bodies and internal void spaces (Lissauer and de Pater, 2013).

1.2.3. Rosetta

On 2 March 2004, the European Space Agency (ESA) launched the Rosetta spacecraft. This spacecraft had a total mass of 3000 kg, containing a 100 kg lander called Philae (Siddiqi, 2018). Although the mission aimed for a comet instead of an asteroid and thus has some different objectives, the mission is interesting since the spacecraft orbited an irregular shaped minor body. The Rosetta mission had multiple objectives, but the prime objective was the in-situ analysis of cometary matter by rendezvous (Hechler, 1997). After the launch was delayed, the team had to cancel the plan to rendezvous with comet 46P/Wirtanen and selected 67P/Churyumov-Gerasimenko as its new destination. An image of this comet is shown in Figure 1.3. During the journey towards this comet, the spacecraft performed a flyby past asteroid 2867 Steins which provided a vast amount of useful scientific data about this asteroid (Siddiqi, 2018).

The Rosetta mission appeared to become one of ESA's most successful planetary missions by retrieving an enormous amount of data about the comet's properties that lead to crucial findings. Rosetta detected water vapor, molecular nitrogen, molecular oxygen, water ice on the surface, the amino acid glycine, and the component of DNA phosphorus for the first time on a comet (Siddiqi, 2018). These discoveries support the theory that comets and asteroids contain the building blocks of life.

1.2.4. DAWN

The mission by NASA called Dawn, can be seen as a very successful mission. This is emphasized by the two times the mission got extended, despite having multiple malfunctions causing the spacecraft entering safe mode, and components becoming unusable during the mission lifetime. The spacecraft launched on 27 September 2007 visited two celestial bodies, what was a first in the history of deep space missions. By reaching the asteroid Vesta in 2011 the spacecraft became the first spacecraft to orbit an object in the main asteroid belt (Siddiqi, 2018). After having orbited the asteroid on multiple altitudes from 2700 to 210 km the spacecraft escaped from Vesta and continued its journey towards dwarf planet Ceres on 5 September 2012. On 7 March 2015 Dawn was maneuvered into an orbit around the largest object known in the main asteroid belt, Ceres (Siddiqi, 2018). Since Ceres is also recognized as a dwarf planet, Dawn became the first spacecraft to study a dwarf planet. Vesta and

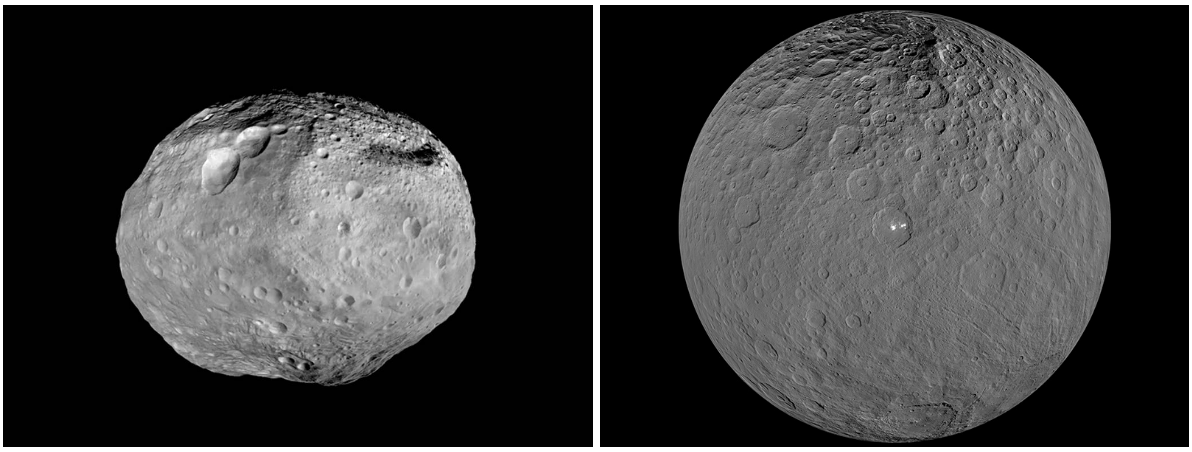

(a) Picture of asteroid Vesta. Credit: NASA (b) Picture of Ceres. Credit: NASA

Figure 1.4: Celestial bodies orbited by Dawn

Ceres are shown in Figures 1.4a and 1.4b, respectively. The spacecraft did orbit Ceres in multiple configurations till November 2018 from altitudes of 1470 till 35 km above the surface (Siddiqi, 2018).

1.2.5. OSIRIS-REx

The sample return mission by primarily NASA and the University of Arizona which launched on 8 September 2016 has the name OSIRIS-REx. This is an abbreviation for Origins, Spectral Interpretation, Resource Identification, Security, Regolith Explorer, what refers to its objectives and capabilities. The main objective of the mission is to collect a sample from the rubble pile asteroid 101955 Bennu and return it to Earth in September 2023 (Siddiqi, 2018). Because of the inclusion of multiple thruster systems that provide redundancy, the spacecraft had the ability to repeat the Touch-And-Go (TAG) procedure multiple times to be sure to collect enough sample. Nevertheless, NASA confirmed in a press-release that on 20 October 2020 the first TAG event already collected more than the minimum amount (59.5 g) of sample [1] and a repetition was thus not required.

1.3. Unpredictable environment

To obtain material from an asteroid, a spacecraft has to reach the surface of the asteroid. This could include a complete landing or a so-called Touch-and-Go maneuver, where the spacecraft only touches the surface for a moment. However, asteroids are small in size and often have a very irregular shape. The relatively small mass of the asteroid and thus small gravitational attraction on the spacecraft, makes the acceleration difficult to predict. Small, unexpected perturbations can therefore have big consequences (Hesar et al., 2016). The spacecraft could escape or collide with the asteroid unintentionally.

As missions generally use radiometric measurements using the Deep Space Network (DSN) to determine their position and velocity, the frequency of updating estimation parameters is limited, because of the signal travel times between the spacecraft and Earth stations. This stirs up the desire for autonomous navigation, which can update its state in higher frequency and correct faster for unexpected perturbations (Gil-Fernandez and Ortega-Hernando, 2018). Also, when going closer to the surface of the asteroid, the connection to the DSN is not assured what emphasizes the need for autonomous navigation even more. Such autonomous navigation system requires to make no use of radiometric tracking from base stations on Earth. The navigation system should depend on other sources, such as the optical navigation (star tracking, landmark tracking) and light detection and ranging (LIDAR) laser altimeters. When closer to the surface, there can be made use of landmark tracking. A landmark is a

---

[1] website: https://www.nasa.gov/press-release/nasa-s-osiris-rex-spacecraft-collects-significant-amount-of-asteroid Date accessed: 10/1/2020

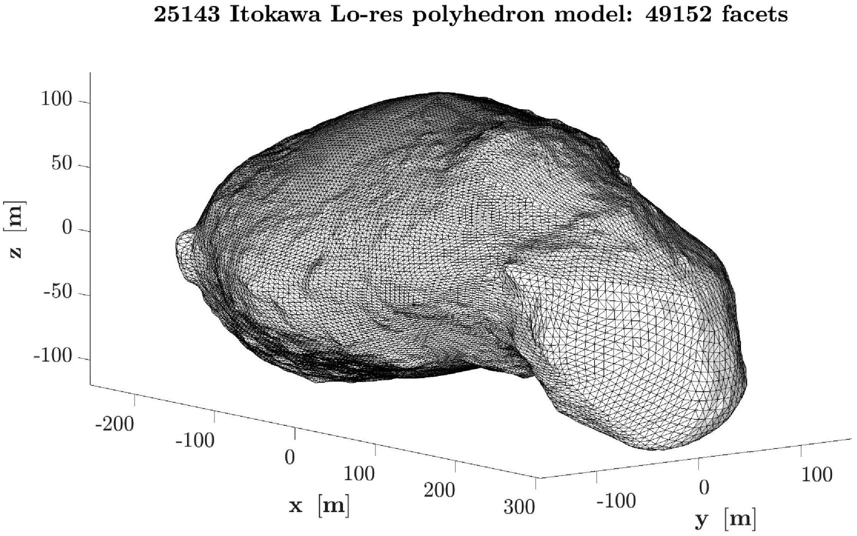

Figure 1.5: Shape model of Itokawa from (Furfaro et al., 2021)

body-fixed vector from the body center towards the surface. It is the center of a small digital terrain, which is a map over a fraction of the surface (Mastrodemos et al., 2011). The contrast in brightness is used to distinguish landmarks. Gaskell et al. (2008) developed a method and software suite used for multiple missions to identify and progress landmark positions (Gaskell et al., 2008; Mastrodemos et al., 2011; Williams et al., 2018). The study describes how a landmark position on the surface can be processed using the positions on images and the spacecraft positions. It explains that when landmark positions are known with respect to the body after a survey phase, the landmark maps will be correlated with new images used to determine the relative spacecraft state in close proximity.

During the Hayabusa mission, the navigation system switched to autonomous mode for the landing phase. The spacecraft was equipped with a crucial laser range finder, which had four beams that have provided both altitude information as attitude with respect to the surface. During the descent the orbit of the spacecraft was synchronized with the rotation of the asteroid such that the observed surface was fixed below the spacecraft. The navigation of the horizontal motion relative to the surface was performed by setting an artificial target marker on the surface what gets tracked. In this way the spacecraft could determine how to correct for the horizontal motion (Kubota et al., 2006). This method can be suitable for landing using an asteroid-rotation fixed orbit. However, if it is desired to orbit the asteroid at a relatively low altitude, it is convenient for the navigation system to have knowledge about the asteroid environment. The more accurate the dynamical model of the asteroid, the more accurate the predicted accelerations on the spacecraft.

The general method used for modeling the gravity field of a celestial body is spherical harmonics. Unfortunately, this method diverges inside the object circumscribing sphere, called the Brillouin sphere (Hesar et al., 2016; Takahashi et al., 2013). As asteroid shapes are often very different from spherical, using the spherical harmonics model for navigation, would make the navigation system unusable in regions around the asteroid inside this Brillouin sphere. This property of the spherical harmonics method creates the demand for different approaches to predict or correct for the influences of the gravity field.

One alternative for modeling the gravity field is the polyhedron gravity model. This model requires an available shape model. Such shape model consists of vertices and faces describing the spatial form of the asteroid. An example is given in Figure 1.5, showing the shape model of asteroid Itokawa. By assuming a constant density in this volume, the gravitational attraction caused by the virtual body can be calculated (Werner and Scheeres, 1997). However, relative to other models, this polyhedron model is computationally expensive.

Another alternative for the spherical harmonics is using point-masses. The gravity model used by the Hayabusa mission gives an example of such point-mass model. This gravity field model consists

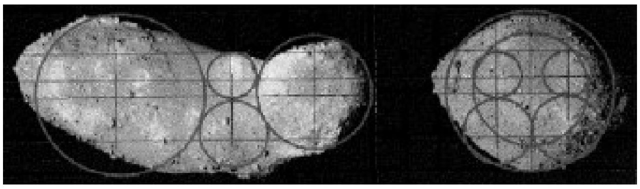

Figure 1.6: Gravity model for the hayabusa mission using six point masses (Yoshimitsu et al., 2009).

of 6 points masses, divided over the shape of Itokawa. The point mass positions are illustrated in Figure 1.6 (Yoshimitsu et al., 2009). This gravity field model was made of optical images describing the shape and estimations for the gravitational parameters before approaching Itokawa.

Besides the shape of the asteroid, another property which influences its gravity field is the possible heterogeneous interior density distribution (Scheeres et al., 2020). Density differences or void spaces inside the asteroid cause a different gravity field than would be expected if mass of the asteroid would be homogeneously distributed through its body. As fluctuations in the experienced acceleration by the spacecraft is related to the mass distribution of the target body, determining the gravity field could give information about the density differences and thus the interior structure of the asteroid (Park et al., 2010; Scheeres et al., 2020). This could give insights in the asteroid its past or eventually help with selecting a landing site.

As a result from earlier missions, constraints have been made about interiors of targeted asteroids. Asteroids could appear to have a quite uniform mass distribution. An example of such asteroid is Eros. The polyhedron model of Eros appeared to be quite consistent with the measured gravity field and the constant-density assumption would thus give a good approximation (Yeomans et al., 2000). Also, according to Miller et al. (2002), the center of figure and center of mass of the asteroid only deviated 30 meters. Relative to the maximum intersection of Eros of about 32 kilometers, this deviation is small, what also indicates small heterogeneity.

On the contrary, asteroids Itokawa and Bennu appeared to have a non-uniform mass distribution. By comparing the measured gravity field with the modeled gravity field from theoretically possible density distributions of Bennu, Scheeres et al. (2020) found that a distribution as shown in Figure 1.7 would explain the measured gravity field best. The computed model contains lower densities at Bennu's equatorial bulge and center, and higher densities in the middle layer. These mass regions are indicated in the figure.

Itokawa is expected to have a non-uniform density distribution through its body. This expectation was raised by the relatively large difference between the center of mass and center of figure. According to Kanamaru et al. (2019), this offset can be explained by a ”compressed head” model. This model splits the body of Itokawa in two density regions, as shown in Figure 1.8. The head is expected to have an average density of 2,450 kg/m^3, while the body is expected to have a density of about 1,930 kg/m^3.

1.4. Thesis heritage

This study can be considered as an extension on the work done by Razgus (2016) and Bourgeaux (2020). Both studies focussed on missions around minor bodies and developed a Kalman filter.

Razgus (2016) investigated how to make relative navigation techniques more robust, reliable and autonomous in asteroid missions. To answer this question, he tested the dual-quaternion approach to represent the spacecraft's pose. In the study, the dual-quaternion approach is compared with the conventional one (Cartesian coordinates for position and quaternions for attitude) using an extended Kalman filter. Both methods appeared to have identical performances. Possible reasons for this similarity in performance are given. It could be caused by a high dependency on measurements, as the models have similar measurement equations. The high process noise, which causes the model to rely more on the measurements, means that the gravity field of the asteroid is inaccurate. This appeared to be the case, as for example for asteroid Kleopatra, where the difference between the central gravity field and the polyhedron gravity field can be about 80% at an altitude of 100 km. For a transient

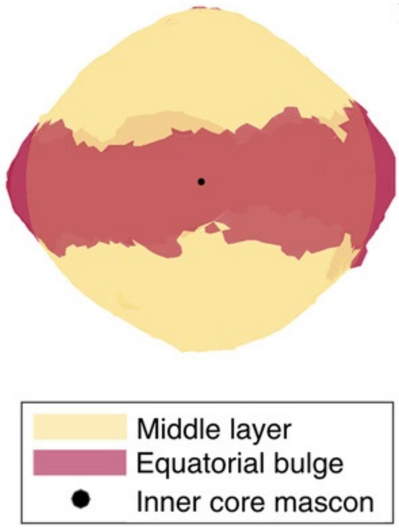

Figure 1.7: Three-component density model for asteroid 101955 Bennu as hypothesized by Scheeres et al. (2020).

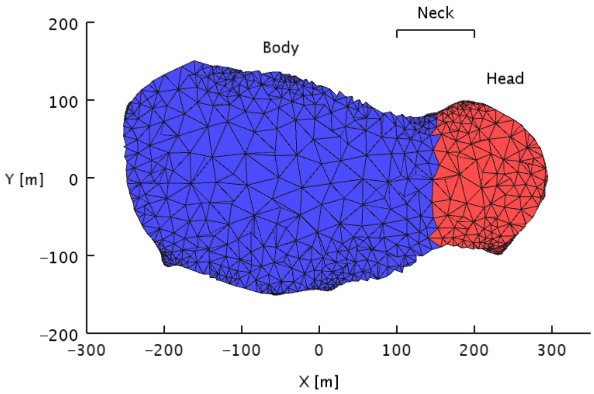

Figure 1.8: Compressed Head Model for Itokawa, where the head and body density regions are indicated with the red and blue color, respectively (Kanamaru and Sasaki, 2019).

mission phase, the dual-quaternion method appeared to be moderately more accurate. The dual-quaternion extended Kalman filter, the convergence time appeared to be about 500 seconds lower, tested by Monte-Carlo simulations. However, the computational time appeared to be 40-50% higher than the conventional quaternion-vector filter. Also, it was found that improving the 'on-board' gravity field, made convergence possible even in an unfavourable scenario and increased estimation accuracy. Besides designing the filter, Razgus (2016) invented an approach for simulating the navigation camera. By this simulation, the number of visible landmarks can be simulated.

In the recommendations of Razgus (2016), it is mentioned that the filters should be tested using a more precise gravity model. The suggestion is raised to estimate this corresponding gravity field real-time. This was exactly what Bourgeaux (2020) has done. She implemented the spherical harmonics model into a filter to estimate the gravity field together with the spacecraft state.

Bourgeaux (2020) investigated how to increase the safety of autonomous navigation for asteroid missions. For her research, a spacecraft was simulated in the environment of asteroid 433 Eros. It was concluded multiple points based on her findings. Measuring the forces and torques acting on the spacecraft in an asteroid environment as accurately as possible will improve the safety of the autonomous navigation. The measurements should provide as much environmental information as possible. Also, the research showed that solar radiation pressure (SRP) and third-body perturbations cannot be neglected, as they cause significant errors in the estimation of the gravitational parameter. This requires the navigation software to be able to predict these forces and apply these to the dynamical model. Last, it was concluded that the gravity field of the asteroid shall be included in the estimation. It is added that the spherical harmonics model is a suitable model, but only before the landing phase. In this phase, the spacecraft reaches altitudes below the sphere of reference (Brillouin sphere), in which the spherical harmonics model diverges. The polyhedron gravity field is mentioned as an alternative, but has the disadvantage of being computationally heavy. Modeling the gravity field by a single point mass appeared to give errors up to 30% at low altitude orbits, what emphasizes the importance of the gravity model. Bourgeaux (2020) developed a unscented Kalman filter, which used only on-board data and measurements. The unscented Kalman filter appeared to be much easier to implement as the extended Kalman filter. The difference in performance did not show to be significant. Besides the state, this filter estimated the asteroid Eros' spherical harmonic gravity field up to degree and order 8 below 10% error. The state of the spacecraft was estimated with errors below 10 meters for position and 0.01 m/s for velocity. The model was capable of estimating higher order gravity field coefficients. However, it was decided to limit the estimation to degree and order 8, because of the relatively small increase in accuracy with respect to the increased computational costs.

In addition to these conclusions, Bourgeaux (2020) gives some recommendations to improve the model. The recommendations highlight the dependency of the model on the shape of the asteroid. For example, as Eros has an irregular shape, the J_2 effect could be estimated accurately in an early mission phase. Because of this early accuracy in the J_2 parameter, this parameter is not estimated during later mission phases to increase computational efficiency. Some asteroids are less irregular, what could require this parameter to be estimated for a longer duration. By testing the software in other environments with other settings, its efficiency can be evaluated. Also, as the model used some constant values, such as the solar radiation pressure and rotational rate, the system should be tested including these parameters in the estimation, without assuming these values as given. The most relevant recommendation for this thesis work, was to investigate alternative gravity field estimation techniques for the last phase of the mission. This recommendation arises from the spherical harmonics model its disadvantage of divergence inside the Brillouin sphere, and emphasizes the need for different gravity modeling techniques.

1.4.1. Gravity field estimation

As the need for a different gravity model close to asteroids is emphasized in earlier work, the focus of this thesis is on investigating another gravity field model. As the polyhedron model is computationally expensive, it was shown in Chanut et al. (2015) that a point-mass distribution is a faster alternative. Using this model, the asteroid is filled with a number of point masses, so called mascons (mass-concentrations), all influencing the gravitational attraction on a spacecraft. In Park et al. (2010) it was shown that such model can be implemented in an estimation filter and is a promising model for navigation using measurements inside the Brillouin sphere of asteroids.

1.5. Research Questions

From the previous sections in this chapter, the relevancy of asteroid missions and the challenges regarding navigation are highlighted. As this thesis will build upon the studies highlighted in these sections, the focus is set on improving gravity field estimation for navigation. Since the spherical harmonics model has proven to be suitable till reaching the Brillouin sphere, the focus is on using a gravity model which eliminates this limitation. This thesis title ”Asteroid gravity field estimation below Brillouin sphere” is based on this choice. Therefore, the following research objective is defined:

> *Increase the safety of navigation near asteroids by improving the gravity field estimation inside the Brillouin sphere.*

As the mascon model converges inside the Brillouin sphere and showed promising results when implemented in a state estimation filter, this model will be examined to reach the objective. To achieve the objective using this model, the following research question has to be answered:

> *Can the implementation of the mascon gravity field model for estimation make autonomous navigation more robust inside the Brillouin sphere of a heterogeneous asteroid?*

To answer this research question, the following sub questions will be answered:

a) What is the best approach to implement the mascon gravity field model during a multi-phase mission.

b) What is the effect of gravity field estimation on the accuracy and convergence speed of the estimation?

c) How does density heterogeneity influence the estimation performance?

To give the research some guidance, the following requirements and assumptions are given below.

Requirements

REQ-01 The spacecraft shall travel through the asteroid's circumscribing sphere.

REQ-02 The spacecraft's trajectory shall not go through the asteroid body.

REQ-03 The shape of Eros shall be used.

REQ-04 The polyhedron gravity model shall be used to model the real-world asteroid gravity field.

REQ-05 The simulator shall be able to model density differences inside the asteroid shape.

REQ-06 Multiple degrees of density heterogeneity shall be tested.

REQ-07 Density differences shall be modeled up to minimal precision of 1 km^3.

REQ-08 The mascon model shall be implemented in navigation system and its gravitational parameters shall be estimated.

REQ-09 The navigation system shall estimate the spacecraft's position, velocity.

REQ-10 The position of the spacecraft in the close proximity phase shall be estimated with a 1σ accuracy of 1 meter and the velocity shall be determined with an accuracy of 1 mm/s.

REQ-11 The navigation system shall use the extended Kalman filter.

REQ-12 The navigation system shall be tested with multiple mascon models for a certain number of point masses.

REQ-13 The navigation system shall determine the spacecraft's relative position and velocity.

Assumptions:

- The orbit of the asteroid around the Sun is not taken into account.
- The SRP is estimated in an early stage of the mission. The perturbing force is thus assumed known and not estimated.
- The sensors shall have no misalignment or scaling errors.
- The shape model is determined before reaching the close proximity phases.
- There is no guidance or control system that influences the spacecraft's trajectory or attitude.
- The asteroid rotates at a constant rate around its z-axis.

1.6. Outline

To finally answer these research questions, a spacecraft is simulated in an asteroid environment. The concept of asteroids and the dynamics of such asteroid environment are explained in chapter 2. The asteroid of interest is 433 Eros as this asteroid has an elongated shape and is also used in Bourgeaux (2020). Besides this real-world simulator, a state estimator is designed in the form of an extended Kalman filter (EKF), which uses measurements as input based on the simulated trajectories. The mascon gravity field is implemented in this EKF. The design of the software will be addressed in chapter 4. The steps taken during and the results from analysis are given in chapter 5. Finally, the research questions will be answered and recommendations on future work will be given in chapter 6.

2

Asteroid environment

In this section, the dynamics and kinematics of an asteroid environment are addressed. First, the concept of asteroids and their relevant properties are highlighted in section 2.1. Next, the reference frames used in the software are explained in section 2.2. In section 2.3 the forces influencing the translational motion of a spacecraft in an asteroid environment are explained, followed by the rotational motion in section 2.4.

2.1. Asteroids

In this section, relevant asteroid properties concerning asteroid heterogeneity are introduced. Also, the properties of target body, asteroid 433 Eros, are highlighted.

2.1.1. Location

Asteroids are classified based on multiple aspects. The first criterion is the location of the asteroid in the Solar System. The three main groups of asteroids in the Solar System are:

- **Main Belt Asteroids (MBAs):** As the name states these asteroids are located in the main asteroid belt at distances between 2.1 and 3.3 au from the Sun. The asteroid orbits have a mean eccentricity of about 0.14 and a mean inclination of 15° with the ecliptic plane. At certain resonance areas with Jupiter there are so-called Kirkwood gaps, where no or almost no asteroids are located (Lissauer and de Pater, 2013).
- **Near Earth Objects (NEOs):** All asteroids and comets that have perihelia smaller 1.3 au are called NEOs. Because of their orbits that come relatively close to Earth's orbit it could mean that there is a chance of collision with our planet. This could possibly mean danger for the habitants of planet Earth (Lissauer and de Pater, 2013).
- **Trojan Asteroids:** Thousands of asteroids have been discovered near the stable Sun-Jupiter L_4 and L_5 points. These objects are called Trojan asteroids (Lissauer and de Pater, 2013).

2.1.2. Composition

Asteroids are classified based on their composition. The most influential technique in obtaining information about the composition is spectroscopy. Based on reflectance spectra and albedo information, an asteroid is classified by a taxonomic class. The main taxonomic classes are given in Table 2.1. Most asteroids belong to the C-type, also the carbonaceous type. About 40% of all discovered asteroids belongs to this group of dark bodies. Most C-type asteroids are found near the outer regions of the main belt. According to NASA[1], these asteroids are examples of the most ancient objects in the

---

[1] https://solarsystem.nasa.gov/asteroids-comets-and-meteors/asteroids/in-depth/ Date accessed: 04/12/2020

Table 2.1: Asteroid Taxonomic Types (Adapted from Lissauer and de Pater 2013)

Type	Characteristics
C	Carbonaceous asteroids; similar in surface composition to CI and CM meteorites. Dominant in outer belt (>2.7 AU)
D	Extreme outer belt and Trojans. Red featureless spectrum, possibly due to organic material.
P	Outer and extreme outer belt. Spectrum is flat to slightly reddish, similar to M types, but lower albedo.
S	Stony asteroids. Major class in inner-central belt.
M	Stony-iron or iron asteroids; featureless flat to reddish spectrum.
W	Visible light spectra similar to those of M types but have an absorption band near 3 μm (indicative of hydration).
V	Similar to basaltic achondrites. Type example: 4 Vesta

Table 2.2: Table from Consolmagno et al. (2008), containing the carbonaceous chondrite average densities and porosities.

Class	**Avg. grain density (g/cm^3)**	**±**	**Avg. bulk density (g/cm^3)**	**±**	**Avg. porosity (%)**	**± (%)**
CI	2.46	0.04	1.6	0.03	35	–
CM	2.90	0.08	2.25	0.08	23.1	4.7
CO	3.41	0.23	3.03	0.19	10.8	9.1
CVo	3.30	0.15	2.79	0.06	21.8	1.7
CVr	3.45	0.09	0.12	0.25	9.7	4.9
CK	3.58	0.09	2.85	0.08	21.8	2.2

Solar System and probably consist of clay and silicate rocks. With 30 to 35% of the asteroids, the class with stony S-type asteroids is the second largest group. These bright reddish asteroids are especially present with large numbers in the inner parts of the main belt and contain silicate materials and nickel-iron. The metallic nickel-iron M-type asteroids are mostly seen in the central region of the main asteroid belt. D- and P-type asteroids only are identified in the extreme outer parts of the main asteroid belt and as Trojan asteroids (Lissauer and de Pater, 2013). These two types are expected to contain organic rich silicates, carbon and anhydrous silicates with possibly water ice (Nelson et al., 1993). The W-type asteroid were classified as M-type earlier, but distinguish themselves because of the indication of water in the spectrum. The V-type asteroids are expected to contain olivine and pyroxene. By comparison with meteorites it is concluded that the surface of V-type asteroids is covered with basaltic material (Lissauer and de Pater, 2013; Nelson et al., 1993).

In a study by Bus (2002), the SMASSII classification was introduced. This classification is of higher precision and (sub)divides the earlier mentioned taxonomic classes, based on the spectral characteristics. The carbonaceous asteroids (C-class) for example, can be distinguished in the classes as shown in Table 2.2.

Besides spectroscopic measurements, there are also remnants of asteroids or meteoroid on Earth. These meteorites survived the passage through Earth's atmosphere as a meteor. The properties of these meteorites can be linked with asteroid types, as is done in Table 2.2. Besides the densities of these samples, also the porosity is an important property. The porosity is a measure of voids an cracks inside a volume. These flaws in the physical arrangement of mass create a discrepancy between the bulk density ρ_b and the grain density ρ_g, where the bulk density is the overall density of the complete volume, and the grain density is the density of the material. The porosity describes the relation between these two densities as follows (Consolmagno et al., 2008):

$$\mathcal{P} = \left(1 - \frac{\rho_b}{\rho_g}\right) \times 100\% \tag{2.1}$$

When studying a certain asteroid, its reflectance spectrum can be used to indicate a meteorite with

Table 2.3: Table adapted from Consolmagno et al. (2008), containing the density and macro-porosity of Eros, Itokawa, Vesta, and the averaged values per asteroid-type S, C and M.

Object	Density (g/cm3)	±	Mass (kg)	Class	Meteorite analog	Macro-porosity (%)	± (%)
Average S	2.69	0.04		S	L Chondrite	19.9	1.2
Average C	1.40	0.05		C	CM	37.7	2.2
Average M	4.7	0.5		M	Iron	40	13
433 Eros	2.67	0.03	6.68×10^{15}	S	L Chondrite	20.5	0.9
25143 Itokawa	1.95	0.14	3.58×10^{10}	S	L Chondrite	42.0	4.2
4 Vesta	3.44	0.12	2.74×10^{20}	V	L Chondrite	0.0	3.6

a similar spectrum, which can be used as analog. This meteorite can than be used to make estimations about the asteroid's interior properties. If the mass and volume of an asteroid are estimated, its bulk density can be determined and compared with the grain density of the analog meteorite. In this way, the bulk porosity of an asteroid can be obtained using Eq. (2.1). This bulk porosity is a combination of the micro-porosity, which can be assumed equal to the porosity of the meteorite, and the macro-porosity, which is caused by large-scale cracks and voids in the asteroid. Consolmagno et al. (2008) summarized multiple studies to these meteorite and asteroid properties. In Table 2.3, a part of the result of this study is shown. The average density and macro-porosity of common asteroid-types are given in this table, together with the properties of three extensively studied asteroids. The table also indicates the meteorite analog used to determine its properties, where the L chondrite refers to the stony L-type of the SMASS taxonomy, which is a subdivision of the S-type. The values in these Tables 2.2 and 2.3 helped in designing asteroid density distributions.

In the history of the Solar System, collisions of bodies have played an important role. The collisions of bodies can have consequences for their shape, mass and orbit. When an impact is not that energetic and bodies are not dispersed, only shattered or fractured, fragments can form a single body again. Such single body is then called a rubble pile, which was already introduced in section 1.2. When two bodies form a system rotating around their barycenter, this is called a binary system. If these bodies are gravitated towards each other till they form one body, this is called a contact-binary asteroid (Margot et al., 2015). Such contact-binary can have a clear density difference between the two lobes forming one asteroid.

2.1.3. Eros

For the thesis work, Eros has been used as the target asteroid. This S-type asteroid is, as mentioned earlier, visited by the NEAR-spacecraft. Because of this mission, a detailed shape model is available of the asteroid and mass and density are determined accurately. In Table 2.3, Eros' bulk density, porosity and mass are given according to Yeomans et al. (2000). Eros has a size of 34.4×11.2×11.2 and orbits the Sun with a mean semi-major axis of 1.458 au [2]. The rotation period of Eros is equal to 5.27 Earth hours and the surface normal gravitational accelerations range from 2.1 to 5.5 mm/s^2 (Yeomans et al., 2000).

Since Eros has an elongated shape, it has a relatively large reachable space around its body that is inside the Brillouin sphere. This makes the asteroid suitable for traveling through the Brillouin sphere. Also, Bourgeaux (2020) studied the implementation of the spherical harmonics model with Eros as target asteroid. The use of the same asteroid is useful for comparison between the two models.

---

[2] JPL Small-Body Database Lookup:https://ssd.jpl.nasa.gov/tools/sbdb_lookup.html#/?sstr=2000433; Accessed on 21/10/2021

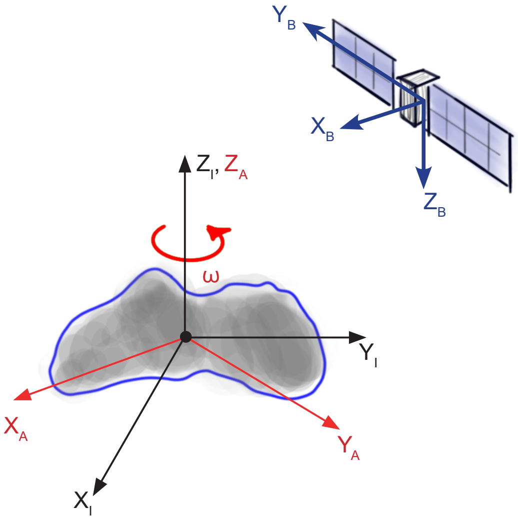

Figure 2.1: Schematic visualization of the used reference frames.

2.2. Reference frames

When describing the dynamics during the mission, it is important to know in what reference frame these dynamics are described. During this thesis, three reference frames are used. These three reference frames are explained below and schematically visualized in Figure 2.1

- **Inertial reference frame:**
  This reference frame has its origin fixed in the center of the asteroid and its axes are inertially fixed. Vectors or matrices in the inertial reference framed are indicated by the subscript I.

- **Asteroid-fixed reference frame:**
  The origin of the asteroid-fixed reference frame is placed in the center of the asteroid, similar to the inertial reference frame. In contrary to the inertial frame, the axes of this reference frame rotate synchronous to the asteroid rotation around. The x-axis of this reference frame is fixed to the asteroid its prime meridian. For a rotation around the z-axis, the z-axis of the asteroid frame remains equal to the z-axis of the intertial reference frame. The frame is indicated by the subscript A.

- **Body-fixed reference frame:**
  The origin of the body-fixed reference frame is fixed in the center of the spacecraft. The axes of the frame, x, y, and z, are defined along the length, width and height of the spacecraft, respectively. These axes are kept fixed with respect to the spacecraft body. The frame is indicated by subscript B.

2.2.1. Conversion between reference frames

To translate vectors from one reference frame to another, a *Direction Cosine Matrix (DCM)* can be used. Considering the vector $\mathbf{r} = (r_1\ r_2\ r_3)_A^T$ in the asteroid reference frame, vector $\mathbf{r}$ can be converted to the body reference frame using the DCM $\mathbf{C}_{B/A}$ as follows:

$$\mathbf{r}_B = \mathbf{C}_{B/A}\mathbf{r}_A, \tag{2.2}$$

A DCM is an orthonormal matrix with the following properties:

$$\mathbf{C}_{B/A}^T = \mathbf{C}_{A/B} = \mathbf{C}_{B/A}^{-1} \tag{2.3}$$

$$\mathbf{C}_{A/B}\mathbf{C}_{A/B}^T = \mathbf{C}_{A/B}^T\mathbf{C}_{A/B} = \mathbf{I} \tag{2.4}$$

Consider two sets of orthogonal unit vectors $(\mathbf{a}_1, \mathbf{a}_2, \mathbf{a}_3)^T$ and $(\mathbf{b}_1, \mathbf{b}_2, \mathbf{b}_3)^T$ in the asteroid- and body-fixed reference frame, respectively. Using the angles between the unit vectors, the unit vectors of $\mathbf{b}$ can be described in terms of unit vectors of $\mathbf{i}$ as follows (Wie, 2008):

$$\begin{pmatrix} \mathbf{b}_1 \\ \mathbf{b}_2 \\ \mathbf{b}_3 \end{pmatrix} = \begin{bmatrix} \cos\theta_{11} & \cos\theta_{12} & \cos\theta_{13} \\ \cos\theta_{21} & \cos\theta_{22} & \cos\theta_{23} \\ \cos\theta_{31} & \cos\theta_{32} & \cos\theta_{33} \end{bmatrix} \begin{pmatrix} \mathbf{a}_1 \\ \mathbf{a}_2 \\ \mathbf{a}_3 \end{pmatrix} = \mathbf{C}_{B/A} \begin{pmatrix} \mathbf{a}_1 \\ \mathbf{a}_2 \\ \mathbf{a}_3 \end{pmatrix} \tag{2.5}$$

Alternative methods to obtain the DCM of two frames, which can be more efficient and/or robust are available. One example is using *Euler angles*. This method can simplify the maximum number of parameters for describing the rotation from nine to three parameters. The method splits the rotation in three separate rotations around each of the three axes. Each rotation about one of the axes requires one rotation matrix $C_i(\theta_i)$ with only one angle θ_i. The DCM can then be computed according to the following relation (Wie, 2008):

$$\mathbf{C}_{B/A} = \mathbf{C}_1(\theta_1)\mathbf{C}_2(\theta_2)\mathbf{C}_3(\theta_3) \tag{2.6}$$

One should mind the sequence of rotations is of importance using Euler angles.

The attitude of a body is often represented by *quaternions*. These four-dimensional hyper-complex numbers can also be used to compute the DCM for conversion between reference frames. A quaternion $\mathbf{q}$ is defined as:

$$\mathbf{q} = q_1 i + q_2 j + q_3 k + q_4, \tag{2.7}$$

where it yields that $||\mathbf{q}|| = 1$ and the symbols i, j, k indicate imaginary numbers with the following properties:

$$\begin{aligned} ij &= -ji = k \\ jk &= -kj = i \\ ki &= -ik = j \\ i^2 = j^2 &= k^2 = ijk = -1 \end{aligned} \tag{2.8}$$

For attitude operations, the quaternion is considered a four-component vector, where the first three components represent the vectorial part $\mathbf{q}_{1:3} = (q_1, q_2, q_3)^T$ and the fourth component the scalar part q_4:

$$\mathbf{q} = \begin{pmatrix} \mathbf{q}_{1:3} \\ q_4 \end{pmatrix} \tag{2.9}$$

The quaternion does not rotate a certain angle around each unit axis, but only one angle ϕ along a single so-called Euler axis of rotation $\mathbf{n}$. Considering such rotation, the quaternion is defined as:

$$\mathbf{q}(\mathbf{n}, \phi) = \begin{pmatrix} \mathbf{n} \sin\phi/2 \\ \cos\phi/2 \end{pmatrix} \tag{2.10}$$

Using quaternions, the DCM can be computed as follows:

$$\mathbf{C}(\mathbf{q}) = \left(q_4^2 - \|\mathbf{q}_{1:3}\|^2\right)\mathbf{I}_3 - 2q_4\left[\mathbf{q}_{1:3}\times\right] + 2\mathbf{q}_{1:3}\mathbf{q}_{1:3}^T \tag{2.11}$$

with

$$\left[\mathbf{q}_{1:3}\times\right] = \begin{bmatrix} 0 & -q_3 & q_2 \\ q_3 & 0 & -q_1 \\ -q_2 & q_1 & 0 \end{bmatrix} \tag{2.12}$$

Substituting Eq. (2.12) into Eq. (2.11) gives:

$$\mathbf{C}(\mathbf{q}) = \begin{bmatrix} q_1^2 - q_2^2 - q_3^2 + q_4^2 & 2\left(q_1q_2 + q_3q_4\right) & 2\left(q_1q_3 - q_2q_4\right) \\ 2\left(q_1q_2 - q_3q_4\right) & -q_1^2 + q_2^2 - q_3^2 + q_4^2 & 2\left(q_2q_3 + q_1q_4\right) \\ 2\left(q_1q_3 + q_2q_4\right) & 2\left(q_2q_3 - q_1q_4\right) & -q_1^2 - q_2^2 + q_3^2 + q_4^2 \end{bmatrix} \tag{2.13}$$

If the attitude, of for example the spacecraft, $\mathbf{q}_{B/I}$ is known through measurements during a mission with respect to the inertial reference frame, DCM $C_{B/I}$ can be computed and transformations between the body and inertial reference frame can be executed.

2.3. Translational Motion

The translational motion of a spacecraft orbiting an asteroid is dependent on the forces acting on the spacecraft. According to Newton's law, the relation between the acceleration of the spacecraft and the resultant of all forces acting on the spacecraft $\mathbf{F}$ is described in the following equation:

$$\ddot{\mathbf{r}}_I = \mathbf{F}/M \tag{2.14}$$

Here, $\mathbf{r}_I$ indicates the position of the spacecraft body with respect to the inertial frame. The accelerations on the spacecraft due to the different forces can be split in the acceleration due to the gravitational attraction $\mathbf{g}$ of the orbited asteroid and other perturbing forces $\mathbf{a}_{pert}$. Doing this, the translational motion of the spacecraft can be described by the following equation of motion:

$$\ddot{\mathbf{r}}_I = \mathbf{g}_I + \mathbf{a}_{pert,I} \tag{2.15}$$

The translational kinematics of the spacecraft are described by:

$$\dot{\mathbf{r}}_I = \mathbf{v}_I \tag{2.16}$$

where, the velocity of the spacecraft is indicated with the symbol $\mathbf{v}$. As Newtons equation, Eq. (2.14), only yields in the inertial reference frame, the equations of motion are defined with respect to this frame. If accelerations and velocities would be described in the body- or asteroid-fixed reference frame, it would require to include apparent forces. As for simulations of the real-world motion all accelerations are defined in the inertial reference frame, Eqs. (2.15) and (2.16) can be used as stated.

2.3.1. Gravitational acceleration

The main contributor to the acceleration of the spacecraft is the gravitational acceleration due to the asteroid's attraction. A way commonly used to model the gravitational influence of a body at a great distance is assuming it as a point mass. When the distance between the spacecraft and the body is much greater than the diameter of the body, the body may be assumed as point with the total mass of the body. Using Newton's gravitational law, the gravitational force $\mathbf{F_{12}}$ acting on the body with mass M_2 can be described as:

$$\mathbf{F_{12}} = -G\frac{M_1 M_2}{||\mathbf{r}_{12}||^3}\mathbf{r}_{12} \tag{2.17}$$

where $\mathbf{r}_{12}$ indicates the vector pointing from body 1 towards body 2, G the gravitational constant and M_1 the mass of the spacecraft. When coming closer to a body, the influence of the size and shape of the body cannot be neglected. Below, alternative, more precise, methods to model the gravity field are evaluated.

Spherical Harmonics

The spherical harmonic (SH) gravity field, also called the exterior gravity field is an efficient approach to model a celestial body's gravity field. This gravity is modeled using harmonic functions by the gravitational potential U, which is dependent on the position of the spacecraft with respect to the body. The gravity field is expressed by the following equation (Takahashi et al., 2013):

$$U(r,\phi,\lambda) = \frac{GM}{r}\left[1 + \sum_{n=1}^{\infty}\left(\frac{R}{r}\right)^n \sum_{m=0}^{n} P_{nm}(\sin\phi) \times [C_{nm}\cos(m\lambda) + S_{nm}\sin(m\lambda)]\right] \tag{2.18}$$

In this equation r is the distance between the spacecraft the center of the spherical body with reference radius R, ϕ and λ the latitude and longitude of the spacecraft, respectively, G the gravitational constant, P_{nm} the Legendre function of degree n and order m, and C_{nm} and S_{nm} are the spherical harmonic coefficients. The Legendre function P_{nm} is defined as:

$$P_{nm}(t) = \frac{1}{2^n n!}(1-t^2)^{m/2}\frac{d^{n+m}}{dt^{n+m}}\left(t^2-1\right)^n \tag{2.19}$$

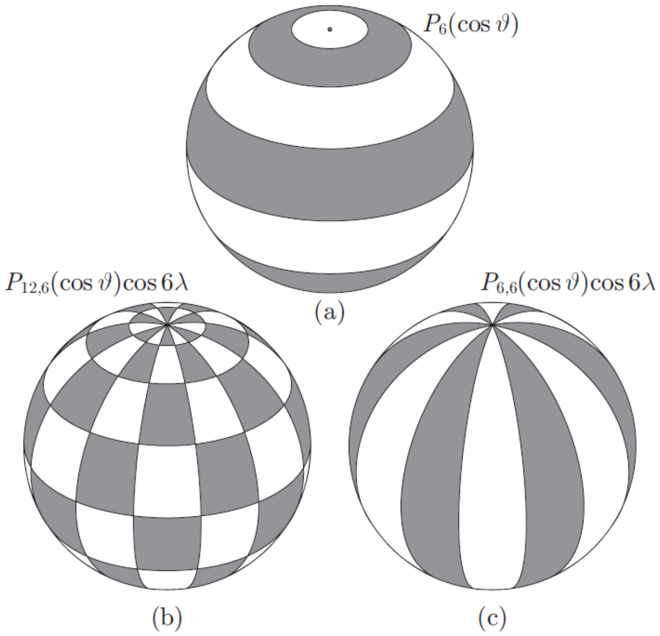

Figure 2.2: Examples of the three different kinds of spherical harmonics: (a) zonal harmonics, (b) tesseral harmonics, and (c) sectorial harmonics; with colatitude $\vartheta = \pi - \theta$ (Hofmann-Wellenhof and Moritz, 2006)

Eq. (2.18) can be rewritten using the normalized coefficients $\bar{C}_{nm}$ and $\bar{S}_{nm}$. Using these normalized coefficients requires the Legendre polynomials also to be normalized using $\bar{P}_{nm}$. The normalization uses the following relations:

$$\begin{aligned} C_{nm} &= \Pi_n^m \bar{C}_{nm} \\ S_{nm} &= \Pi_n^m \bar{S}_{nm} \\ P_{nm} &= \frac{\bar{P}_{nm}}{\Pi_n^m} \\ \Pi_n^m &= \sqrt{\frac{(n-m)!(2n+1)(2-\delta_0^m)}{(n+m)!}} \end{aligned}$$

Here δ_0^m is the the Kronecker-delta which in this case is equal to 1 when $m = 0$, else it is equal to 0. Substituting the coefficients and polynomials in Eq. (2.18) using the relations above, the equation becomes (Hofmann-Wellenhof and Moritz, 2006):

$$U(r,\phi,\lambda) = \frac{GM}{R}\sum_{n=0}^{\infty}\left(\frac{R}{r}\right)^{n+1}\sum_{m=0}^{n}\bar{P}_{nm}(\sin\phi)\times[\bar{C}_{nm}\cos(m\lambda)+\bar{S}_{nm}\sin(m\lambda)] \tag{2.20}$$

From the gravitational potential the acceleration on a spacecraft can be determined by taking the derivative as follows:

$$\mathbf{g} = \begin{pmatrix} g_r & g_\phi & g_\lambda \end{pmatrix}^T = -\nabla U = \begin{pmatrix} -\frac{\partial U}{\partial r} & -\frac{1}{r\cos\lambda}\frac{\partial U}{\partial\phi} & -\frac{1}{r}\frac{\partial U}{\partial\lambda} \end{pmatrix}^T \tag{2.21}$$

The more degree and order coefficients are determined, the more precise the gravity field model. Different degree and order harmonics correspond with different geometrical characteristics (Hofmann-Wellenhof and Moritz, 2006). When order m is zero and degree n is not, it is classified as zonal harmonics because it depends on the latitude and not on the longitude, and can be divided in zonals since the sign changes n times. In general, the sign changes $n-m$ times in the interval $0 \leq \phi \leq \pi$. For the harmonics where n and m are equal and nonzero, the term sectorial harmonics is used. Because of the zero changes of sign over the interval in latitude($n - m$) it only changes in sign over the interval $0 \leq \lambda \leq 2\pi$ what divides the harmonics over positive and negative sectors. Every other combination where n and m are not equal and nonzero divides the sphere in compartments because it changes sign over both the intervals. These harmonics are called tesseral harmonics. Examples of all three particular harmonics are visualized in Figure 2.2.

The spherical harmonics estimation accuracy is dependent on the altitude of the spacecraft orbit. The study by Bourgeaux (2020) showed, the closer a spacecraft is to the surface, the more accurate the estimation. This is expressed by errors of a lower percentage in the estimated spherical coefficients, with respect to their estimated value, for lower altitudes.

Point-mass distribution

Another method to model the gravity field is defining a distribution of point masses, mascons (mass concentrations), over the shape of the body. One example is the simple model of Itokawa for the Hayabusa mission shown in Figure 1.6. The size of the ring indicates the mass and thus the gravitational force by the point mass. This is a very simplified distribution of only six points. A commonly used approach is defining an evenly spaced grid of points with individual masses filling the shape of the body (Werner and Scheeres, 1997). The sum of the individual masses is equal to the total mass of the asteroid. Other options are to define a non-uniform grid, or to randomly distribute masses with an uniform distribution (Bolatti, 2020).

With this method it is possible to model gravitational variations of any irregular shape and mass distribution characterizing the asteroid. The complexity and accuracy of the model is dependent on the number of mass points used. In this way, the minimal computational effort required for a desired accuracy can be selected. Nevertheless, according to Werner and Scheeres (1997), modeling the gravitational field using a evenly spaced point mass distribution has multiple deficiencies. The computational effort is higher for the same desired accuracy as harmonic modeling and significant errors remain even with large numbers of mascons.

Another technique is using the polyhedral shape model of an asteroid to construct a shape model. In Chanut et al. (2015) two models are described using the triangular facets of a shape model and connecting the vertexes with the center of the asteroid. The first model places a mascon in the centroid of the formed tetrahedron giving it a mass proportional to the volume of the tetrahedron with respect to the complete mass of the asteroid. This model with one mascon per tetrahedron is called Mascon 1. The second model, called Mascon 3, divides the tetrahedron in three parts. In the center of every part is placed a mascon proportional to the volume. The resulting mascon models for asteroid 216 Kleopatra are given in Figure 2.3a and 2.3b. These models appeared to be quite consistent with the polyhedral model with a relative error of about 0.1 km^2s^{-2} in potential, and convergent close to the surface. Especially Mascon 3 performed well close to the surface (Chanut et al., 2015).

Polyhedron gravity field

The last method to model the gravity field evaluated in this chapter is the earlier mentioned polyhedron method. In this method the asteroid is modeled as a polyhedron with a constant density. The polyhedron consists of a number of planar faces. These polygons meet at edges. By increasing the number of faces such polyhedron shape model can be made very accurate including craters, caves, overhangs or big rocks. In this way there can be dealt with the irregular shape up to high detail. The volume defined by the shape is assumed to have a constant density, what results in the total mass of the asteroid. The exterior gravitation caused by the body can be derived analytically in a closed form (Werner and Scheeres, 1997). In Figure 1.5 an example of such shape model is given.

The polyhedron model eliminates potential critical problems. First, since the gravitation can be derived in closed form analytically from the shape model, the total error can be fully reduced to errors in the shape model. Second, the polyhedron gravity model does always converge. Third, by evaluating the Laplacian of the potential it can be determined whether a point is inside or outside the shape. When

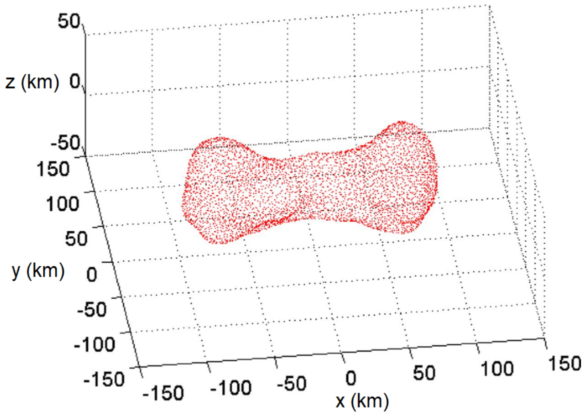

(a) Visualization of Mascon 1 model of asteroid 216 Kleopatra by (Chanut et al., 2015)

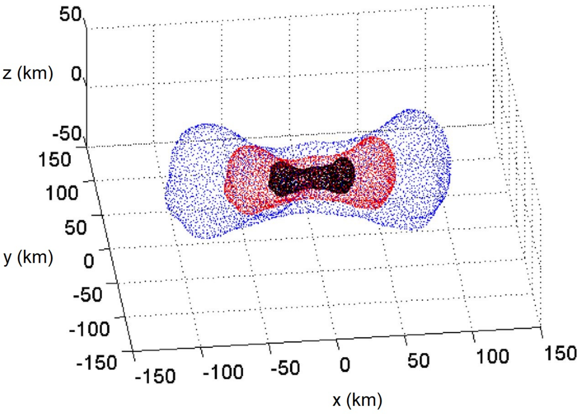

(b) Visualization of Mascon 3 model of asteroid 216 Kleopatra by (Chanut et al., 2015)

the Laplacian is equal to zero, the field point is outside the shape and when it is not zero the point is inside the shape (Werner and Scheeres, 1997). This easy way of determining whether a point is inside or outside the shape could for example avoid collision.

The gravitational potential at a field point at position $\mathbf{r}$ can be determined by summation over the faces and edges following Eq. (2.22), where ρ is the density and G the gravitational constant. Suffixes e and f specify whether an edge or face are considered, respectively (Park et al., 2010; Werner and Scheeres, 1997).

$$U(\mathbf{r}) = \frac{1}{2}G\rho \sum_{e \in edges} \mathbf{r}_e^T \mathbf{E}_e \mathbf{r}_e \cdot L_e - \frac{1}{2}G\rho \sum_{f \in faces} \mathbf{r}_f^T \mathbf{F}_f \mathbf{r}_f \cdot \omega_f \tag{2.22}$$

Each face has a normal vector $\hat{\mathbf{n}}_f$ pointing outwards. Each edge has a normal vector $\hat{\mathbf{n}}_e$ pointing outward and perpendicular to $\hat{\mathbf{n}}_f$. Every edge or face has its own dyadic product $\mathbf{E}_e$ or $\mathbf{F}_f$ respectively as defined below:

$$\begin{aligned} \mathbf{E}_e &= \hat{\mathbf{n}}_A (\hat{\mathbf{n}}_{12}^A)^T + \hat{\mathbf{n}}_B (\hat{\mathbf{n}}_{21}^B)^T \\ \mathbf{F}_f &= \hat{\mathbf{n}}_f \hat{\mathbf{n}}_f^T \end{aligned}$$

Here A and B are two faces that are connected by the edge that connects vertices P_1 and P_2 as in Figure 2.4. Dimensionless per-edge factor L_e is defined as:

$$L_e = \ln \frac{r_i + r_j + e_{ij}}{r_i + r_j - e_{ij}}, \tag{2.23}$$

where $r_i = ||\mathbf{r}_i||$, with $\mathbf{r}_i$ as the vector from field point location towards vertex P_i, and e_{ij} as the length between vertices P_i and P_j. The dimensionless per-face factor ω_f is defined as follows for a triangular face defined by vertices P_i, P_j and P_k (Park et al., 2010; Werner and Scheeres, 1997):

$$\omega_f = 2 \arctan \frac{\mathbf{r}_i \cdot \mathbf{r}_j \times \mathbf{r}_k}{r_i r_j r_k + r_i(\mathbf{r}_j \cdot \mathbf{r}_k) + r_j(\mathbf{r}_k \cdot \mathbf{r}_i) + r_k(\mathbf{r}_i \cdot \mathbf{r}_j)} \tag{2.24}$$

The gravitational acceleration at a certain field point location can then be determined by taking the derivative of the gravitational potential. This results in Eq. (2.25).

$$\mathbf{g}(\mathbf{r}) = \frac{\partial U(\mathbf{r}}{\partial \mathbf{r}} = -G\rho \sum_{e \in edges} \mathbf{E}_e \mathbf{r}_e \cdot L_e + G\rho \sum_{f \in faces} \mathbf{F}_f \mathbf{r}_f \cdot \omega_f \tag{2.25}$$

The method has relatively high requirements for computation and memory. Determining the potential requires summation over the complete surface of the polyhedron shape model. The high computational

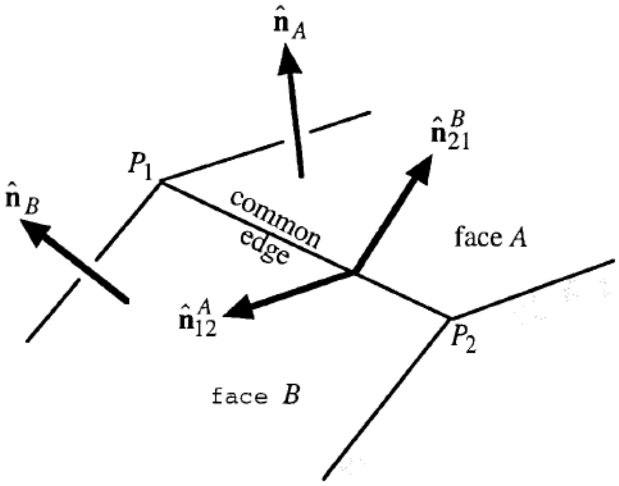

Figure 2.4: Visualization of normal vector definitions for faces and edges. From (Werner and Scheeres, 1997).

Table 2.4: Models compared on CPU time (Chanut et al., 2015).

Asteroid	**(216) kleopatra**		**(433) Eros**		**(4769) Castalia**		**(4179) Toutatis**	
CPU speed	**3.10 GHz**	**2.27 GHz**	**3.10 GHz**	**2.27 GHz**	**3.10 GHz**	**2.27 GHz**	**3.10 GHz**	**2.27 GHz**
Mascon 1	9 m 14 s	11 m 45 s	17 m 02 s	21 m 17 s	9 m 16 s	11 m 32 s	69 m 26 s	113 m 12 s
Mascon 3	11 m 37 s	19 m 48 s	25 m 55 s	36 m 28 s	11 m 39 s	19 m 46 s	105 m 07 s	194 m 58 s
Polyhedron	190 m 50 s	458 m 55 s	469 m 30 s	801 m 4 s	191 m 30 s	460 m 36 s	2338 m 12 s	4630 m 12 s

load of the polyhedron gravity field computation has been demonstrated by Chanut et al. (Chanut et al., 2015), who compared gravity field computation using the mascon distribution models described in subsection 2.3.1 with the polyhedron gravity field computation. In Table 2.4 the CPU time for two different computer speeds are shown for four different asteroid shape models. The table clearly shows the increased CPU time for computing the gravity field using the polyhedron model, for both computers and all four different asteroid shape models. Regarding autonomous navigation with limited on-board computer performance and memory storage the aspects of computational load and memory requirements shall be considered when selecting a gravity model for implementation. Also, one shall not forget the controversial assumption of a constant density. The polyhedron model can, because of its known homogeneous density and unlimited convergence, be used as reference method to discover heterogeneity or to define the nominal gravity field, to which gravity fields computed using other models can be compared (Park et al., 2010; Scheeres et al., 2020; Takahashi et al., 2013).

2.3.2. Third-body perturbation

One of the external perturbations, besides the gravitational attraction by the asteroid body, is the gravitational attraction by other celestial bodies besides the asteroid. This could, for example, be planets as Mars and Jupiter, or the Sun. The environment defined for simulation includes only the Sun as a third-body. As the Sun is at an average distance of 1.458 au from Eros, this third body perturbation is modeled as a point-mass. Therefore, the third body perturbation $\mathbf{a}_{3rd}$ caused by the Sun, with respect to the defined inertial reference frame, is given by (Wakker, 2015):

$$\mathbf{a}_{3rd} = -GM_A \frac{\mathbf{r}_B}{\|\mathbf{r}_B\|^3} + GM_S \left(\frac{\mathbf{r}_{BS}}{\|\mathbf{r}_{BS}\|^3} - \frac{\mathbf{r}_S}{\|\mathbf{r}_S\|^3} \right) \tag{2.26}$$

Here, G is the gravitational constant, M_A and M_S are the mass of the asteroid and Sun, respectively, $\mathbf{r}_B$ is the position of the spacecraft, $\mathbf{r}_S$ is the position of the Sun, and $\mathbf{r}_{BS} = \mathbf{r}_B - \mathbf{r}_S$ is the relative position of the spacecraft with respect to the Sun.

2.3.3. Solar Radiation Pressure

Besides the Sun its gravitational attraction, the photons which are emitted by the Sun generate a force on the spacecraft when they hit the body. This is another perturbing force called *solar radiation pressure (SRP)*. The SRP during a mission does influence the orbit of the spacecraft. Since the gravitational force of an asteroid relatively small compared to when orbiting a planet, the SRP has relatively high influence (Scheeres, 1999). In Kato and van der Ha (2012), the acceleration due to SRP is modeled for the Rosetta spacecraft during its mission cruise phases. During these phases the spacecraft traveled from a distance with the Sun of 0.9 au towards a distance of 5.3 au. The acceleration due to SRP appeared to range from 10^{-7} to 10^{-8} m/s^2. With a simple calculation of the point mass near an asteroid, this value can be compared with acceleration due to the gravitational pull of the asteroid. The point mass acceleration by, for example, Eros, with a gravitational parameter $\mu = (4.461 \pm 0.001) \times 10^5$ m^3/s^2 and an orbit around the Sun ranging from 1.13 till 1.76 au (Yeomans et al., 2000), at a distance d of 500 km would be $\frac{\mu}{d^2} \approx 1 \times 10^{-6}$ m/s^2. This is only an order 10 higher than the SRP force, what motivates for including this force in the simulation.

According to Markley and Crassidis (2014), the SRP force can be modeled according to the following equation:

$$\mathbf{F}_{SRP} = -P_{\odot} \sum_{i=1}^{N} \cos\theta_i A_i \left((1-\epsilon_i)\mathbf{e}_{S/B,i} + 2\epsilon_i \cos\theta_i \hat{\mathbf{n}}_i \right) \tag{2.27}$$

Here, the spacecraft is modeled as a collection of N planes, each with a surface area A_i, normal vector $\hat{\mathbf{n}}_i$, and reflectivity coefficient ϵ_i. The symbol $P_{\odot}$ indicates the solar radiation pressure, θ_i the angle between the Sun vector and the plane normal vector, and $\mathbf{e}_{S/B,i}$ the unit vector directed towards the Sun from the spacecraft.

2.3.4. Overview

As the simulator is required to be able to simulate the spacecraft inside the Brillouin sphere, the polyhedron model is selected as the gravity model used for simulation. The spherical harmonics model is not used for simulation, but only used for comparison of estimated gravity field accuracies. The point-mass distribution is used in the state estimator, which is explained in more detail in chapter 3, because of its relatively low computational costs, and large region of convergence.

As the Sun is the main perturbing body, its influences are included in the modeled asteroid environment. Other possible disturbing bodies as Jupiter, Mars or Earth are assumed to be too far away to have a negligible contribution. Thereby, it is not complicated to include this perturbation, knowing the Sun's gravitational parameter. Besides this third body perturbation, the Sun also unduces the SRP force. Bourgeaux (2020) showed that whether or not these forces are included in the gravity field estimation can make a difference in its performance. Therefore, it is decided to include these perturbation in the simulation.

2.4. Rotational motion

Besides position and velocity, also the attitude of a spacecraft is of importance during a mission. If a spacecraft has the desired attitude, the instruments give the best measurements. Elsewise, the control system should correct to reach the desired attitude. The quaternions, which are used to describe the attitude, are already introduced in subsection 2.2.1. In this section, it is described how these quaternions evolve over time according to dynamic and kinematic laws. A distinction can be made between the attitude of our two bodies of interest, the spacecraft and asteroid.

2.4.1. Spacecraft rotation

As a body has a certain angular velocity described by the angular velocity vector $\boldsymbol{\omega} = (\omega_1, \omega_2, \omega_3)^T$, the quaternion vector $\mathbf{q}$ changes over time. According to Wie (2008), the attitude kinematics equation adapted for the spacecraft body is:

$$\dot{\mathbf{q}}_{B/I} = \frac{1}{2}\boldsymbol{\omega}^B_{B/I} \otimes \mathbf{q}_{B/I} = \frac{1}{2}\boldsymbol{\Omega}(\boldsymbol{\omega}^B_{B/I})\mathbf{q}_{B/I} \tag{2.28}$$

with $\boldsymbol{\omega}^B_{B/I}$ describing the angular velocity of the body-frame with respect to the inertial frame expressed in the body-frame, and $\boldsymbol{\Omega}(\boldsymbol{\omega})$ as:

$$\boldsymbol{\Omega} = \boldsymbol{\omega}\otimes = \begin{bmatrix} -[\boldsymbol{\omega}\times] & \boldsymbol{\omega} \\ -\boldsymbol{\omega}^T & 0 \end{bmatrix} = \begin{bmatrix} 0 & \omega_3 & -\omega_2 & \omega_1 \\ -\omega_3 & 0 & \omega_1 & \omega_2 \\ \omega_2 & -\omega_1 & 0 & \omega_3 \\ -\omega_1 & -\omega_2 & -\omega_3 & 0 \end{bmatrix} \tag{2.29}$$

This equation describes the behavior of the attitude over time dependent on the angular velocity vector. This angular velocity can also evolve over time, depending on the forces working on the body. These forces can induce a torque, which influences the change in angular velocity. The dynamics of the angular velocity are described by Euler's rotational equation (Wie, 2008), which, adapted for the spacecraft body is given by:

$$\dot{\boldsymbol{\omega}}^B_{B/I} = \mathbf{J}^{-1}(-\boldsymbol{\omega}^B_{B/I} \times (\mathbf{J}\boldsymbol{\omega}) + \boldsymbol{\tau}) \tag{2.30}$$

Here, the symbol $\mathbf{J}$ indicates the moment of inertia tensor of the body, and the symbol $\boldsymbol{\tau}$ indicates the resultant torque working on the body. As $\boldsymbol{\tau}$ is a resultant torque, this can be the sum of multiple torques. It could be for example be an internal torque, which is induced due to the control system, or external torques due to disturbances.

Solar Radiation Pressure Torque

Besides the SRP force caused by the emitted photons of the Sun, these also influence the rotational motion of the spacecraft. According to Markley and Crassidis (2014) this gravitational torque can be obtained with the following equation:

$$\boldsymbol{\tau}_{SRP} = \sum_{i=1}^{\text{planes}} \mathbf{r}_{B,i} \times \mathbf{F}_{SRP,B,i} \tag{2.31}$$

In this equation, the sum is taken over the product of the center of plane positions with respect to the body-fixed frame $\mathbf{r}_{B,i}$ and the SRP force per plane $\mathbf{F}_{SRP,B,i}$.

Gravity Gradient Torque

Another external torque that could influence the attitude of the spacecraft is the gravity gradient torque. This torque is induced by differences in the gravitational attraction over the dimensions of the spacecraft body. By describing the spacecraft body by N number of point-masses, the gravity gradient torque can be approximated, using the following equation (Razgus et al., 2017; Wie, 2008):

$$\boldsymbol{\tau}_{GG} = \sum_{i=1}^{N} \mathbf{r}_{B,i} \times m_i \mathbf{g}_{B,i} \tag{2.32}$$

Here, $\mathbf{r}_{B,i}$ is the position of, m_i the mass of, and $\mathbf{g}_{B,i}$ the acceleration on the i^{th} point-mass. For this numerical approach to approximate the gravity gradient torque, it yields that the more point-masses are used to model the spacecraft, the more accurate the model becomes with reality. However, It is chosen to neglect this torque as it increases simulation time tremendously and only influences the rotational motion of the spacecraft directly. Indirectly it influences the solar radiation pressure, which depends on this attitude. However, in the navigation system, this force is assumed known and thus not influencing the estimation performance. As it is chosen not to estimate the attitude of the spacecraft and the acceleration dependent on this attitude is assumed known, this simulation time increasing torque is ignored. The simulation time increase is due to the the fact that the gravity gradient torque requires the gravitational acceleration to be determined for each of the point masses which models the spacecraft, according to Eq. (2.32). As the minimum number of point-masses required to model the spacecraft dimensions is 16, the summation as in Eq. (4.6) has to be done 17 times each time step.

2.4.2. Asteroid rotation

During the thesis work, the asteroid is assumed to rotate with a constant speed around the z-axis. This makes propagation of the attitude of the asteroid only require the kinematic equation:

$$\dot{\mathbf{q}}_{A/I} = \frac{1}{2}\boldsymbol{\omega}_{A/I}^{A} \otimes \mathbf{q}_{A/I} \tag{2.33}$$

Here, again, $\boldsymbol{\omega}_{A/I}\otimes$ can be determined using Eq. 2.29. The fixed angular velocity makes the angular velocity vector of the asteroid-fixed frame with respect to the inertial frame expressed in the asteroid-fixed frame equal to: $\boldsymbol{\omega}_{A/I}^{A} = (0, 0, \omega_z)^T$.

3

Navigation

Before investigating performances of navigation systems near asteroids, one shall have insights in how navigation systems work. A major element in navigation systems is the navigation filter. Such filter estimates the state of the spacecraft using input from, for example, sensors. An established type of filter is the Kalman filter, of which the basic definitions are highlighted in section 3.1. As a solution for non-linear system as, for example, asteroid environments, the Extended Kalman filter is explained in section 3.2. Also, in existing software used by Bourgeaux (2020), Kalman filters are used to estimate the state of a simulated spacecraft over time. The Extended Kalman Filter is compared by Bourgeaux with the Unscented Kalman Filter. The Unscented Kalman Filter is also capable of handling non-linear systems. Bourgeaux showed that the Unscented Kalman Filter had a comparable performance as the EKF and is easier to implement when using spherical harmonics. Therefore, also the Unscented Kalman Filter is addressed in section 3.3. After these explanations about the two different Kalman filter types, the method applied in Park et al. (2010) for mascon gravity field estimation is evaluated. Finally, the two Kalman filter types are discussed and a in section 3.5.

3.1. Kalman Filter

A Kalman filter (KF) is an estimator based on a very effective and versatile procedure. It estimates the state combining a dynamical system with uncertainties and noisy sensor outputs. Examples of books in which the Kalman filter is described are Haykin (2001) and Mooij E (2019). The simplest example of a KF is the Linear Kalman Filter (LKF). This filter estimates the state $\mathbf{x}_k$ of a linear system which can be described as:

$$\mathbf{x}_{k+1} = \mathbf{\Phi}_k \mathbf{x}_k + \mathbf{B}_k \mathbf{u}_{k+1} + \mathbf{w}_k \tag{3.1}$$

Using the measurements $\mathbf{z}_k$:

$$\mathbf{z}_k = \mathbf{H}_k \mathbf{x}_k + \mathbf{v}_k \tag{3.2}$$

Here $\mathbf{u}$ represents the control input, $\mathbf{\Phi}$ the state-transition matrix which defines how the state relates with the next state, $\mathbf{B}$ the control matrix, $\mathbf{H}_k$ the measurement matrix, which indicates how measurements are related to the state, $\mathbf{w}$ the system noise, and $\mathbf{v}$ the measurement noise. The index k indicates the time step.

3.2. Extended Kalman Filter

However, such linear system does not represent a system that will describe the situation in which the spacecraft will be placed in. This requires a KF that can handle non-linear systems such as the Extended Kalman Filter (EKF). The following equation can express the non-linear system:

$$\mathbf{x}_{k+1} = \mathrm{f}(\mathbf{x}_k, \mathbf{u}_k, \mathbf{w}_k) \tag{3.3}$$

with measurements

$$\mathbf{z}_k = \mathrm{h}(\mathbf{x}_k, \mathbf{v}_k) \tag{3.4}$$

The EKF estimates the next state using first-order Taylor series approximations of the system around the current state estimate. The noises $\mathbf{w}_k$ and $\mathbf{v}_k$ are assumed to be uncorrelated (white noise) and their probability distribution is given by:

$$p(\mathbf{v}_k) \sim N(0, \mathbf{R}_k) \tag{3.5}$$

$$p(\mathbf{w}_k) \sim N(0, \mathbf{Q}_k) \tag{3.6}$$

where $\mathbf{R}$ and $\mathbf{Q}$ are the noise of the measurement device and the uncertainty in the system model, respectively. Although white noise cannot exist, it is often used for design and analysis. The white noise is for the system often identical to the real noise, as it only responds to a range of frequencies defined by the so-called ”bandpass” (Welch and Bishop, 2001).

An estimation is done in two steps. First, an *a-priori* estimate is obtained, after which an *a-posteriori* estimation is performed. The *a-priori* estimate $\hat{\mathbf{x}}_k^-$ is an estimate using only the dynamical model. The *a-priori* estimate is then updated and refined into the *a-posteriori* estimate $\hat{\mathbf{x}}_k$ by including the measurements. The errors of these *a-priori* and *a-posteriori* estimates $\mathbf{e}_{xk}^-$ and $\mathbf{e}_{xk}$ are defined as:

$$\mathbf{e}_{xk}^- = \mathbf{x}_k - \hat{\mathbf{x}}_k^- \tag{3.7}$$

$$\mathbf{e}_{xk} = \mathbf{x}_k - \hat{\mathbf{x}}_k \tag{3.8}$$

Using the *a-posteriori* estimate from the previous timestep, the new *a-priori* estimate can be derived and measurements can be estimated by using:

$$\hat{\mathbf{x}}_{k+1}^- = \mathrm{f}(\hat{\mathbf{x}}_k, \mathbf{u}_{k+1}, \mathbf{0}) \tag{3.9}$$

$$\hat{\mathbf{z}}_k = \mathrm{h}(\hat{\mathbf{x}}_k^-, \mathbf{0}) \tag{3.10}$$

In the initializing step, the a-priori estimate is derived using the initial state $\hat{\mathbf{x}}_0$ and covariance matrix $\mathbf{P}_0$, which are defined as:

$$\hat{\mathbf{x}}_0 = E[\mathbf{x}_0] \tag{3.11}$$

$$\mathbf{P}_0 = E[(\mathbf{x}_0 - E[\mathbf{x}_0])(\mathbf{x}_0 - E[\mathbf{x}_0])^T] \tag{3.12}$$

Linearization of the Eqs. (3.9) and (3.10) gives:

$$\mathbf{x}_{k+1} \approx \hat{\mathbf{x}}_{k+1}^- + \mathbf{\Phi}_k \left(\mathbf{x}_k - \hat{\mathbf{x}}_k\right) + \mathbf{W}_k \mathbf{w}_k \tag{3.13}$$

$$\mathbf{z}_k \approx \hat{\mathbf{z}}_k^- + \mathbf{H}_k \left(\mathbf{x}_k - \hat{\mathbf{x}}_k\right) + \mathbf{V}_k \mathbf{v}_k \tag{3.14}$$

Here, $\mathbf{\Phi}$, $\mathbf{B}$, $\mathbf{W}$ and $\mathbf{V}$ indicate the Jacobian matrices of the system used for linearization defined as:

$$\mathbf{\Phi}_k = \left.\frac{\partial \mathbf{f}}{\partial \mathbf{x}}\right|_{(\hat{\mathbf{x}}_k, \mathbf{u}_{k+1}, \mathbf{0})} \tag{3.15}$$

$$\mathbf{H}_k = \left.\frac{\partial \mathbf{h}}{\partial \mathbf{x}}\right|_{\left(\hat{\mathbf{x}}_k^-, \mathbf{0}\right)} \tag{3.16}$$

$$\mathbf{V}_k = \left.\frac{\partial \mathbf{h}}{\partial \mathbf{v}}\right|_{\left(\hat{\mathbf{x}}_k^-, 0\right)} \tag{3.17}$$

$$\mathbf{W}_k = \left.\frac{\partial \mathbf{f}}{\partial \mathbf{w}}\right|_{(\hat{\mathbf{x}}_k, \hat{\mathbf{u}}_{k+1}, \mathbf{0})} \tag{3.18}$$

The Jacobian $\mathbf{\Phi}$ is also called the state-transition matrix. The *a-priori* prediction error $\mathbf{e}_{xk}^-$ and measurement residual $\mathbf{e}_{zk}^-$ are approximated by:

$$\mathbf{e}_{xk}^- = \mathbf{x}_k - \hat{\mathbf{x}}_k^- \approx \mathbf{\Phi}_{k-1}(\mathbf{x}_{k-1} - \hat{\mathbf{x}}_{k-1}) + \epsilon_k \tag{3.19}$$

$$\mathbf{e}_{zk}^- = \mathbf{z}_k - \hat{\mathbf{z}}_k^- \approx \mathbf{H}_k(\hat{\mathbf{e}}_{xk}^-) + \boldsymbol{\eta}_k \tag{3.20}$$

Here η and ϵ are the linear approximations of noises $\mathbf{v}$ and $\mathbf{w}$ with distributions:

$$p\left(\epsilon_k\right) \sim N\left(\mathbf{0}, \mathbf{W}_{k-1}\mathbf{Q}_{k-1}\mathbf{W}_{k-1}^T\right) \tag{3.21}$$

$$p\left(\eta_k\right) \sim N\left(\mathbf{0}, \mathbf{V}_k\mathbf{R}_k\mathbf{V}_k^T\right) \tag{3.22}$$

To estimate the prediction error, the difference can be computed between the *a-posteriori* and *a-priori* errors in equations (3.7) and (3.8). This error shall be equal to the state update for which Kalman gain $\mathbf{K}$ is defined. This gives:

$$\hat{\mathbf{e}}_k = \hat{\mathbf{x}}_k - \hat{\mathbf{x}}_k^- = \mathbf{K}(\hat{\mathbf{e}}_{zk}^-) \tag{3.23}$$

Using this equation, the *a-posteriori* state estimation can be written as:

$$\hat{\mathbf{x}}_k = \hat{\mathbf{x}}_k^- + \mathbf{K}(\mathbf{z}_k - \hat{\mathbf{z}}_k) \tag{3.24}$$

This results in the covariance matrix $\mathbf{P}$ and gain equations:

$$\mathbf{P}_{k+1}^- = \mathbf{\Phi}_k\mathbf{P}_k\mathbf{\Phi}_k^T + \mathbf{W}_k\mathbf{Q}_k\mathbf{W}_k^T \tag{3.25}$$

$$\mathbf{K} = \mathbf{K}_k = \mathbf{P}_k^-\mathbf{H}_k^T\left(\mathbf{H}_k\mathbf{P}_k^-\mathbf{H}_k^T + \mathbf{V}_k\mathbf{R}_k\mathbf{V}_k^T\right)^{-1} \tag{3.26}$$

where:

$$\mathbf{P}_k = (\mathbf{I} - \mathbf{K}_k\mathbf{H}_k)\mathbf{P}_k^- \tag{3.27}$$

These steps are repeated over time by deriving the *a-priori* estimate from the previous *a-posteriori* estimate.

3.3. Unscented Kalman Filter

An alternative for the EKF is the Unscented Kalman Filter (UKF) using Unscented Transformation (UT). UT is defined by Wan and Van Der Merwe (2000) as a method for calculating the statistics of a random variable which undergoes a nonlinear transformation. It describes a set of sample points instead of only one point, resulting in a more precise estimate. By calculating the statistics of carefully chosen sample points instead of only one point it is able to capture the posterior mean and covariance to the third order Taylor series expansion (Wan and Van Der Merwe, 2000).

Unscented transformation works as follows. Imagine a random variable $\mathbf{x}$ of dimension L in non-linear system $\mathbf{y} = g(\mathbf{x})$. A matrix of $2L + 1$ so-called sigma vectors χ_i is formed, with $i \in \{0, ..., 2L\}$, to calculate the statistics of $\mathbf{y}$. These vectors are assigned a weight W_i. The sigma vectors are defined as follows:

$$\begin{aligned}
\chi_{0,k} &= \bar{\mathbf{x}}_k \\
\chi_i &= \bar{\mathbf{x}} + \left(\sqrt{(L+\lambda)\mathbf{P}_\mathbf{x}}\right)_i && i = 1, \dots, L \\
\chi_i &= \bar{\mathbf{x}} - \left(\sqrt{(L+\lambda)\mathbf{P}_\mathbf{x}}\right)_{i-L} && i = L+1, \dots, 2L \\
W_0^{(m)} &= \lambda/(L+\lambda) \\
W_0^{(c)} &= \lambda/(L+\lambda) + \left(1 - \alpha^2 + \beta\right) \\
W_i^{(m)} &= W_i^{(c)} = 1/\{2(L+\lambda)\} && i = 1, \dots, 2L
\end{aligned} \tag{3.28}$$

Here the covariance is indicated by $\mathbf{P}_x$, the mean of the random variable by $\bar{\mathbf{x}}$. $\lambda = \alpha^2(L+\kappa)$ and κ are scaling parameters, where α determines the spread of the sigma points and β is used influence the distribution of $\mathbf{x}$ with prior knowledge. Propagating the sigma vectors using $\mathcal{Y}_i = g\left(\chi_i\right)$, the mean and covariance for $\mathbf{y}$ can than be approximated using:

$$\bar{\mathbf{y}} \approx \sum_{i=0}^{2L} W_i^{(m)} \mathcal{Y}_i \tag{3.29}$$

$$\mathbf{P}_\mathbf{y} \approx \sum_{i=0}^{2L} W_i^{(c)} \{\mathcal{Y}_i - \bar{\mathbf{y}}\}\{\mathcal{Y}_i - \bar{\mathbf{y}}\}^T \tag{3.30}$$

With an extension of UT on Eq.(3.24) from the EKF, the UKF is made. Here the random variable is defined as a concatenation of the state and noise variables as $\mathbf{x}_k^a = \left(\mathbf{x}_k^T\ \mathbf{v}_k^T\ \mathbf{w}_k^T\right)^T$. The sigma points and weights can be calculated using Eq.(3.28) realizing $\chi^a = \left((\chi^{\mathbf{x}})^T\ (\chi^{\mathbf{v}})^T\ (\chi^{\mathbf{w}})^T\right)^T$. The time update can be performed by using:

$$\mathcal{X}_{k|k-1}^x = \mathbf{f}\left(\mathcal{X}_{k-1}^x, \mathcal{X}_{k-1}^v\right) \tag{3.31}$$

$$\hat{\mathbf{x}}_k^- = \sum_{i=0}^{2L} W_i^{(m)} \mathcal{X}_{i,k|k-1}^x \tag{3.32}$$

$$\mathbf{P}_k^- = \sum_{i=0}^{2L} W_i^{(c)} \left(\mathcal{X}_{i,k|k-1}^x - \hat{\mathbf{x}}_k^-\right)\left(\mathcal{X}_{i,k|k-1}^x - \hat{\mathbf{x}}_k^-\right)^T \tag{3.33}$$

$$\mathcal{Z}_{k|k-1} = \mathbf{h}\left(\mathcal{X}_{k|k-1}^x, \mathcal{X}_{k-1}^w\right) \tag{3.34}$$

$$\hat{\mathbf{z}}_k^- = \sum_{i=0}^{2L} W_i^{(m)} \mathcal{Z}_{i,k|k-1} \tag{3.35}$$

The equations for updating the state based on the measurements are given by:

$$\mathbf{P}_{\hat{\mathbf{z}}_k\hat{\mathbf{z}}_k} = \sum_{i=0}^{2L} W_i^{(c)} \left[\mathcal{Z}_{i,k|k-1} - \hat{\mathbf{z}}_k^-\right]\left[\mathcal{Z}_{i,k|k-1} - \hat{\mathbf{z}}_k^-\right]^T \tag{3.36}$$

$$\mathbf{P}_{\mathbf{x}_k\mathbf{z}_k} = \sum_{i=0}^{2L} W_i^{(c)} \left[\mathcal{X}_{i,k|k-1} - \hat{\mathbf{x}}_k^-\right]\left[\mathcal{Z}_{i,k|k-1} - \hat{\mathbf{z}}_k^-\right]^T \tag{3.37}$$

$$\mathbf{K} = \mathbf{P}_{\mathbf{x}_k\mathbf{z}_k}\mathbf{P}_{\tilde{\mathbf{z}}_k\tilde{\mathbf{z}}_k}^{-1} \tag{3.38}$$

$$\hat{\mathbf{x}}_k = \hat{\mathbf{x}}_k^- + \mathbf{K}\left(\mathbf{z}_k - \hat{\mathbf{z}}_k^-\right) \tag{3.39}$$

$$\mathbf{P}_k = \mathbf{P}_k^- - \mathbf{K}\mathbf{P}_{\tilde{\mathbf{z}}_k\tilde{\mathbf{z}}_k}\mathbf{K}^T \tag{3.40}$$

Again, the steps can be iterated over time using the *a-posteriori* estimate to determine the next *a-priori* estimate.

3.4. Direct estimation

An approach to include the asteroid its mass distribution in state estimation is given by Park et al. (2010). The done study describes how to estimate the density of finite elements inside the asteroid shape directly from radiometric measurements. Here, a spacecraft is simulated in a trajectory around Itokawa. Itokawa is modeled using a finite number of cubes or spheres as shown in Figure 3.1. Both the cube- as the sphere-elements models are used for density distribution estimation. A Square Root Information Filter (SRIF) was used to perform a covariance analysis. It appeared that this finite element based approach can provide a good approximation of the polyhedral gravity field. The accuracy depends on the resolution of the finite elements and field-point distance.

When the densities are assigned to the elements, the gravitational potential and acceleration can be computed using these densities according to the following equations:

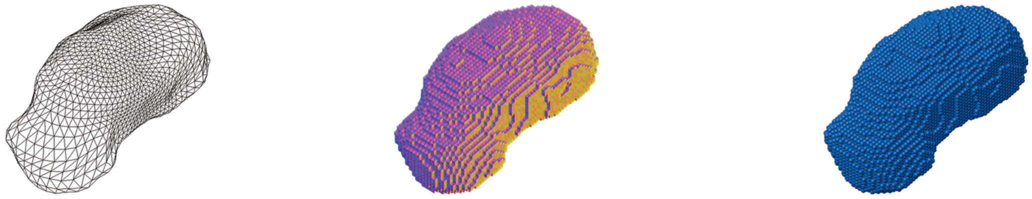

a) Polyhedron model (3688 faces) **b) Finite-cube shape model (26311 elements)** **c) Finite-sphere shape model (26311 elements)**

Figure 3.1: Differences between shape models by (Park et al., 2010).

- Cubes:

$$U_c(\mathbf{r}) = \sum_{i\in \text{ cubes}} \left(\frac{1}{2} G\rho_i \sum_{e\in \text{ edges}} \mathbf{r}_e^T \mathbf{E}_e \mathbf{r}_e \cdot L_e - \frac{1}{2} G\rho_i \sum_{f\in \text{ faces}} \mathbf{r}_f^T \mathbf{F}_f \mathbf{r}_f \cdot \omega_f \right) \tag{3.41}$$

$$\frac{\partial U_c}{\partial \mathbf{r}} = \sum_{i\in \text{ cubes}} \left(-G\rho_i \sum_{e\in \text{ edges}} \mathbf{E}_e \mathbf{r}_e \cdot L_e + G\rho_i \sum_{f\in \text{ faces}} \mathbf{F}_f \mathbf{r}_f \cdot \omega_f \right) \tag{3.42}$$

- Spheres:

$$U_m(\mathbf{r}) = \sum_{i\in \text{ spheres}} \frac{4\pi}{3} r_{mi}^3 G\rho_i \frac{1}{\|\mathbf{r} - \mathbf{r}_i\|} \tag{3.43}$$

$$\frac{\partial U_m}{\partial \mathbf{r}} = \sum_{i\in \text{ spheres}} -\frac{4\pi}{3} r_{mi}^3 G\rho_i \frac{\mathbf{r} - \mathbf{r}_i}{\|\mathbf{r} - \mathbf{r}_i\|^3} \tag{3.44}$$

As can be observed, the cubic elements are considered as distinguishable small polyhedrons applying the theory described in Figure 2.3.1, while the spheres are considered point masses with a position $\mathbf{r}_i$ and radius r_{mi}. The total potential and acceleration is calculated by summing up the influences of all different elements (Park et al., 2010).

The state defined for estimation by Park et al. (2010) is defined as:

$$\mathbf{x} = \begin{pmatrix} \mathbf{r} \\ \mathbf{v} \\ \boldsymbol{\rho} \end{pmatrix}, \tag{3.45}$$

consisting of position vector $\mathbf{r}$, velocity vector $\mathbf{v}$ and density array $\boldsymbol{\rho} = (\rho_1, \rho_2, ..., \rho_N)^T$ containing the densities of all N elements.

Results for the finite sphere model covariance analysis done by Park et al. (2010) are given in Figure 3.2 and Figure 3.3. The figures show a clear improvement of the estimation accuracy at lower altitudes. A remarkable observation is that the outer point-masses are estimated with a lower uncertainty. The cubes appeared to give about the same results in accuracy. Nevertheless, spheres are easier to implement and are computationally faster. The study showed that the finite element method is a promising technique for implementation in close-proximity navigation, because measurements below Brillouin sphere can be used. A disadvantage of the method is the error caused by neglecting the surface variation.

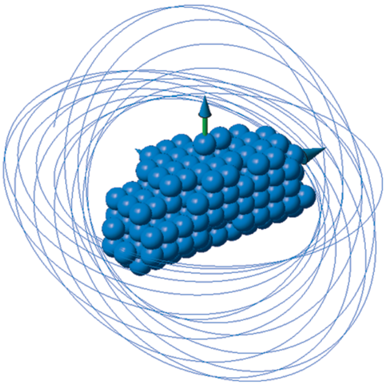

a) 3-D trajectory and finite-sphere shape model (211 elements)

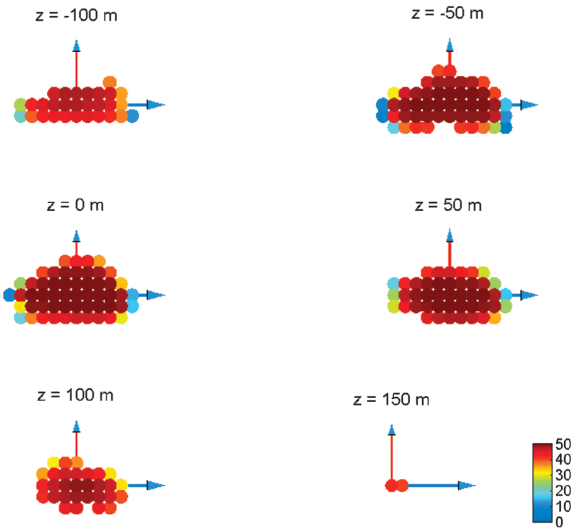

b) Density uncertainties along *x*-*y* cross sections (%)

Figure 3.2: Results of covariance analysis for simulation of trajectory around Itokawa with semi-major axis of 823 meters as initial condition; a) visualization of simulated trajectory and finite-sphere shape model(211 elements); b) resulting density uncertainties along x-y cross section (%) (Park et al., 2010)

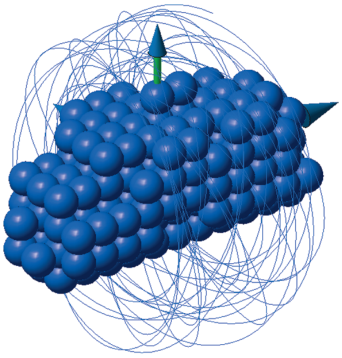

a) 3-D trajectory and finite-sphere shape model (211 elements)

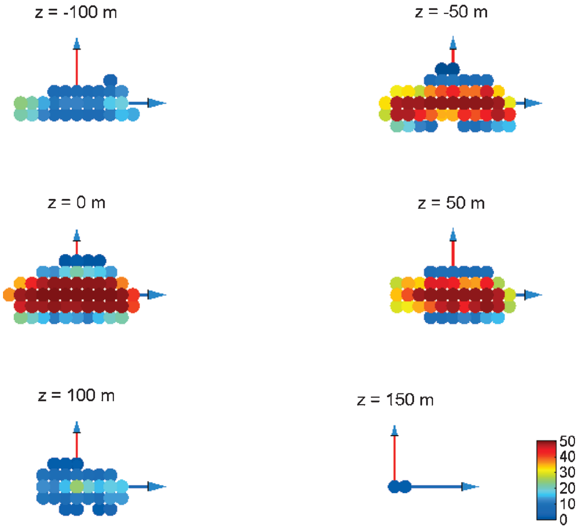

b) Density uncertainties along *x*-*y* cross sections (%)

Figure 3.3: Results of covariance analysis for simulation of trajectory around Itokawa with semi-major axis of 199 meters as initial condition; a) visualization of simulated trajectory and finite-sphere shape model(211 elements); b) resulting density uncertainties along x-y cross section (%) (Park et al., 2010)

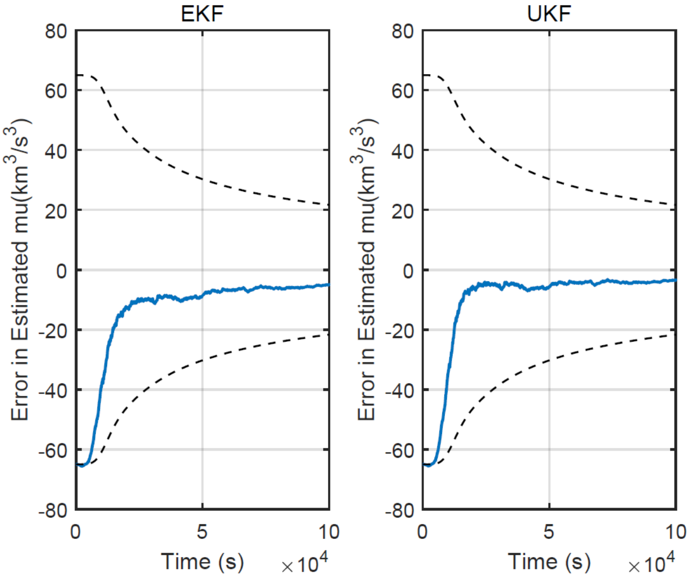

Figure 3.4: Error in estimating μ of Eros with initial condition x_0 = [2500000] and standard deviations of 100 m for position and 10 m/s for velocity in the noise covariance matrix by Bourgeaux (2020).

3.5. Discussion

A Kalman filter is an estimator that is based on a very effective and versatile procedure. It estimates the state combining a dynamical system with uncertainties and noisy sensor outputs. The linear Kalman filter would have its shortcomings on the dynamical system of such autonomous mission towards an asteroid. The Extended Kalman Filter (EKF) is a solution, because of its ability to handle nonlinear systems using a first-order Taylor series approximation around the estimate (Mooij E, 2019). Another solution was found in the Unscented Kalman Filter (UKF). This Kalman filter uses Unscented Transformation. It describes a set of sample points instead of only one point, resulting in a more precise estimate. By calculating the statistics of carefully chosen sample points instead of only one point, it is able to capture the posterior mean and covariance up to the third order Taylor series expansion (Wan and Van Der Merwe, 2000).

Bourgeaux (2020) gave preference to the UKF over the EKF. Especially, because the algorithm was easier to implement as the Jacobian matrix increases when increasing the order and degree of expansions. This would require analytical expressions of the derivatives for each state parameter. Also, the UKF performed slightly better when estimating only the μ parameter with large noise measurements as can be seen in Figure 3.4. Because of these reasons, Bourgeaux (2020) decided to do higher order estimations using the UKF.

Regarding computational costs, literature gives different answers. As for example, it is stated by Julier and Uhlmann (2004) and Wan and Van Der Merwe (2000) the computational cost and complexity of the UKF algorithm are of the same order of magnitude as the EKF, while St-Pierre and Gingras (2004) demonstrates the computational costs of the UKF are significantly higher when implemented in an integrated navigation information system. The results of these study, shown in Table 3.1, show a clear increase in computational time. This study simulated a car on a road, using measurements of a real car traveling on the same route as used in the simulator. The system fused four types of measurements (GPS, IMU, Odometer, Inclinometer). As stated in the study, the increase in computational time is related to the evaluation of 75 sigma points using the UKF, instead of one point using the EKF. It indicates the computational time of the UKF depends on the number of sigma points. The preference for one of the two navigation system appears to depend on multiple aspects.

The models used by Park et al. (2010) showed promising results with regards to using finite elements for direct estimation. Because the spherical shaped elements have lower computational costs and give

Table 3.1: Mean computational time for position estimation (St-Pierre and Gingras, 2004)

EKF (s)	UKF (s)	Gain(%)
0.0028	0.0658	-2250

similar results, these are beneficial over the cubic shaped elements. As the spheres are considered point masses, with a fixed position in a regular grid, it gives a clear example of a way to implement mascon model parameters in state estimation. However, since the finite model is bound to a regular grid and finding the real density distributions is not the main focus of this thesis, the density array in the state is replaced by the mascon gravitational parameters $\mu = GM$.

This gravity field model will be implemented in an EKF. By using an augmented state definition simular to Eq. (3.45), the state can get lengthy. Using the UKF would require the system to calculate a lot of sigma point each time step. Therefore, a UKF would be computationally expensive as it calculates multiple sigma points for each state element. Also, in comparison to when using the spherical harmonics model, the derivatives in the state transition matrix, Eq. (3.15), are easier to derive analytically. As the performance differences found by Bourgeaux (2020) were small, the EKF is preferred above the UKF and will be used for state estimation.

4

Software Design

In this chapter, there is elaborated on the structure of the used software. The general structure is addressed in section 4.1. The software consists of two systems, the real-world simulator and the navigation system. The real-world simulator is explained in section 4.2, after which in section 4.3 the navigation system is addressed.

4.1. Top-level architecture

Figure 4.1 shows the main structure of the software. As visualized in the figure, a spacecraft trajectory in an asteroid environment is simulated. The acceleration $\mathbf{a}$ the spacecraft would experience in the defined environment is calculated. The existing software uses spherical harmonics to determine the gravitational acceleration $\mathbf{a}_{SH}$ by the asteroid. The spherical harmonic coefficients can be based on measurements done by real missions or can be derived from the constant-density polyhedron model. Besides the gravitational acceleration, the model includes solar radiation pressure $\mathbf{a}_{SRP}$ and 3rd body perturbation by the Sun $\mathbf{a}_{g,Sun}$. The simulation is done to determine the sensor measurements the spacecraft would obtain during the mission. Since the focus of this study is on the influence of the in the navigation system implemented gravity model, it is assumed the measurements only experience noise. The noise is added to the simulated ”real” trajectory of the spacecraft and taken as input for the navigation system.

For this study, the implemented spherical harmonics gravity model will be replaced by the polyhedron model. The algorithm to calculate the polyhedron gravitational acceleration, as written by Razgus et al. (2017) and Werner (1997), is adjusted to be able to include density heterogeneity in the asteroid model. The real states $\mathbf{x}_{prop}$ over time are saved to be used as reference trajectory for the estimated trajectory.

The navigation software will consist of a state estimating Kalman filter. This Kalman filter will be an Extended Kalman Filter (EKF). Since the state of for estimation can become lengthy, the EKF is considered as the more efficient option. As mentioned in chapter 3, the UKF is computationally more expensive because of the calculation of multiple sigma points. Bourgeaux (2020) pointed out the accuracy difference is small. Because the derivation for a point-mass model is considered as less complicated, the EKF has been selected for analysis, as this is the more obvious choice. In this Kalman filter, the mascon gravity field will be implemented and the gravitational parameter of each modeled mascon is estimated.

4.2. Real-World simulator

To obtain measurements required as input for the navigation system, a real-world simulator is made. The structure of the real-world simulator is shown in Figure 4.2.

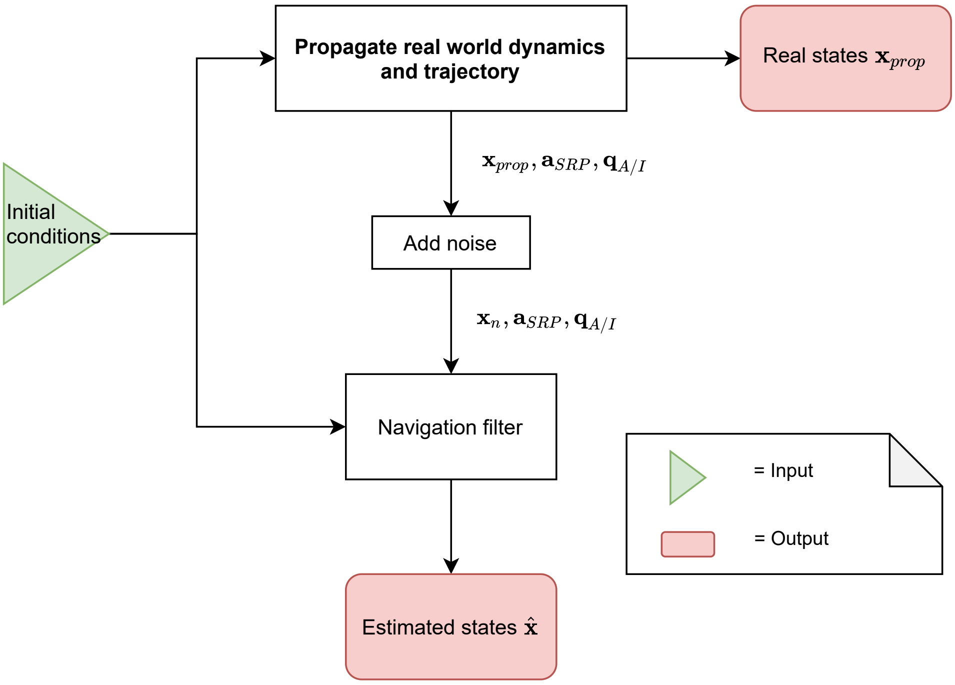

Figure 4.1: Top-level structure of the software.

4.2.1. Spacecraft model

For the spacecraft model, the model defined by Razgus et al. (2017) is used. This spacecraft is based on the Rosetta mission orbiter. Below the dimensions, mass properties and reflectance properties of this spacecraft are given.

- **Dimensions**
  The spacecraft consists of a body and two solar panels. The body is a box of 2.1×2.0×2.8 meters along the X-, Y- and Z-axis of the body-frame, respectively. The center of figure is in the body frame origin. The two solar panels are attached at the points (0 1 0) and (0 -1 0) with 1 m between the beginning of the solar panel area and the attachment point. The 14×2.3 m panels are placed on the YZ-plane and elongated along the Y-axis. In Figure 4.3, the simplified Rosetta spacecraft model by Razgus et al. (2017) is given. The solar panels are assumed to have negligible thickness.

- **Mass properties**
  The dry mass of Rosetta is about 1300 kg. Including the fuell, the total mass of the spacecraft was 3000 kg during launch [1]. At rendezvous with its target body, this mass M_{SC} was decreased towards about 2100 kg (Razgus et al., 2017). As the mass of the solar panels are estimated to have a mass M_{sp} of 75 kg each, the body has a mass M_b of 1950 kg. When assuming a constant density through its components, the spacecraft's inertia tensor $\mathbf{I}_{SC}$ can be calculated using the following equations:

$$\mathbf{I}_{SC} = \mathbf{I}_b + 2\mathbf{I}_s \tag{4.1}$$

---

[1] NASA archive: http://nssdc.gsfc.nasa.gov/nmc/spacecraftDisplay.do?id=2004-006A; accessed at: 07/2/2021

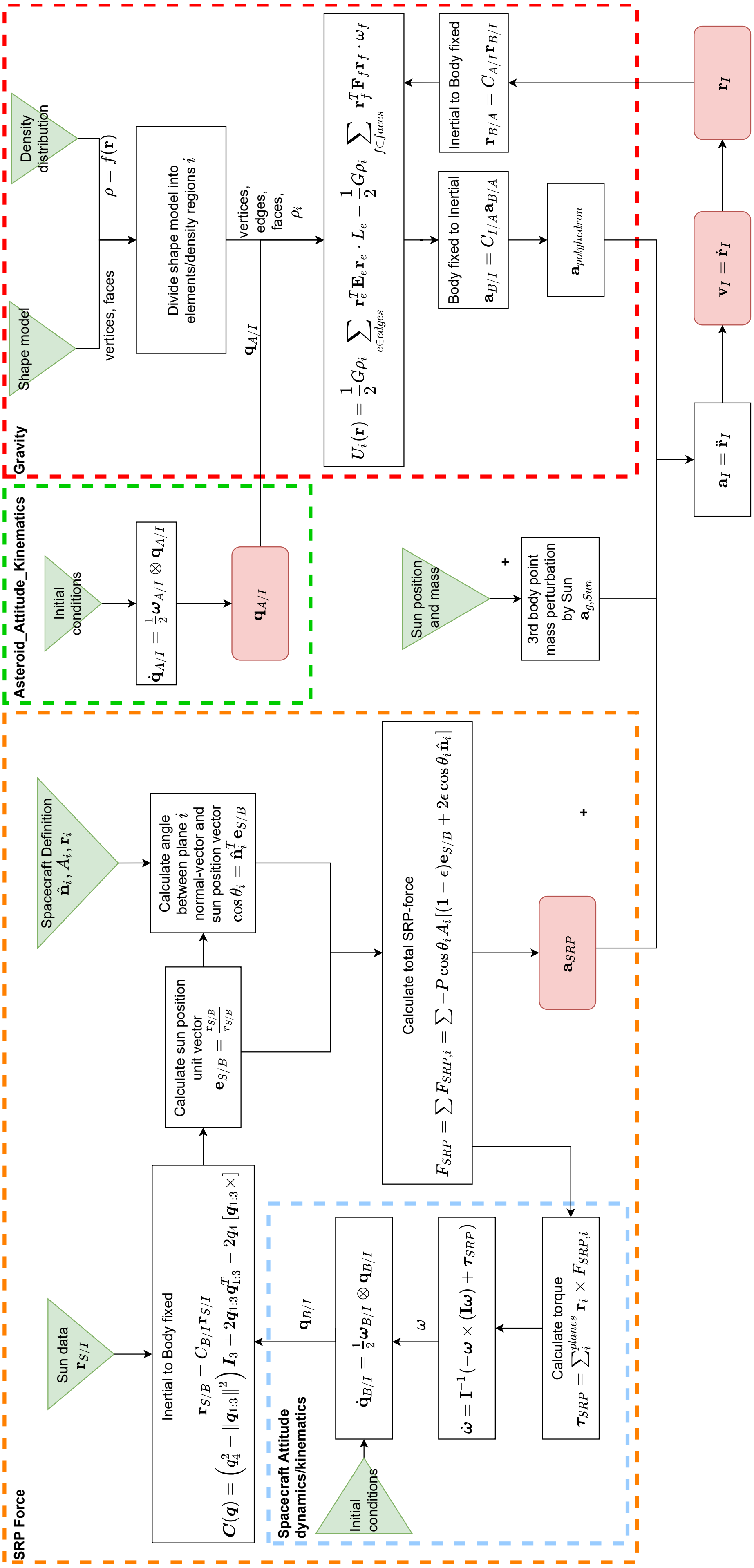

Figure 4.2: Real-world simulator structure

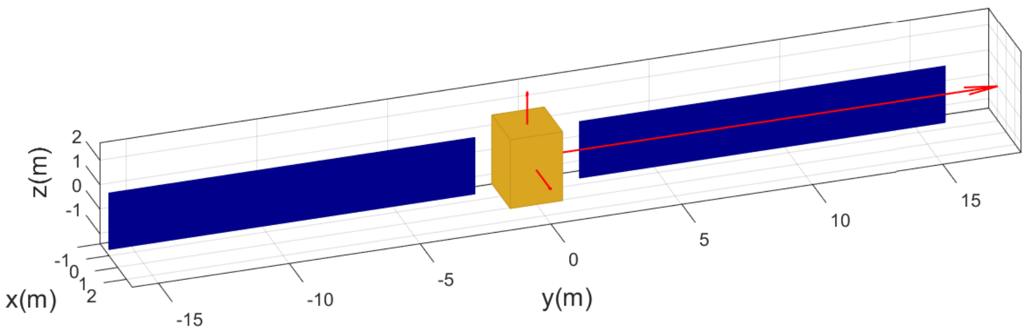

Figure 4.3: Spacecraft model used for simulation visualized in the Body-fixed reference frame. The yellow/brown box indicates the spacecraft's body, and the blue planes indicate the solar panels.

with:

$$\mathbf{I}_b = \begin{bmatrix} \frac{1}{12}M_b(l_y^2 + l_z^2) & 0 & 0 \\ 0 & \frac{1}{12}M_b(l_x^2 + l_z^2) & 0 \\ 0 & 0 & \frac{1}{12}M_b(l_x^2 + l_y^2) \end{bmatrix} \tag{4.2}$$

$$\mathbf{I}_{sp} = \begin{bmatrix} \frac{1}{12}M_s(s_y^2 + s_z^2) + M_s d_x^2 & 0 & 0 \\ 0 & \frac{1}{12}M_s s_z^2 & 0 \\ 0 & 0 & \frac{1}{12}M_s s_y^2 + M_s d_z^2 \end{bmatrix} \tag{4.3}$$

Here, l_i and s_i are the dimensions of the body and solar panels, respectively, along axis i. d_i indicates the displacement of the principal axis of rotation, which is 9 meters in the x and z direction. The resulting inertia tensor is given below:

$$\mathbf{I}_{SC} = \begin{bmatrix} 16590 & 0 & 0 \\ 0 & 2057 & 0 \\ 0 & 0 & 15964 \end{bmatrix} \text{kg m}^2 \tag{4.4}$$

The moment of inertia is important for simulating the rotational motion of the spacecraft.

- **Reflectivity**
  The reflectivity of the spacecraft starts with defining the faces of the spacecraft enclosing the mass as done in Figure 4.3. The blue colored solar panels are given a reflectivity of ϵ = 0.21, based on Montenbruck and Gill (2000). The reflectivity of the body is assumed ϵ = 0.5.

4.2.2. Asteroid model

Besides the spacecraft, also the target asteroid is defined before running the simulation. This asteroid is assumed as the real situation. The polyhedron shape models are used to represent the irregular body of the asteroid. To have a realistic defined asteroid, the density, rotational rate and shape model of Eros are used. The elongated shape of Eros motivates to use a different gravity model than spherical harmonics, as a relatively large region exterior to the asteroid is in the Brillouin sphere. Besides the shape, also the rotational rate and density shall be defined.

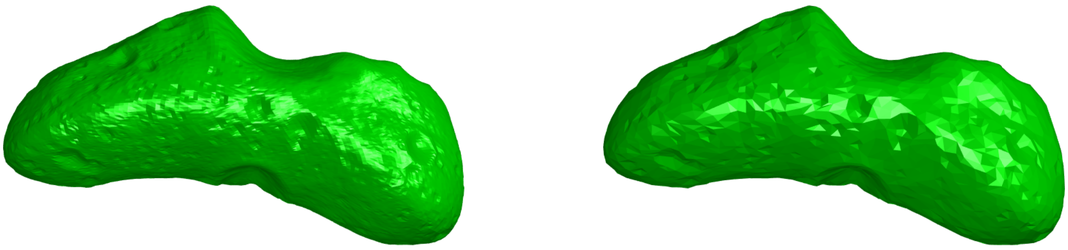

(a) Eros shape model 49152 faces (Gaskell, 2008) (b) Simplified Eros shape model 5144 faces.

Figure 4.4: Original shape model (a) from Gaskell (2008) of 433 Eros, and it's simplified model used for simulation.

4.2.3. Shape model

The shape model of Eros is visualized in Figure 4.4a. This shape model consisting of 49152 faces is simplified to 5144 faces. This simplification is done with the software package called *MeshLab*[2]. The resulting shape model is visualized in Figure 4.4b. Comparing the two shape models shows the loss of detail, but overall shape preserves. The volume of the simplified shape model is only 0.02% smaller than the Gaskell 50k shape model.

With the existing software package *gmsh*[3] the shape model of the target asteroid is divided into elements. The algorithm which divides the shape model is based on Delauney triangulation. The model is simplified, because the size of the surface triangles determines the precision of the volume shape model. The simplified shape model still results in mass elements with a maximum size of less than 1 km^3. In Figure 4.5 the obtained 3D volume shape model is visualized. The figure shows that the volume shape model is completely filled with connected tetrahedra. These tetrahedra can be distinguished as asteroid mass elements. For each element in the mesh, all faces and edges are defined, such that calculations can be done over every single element.

4.2.4. Density distribution

As the polyhedron is divided into distinguishable elements, a density distribution can be assigned to the asteroid. The resolution of this density distribution depends on the size of the elements. In order to quantify the density distribution on characterizing parameters, the Mátern covariance function is used. The Matérn covariance function is given by(Bachoc, 2013):

$$\mathbf{M}(r) = \frac{\sigma^2}{\Gamma(\nu)2^{\nu-1}}\left(\frac{2\sqrt{\nu}}{l}r\right)^{\nu}\mathcal{K}\nu\left(\frac{2\sqrt{\nu}}{l}r\right), \tag{4.5}$$

where r is the distance, Γ the Gamma function, $\mathcal{K}_{nu}$ the Bessel function. The parameter σ^2 is the variance, ν the smoothness parameter, and l the scale parameter. This function can be applied on numerous problems as the Matérn covariance is dependent on the distance between points. For example, Thor (2016) used the Matérn covariance function to map the thickness of the Martian elastic lithosphere. He determined the covariance function using the difference in degrees on a sphere between mapping points.

The effect of the smoothness parameter is shown in Figure 4.6a. The graphs show that for increasing ν, the inflection point increases in distance. This means the covariance is high between points of a

---

[2] Documentation about the *MeshLab* software can be found on: meshlab.net

[3] Documentation about the *gmsh* software can be found on: gmsh.info

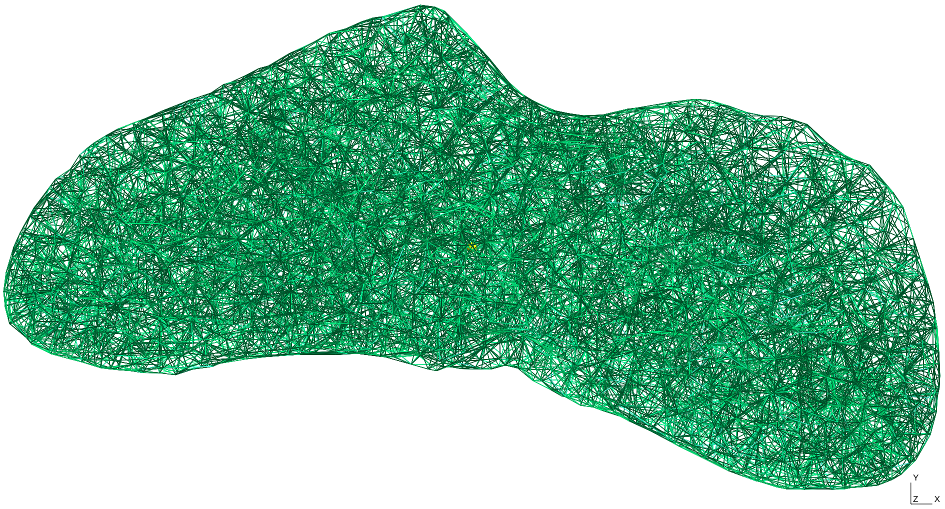

Figure 4.5: Volume shape model as visualized in *gmsh*.

certain distance compared to the resulting covariance when using a lower value of ν. The effect of the scale parameter is shown in Figure 4.6b. Here, the convergence of the covariance to zero increases with increasing l. The effect of these parameters becomes clear when it is used to generate a distribution. When considering a 1D problem with equally spaced distances between consecutive points on a line, the resulting random numbers using the covariance matrix are shown in Figures 4.7a and 4.7b. It clearly shows that for increasing ν the short-wavelength variations decrease and the curve becomes smoother. On the contrary, for increasing l, the long-wavelength variation decreases.

This covariance function is applied on the asteroid-case, using the distance between the centers of mass of the polyhedral elements. A covariance matrix is generated with the rows i and columns j referring to a single element. Matrix-element (i, j) refers to the covariance using the Euclidean distance between element numbers i and j. This covariance matrix is then used to generate a distribution of densities with an average equal to the known bulk-density of the asteroid. The rate of heterogeneity can then be varied using the explained parameters. The ranges of parameter values are based on the realism of the obtained density distributions.

4.2.5. Dynamics

Gravity

In the simulator, a gravity model is implemented to determine the gravitational acceleration on the spacecraft caused by the target asteroid. As stated before, the general method to model an irregular gravity field of celestial bodies is using spherical harmonics as most bodies of interest are spherical. Another often used option is using the polyhedron model. This method is mostly used for irregularly shaped bodies. Both models were implemented in earlier versions of the simulator. Razgus et al. (2017) implemented the polyhedron model in a real-world simulator assuming a uniform density distribution. Bourgeaux (2020) implemented the spherical harmonics model in both the real-world simulator as the navigation system to see whether this model could be used to increase the navigational performance.

Since a goal of this study is to test the dependency of the designed navigation system performance on the heterogeneity of the asteroid, the constant-density polyhedron model does not suffice. While the spherical harmonics model does include density differences, the model diverges below the Brillouin sphere. Therefore, an alternative approach is applied. As the measurements for a trajectory only have to be computed once, separately from the estimation, the computational time for the real-world simulator is not of major importance. To include density differences, the asteroid is divided into elements. The number of elements determines the resolution of the density distribution. These individual

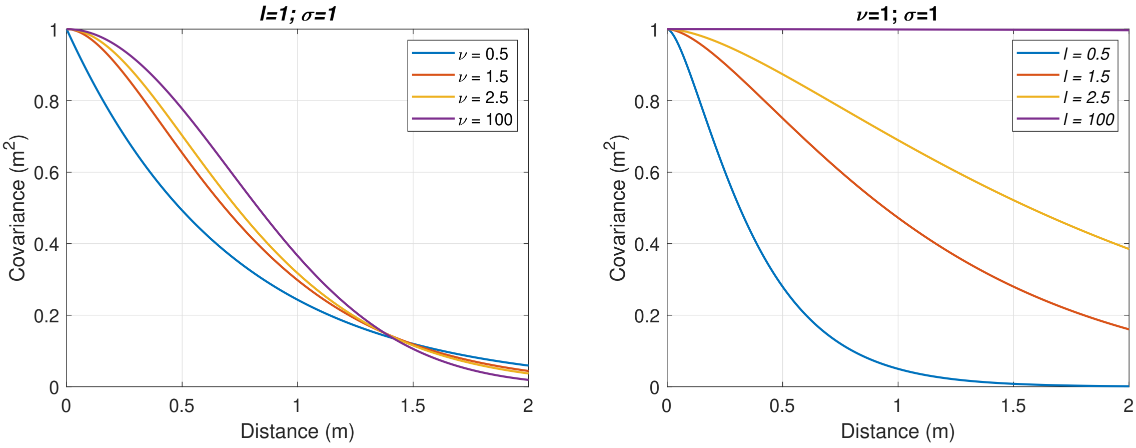

(a) (b)

Figure 4.6: Plots of Matérn covariance against the distance for different values of (a) smoothing parameter ν and (b) scaling parameter l. Reproduced from Bachoc (2013)

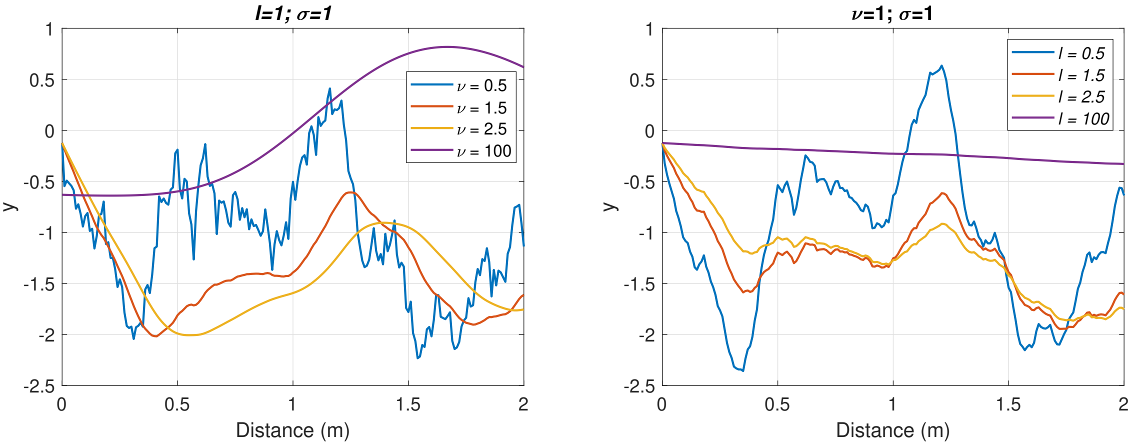

(a) (b)

Figure 4.7: Random generated numbers using the Mátern covariance over distance for different values of (a) smoothing parameter ν and (b) scaling parameter l. For reproducibility, the fixed seed 2 was used.

elements i can then be assigned a density value ρ_i. The contribution of the element on the gravitational acceleration on the spacecraft can then be calculated using the constant-density polyhedron model. Summing up the contributions of all elements according to the equation below gives the total gravitational acceleration by the heterogeneous asteroid.

$$\frac{\partial U(\mathbf{r})}{\partial \mathbf{r}} = G \sum_{i \in elements} \left\{ -\rho_i \sum_{e \in edges} \mathbf{E}_e \mathbf{r}_e \cdot L_e + \rho_i \sum_{f \in faces} \mathbf{F}_f \mathbf{r}_f \cdot \omega_f \right\} \tag{4.6}$$

Here, the symbols in this equation are the same symbols as used in Eq. (2.25).

Solar Radiation Pressure

Besides the target asteroid, also the Sun is included in the environment. The photons emitted by the Sun cause a force on the spacecraft. This solar radiation pressure can be determined using Eq. (2.27). The equation sums up the solar pressure per plane. To do this, the planes first are defined using point masses. The point masses are placed at the corners of the rectangular spacecraft. Connecting the point masses defines the planes of which the area and normal vector can be determined. This vector depends on the used reference frame and attitude of the spacecraft. Also, the angle the planes make with the Sunlight is dependent on the attitude. Therefore, it is important to also determine the spacecraft attitude during the simulation.

As the solar radiation pressure induces a force on the planes of the spacecraft, this can induce a torque. The torque can be calculated using the following equation:

$$\boldsymbol{\tau}_{SRP} = \sum_{i}^{planes} \mathbf{r}_i \times \mathbf{F}_{SRP,i} \tag{4.7}$$

This torque contributes to the change in rotational motion as described in Eq. (2.30). Integration of this change in rotation gives the rotational rate at the next time step. Using this rotational rate, the change in attitude is determined using Eq. (2.28). Integrating results in the attitude state of the spacecraft at the next time step.

Using this new attitude, the angle between the normal vectors of the spacecraft's planes and the Sunlight can again be determined. Consequently, the new $\mathbf{F}_{SRP}$ can be calculated. However, as the defined spacecraft model is axi-symmetric, this torque has negligible influence.

Third body perturbation

Besides the SRP, the Sun's gravity also has an effect on the spacecraft's trajectory. Because of the relatively short simulation time, the orbit of the asteroid around the Sun is not simulated, and the distance between asteroid and the Sun is assumed constant. Because of the large distance, the Sun is modeled as a point mass. Using Equation 2.26, this gravitational perturbation is calculated.

Asteroid Attitude Kinematics

As the asteroid rotational rate is assumed constant, only Eq. (2.33) is required to determine the attitude over time. By integrating the equation using the initial attitude, the attitude can be determined over time and be used as input to translate the spacecraft position from the inertial frame to the asteroid fixed frame.

4.2.6. Verification & Validation

Shape model verification

As the written software divides the shape model into numerous elements, the total volume of all elements should be equal to the original volume of the shape model. The volume of each polyhedron is calculated using the divergence theorem. This is done for spherical shapes with a varying volume and varying number of elements. The results are shown in Table 4.1. It shows that the maximum error

Table 4.1: Volume verification

Radius (km)	Volume sphere (m^3)	Volume error shape model (m^3)	Number of Elements (-)	Volume difference surface and volume shape (m^3)
1	4.18879e9	0.148517e9	637	9.53674e-7
10	4188.79e9	147.029e9	650	2.92969e-3
100	4.18879e15	0.148324e15	676	5
200	3.35103e16	1.17673e15	660	0
300	1.13097e17	3.89311e15	662	96
600	9.04779e17	3.14715e16	709	0
800	2.14466e18	7.45990e16	709	1536
1000	4.18879e18	1.45701e17	709	6144
10	4188.79e9	147.029e9	650	2.92969e-3
10	4188.79e9	37.4167e9	4957	1.90430e-2
10	4188.79e9	9.39608e9	39673	1.80664e-2
10	4188.79e9	2.35165e9	295576	2.44141e-3

caused by the shape division is not significant compared to the volumes. In some situations this error is zero, what implies that the error is purely caused by numerical errors in the used software. Increasing the precision of the shape model reduces the volume error in the surface shape model, but this reduction is not observed in the error by splitting the shape into volume elements. However, for verification of the splitting algorithm, the error caused by the division of the shape model into elements should be compared to the surface shape volume.

Density distribution

To verify the working of the written Mátern covariance function, the results by Bachoc (2013) and Thor (2016) have been reproduced. This verified the implementation of the function as the expected dependencies of the covariance on the parameters were obtained. Figure 4.6a is one example of a reproduced result from Bachoc (2013).

Besides the verification of the implementation of the Matérn covariance function, the application on the asteroid problem shall be validated. First, the distribution is visualized by assigning a color to every element based on their density value. The color scale then represents the density distribution. This is done for varying parameter values to see whether the distribution changes as expected. It appeared the distances should be scaled to obtain significant covariances. Having the knowledge of the relations in Figures 4.6a and 4.6b, it is chosen to scale the vertices of the shape model by dividing them by the Euclidean distance of the vertex which is furthest away from the origin. By doing this, the Matérn covariance function decreases significantly over the range of distances between the elements of target asteroid for similar parameter values as used by Bachoc (2013) and Thor (2016). By plotting the covariances over the distances for varying ν, as done in Figure 4.8, this behavior is verified. In Figure 4.9 the density distributions for varying smoothness parameter ν are shown. It clearly shows the expected relation as neighboring elements become more correlated for increasing ν. While the density distribution is still quite random for a very low value of ν, the short wavelength variation disappear for higher values of ν.

Integration equations of motion

To verify whether the simulator integration and spacecraft position propagation, a circular orbit is generated by assuming a point-mass gravity field. The point-mass is given a mass of $6.5684 \cdot 10^{15}$ kg. Since the point-mass gravity model is assumed and the mascon is positioned at the origin of the inertial frame, an circular Kepler orbit is expected when using the following initial velocity:

$$v_{circ} = \sqrt{\frac{GM}{R}} \tag{4.8}$$

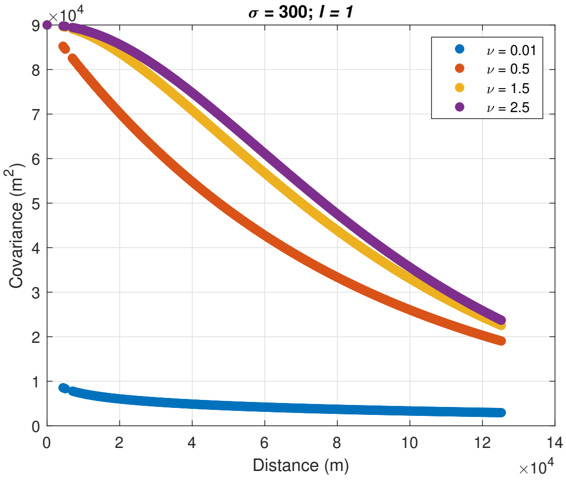

Figure 4.8: Covariance between elements plotted over their distance for varying smoothness parameter ν.

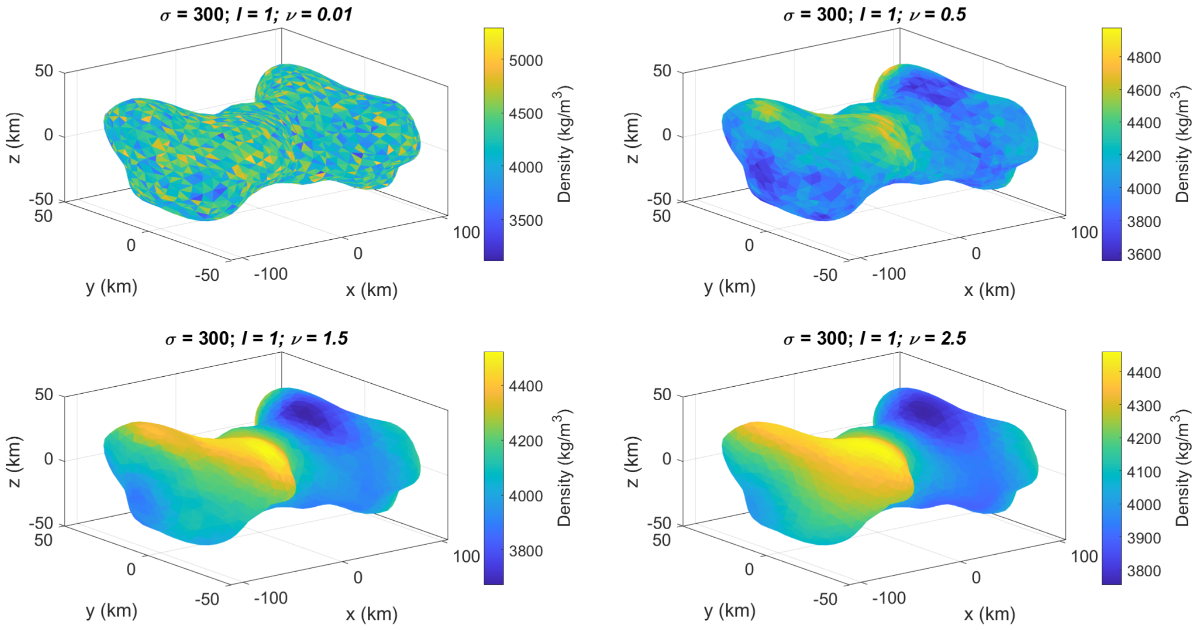

Figure 4.9: Generated density distributions for asteroid Kleopatra with varying smoothness parameter ν.

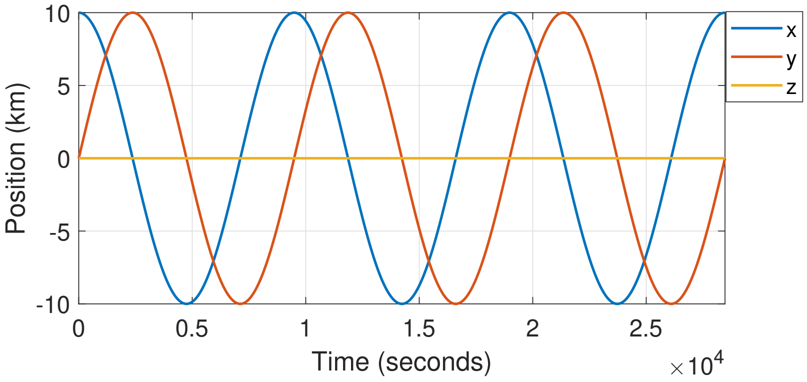

Figure 4.10: Plot of Cartesian position elements over simulation time for a circular orbit around a point-mass.

For an equatorial orbit with initial conditions $\mathbf{r}_{in} = (20\ 0\ 0)^T$ km, the initial velocity vector is $\mathbf{v}_{in} = (0\ 4.6818\ 0)^T$ m/s. The orbital period T is equal to:

$$T = 2\pi\sqrt{\frac{R^3}{GM}} \approx 9.4897 \cdot 10^3 \text{ s} \tag{4.9}$$

The resulting positions from simulation are plotted over time in Figure 4.10. This plot shows a repetitive orbit with constant properties. Since a equatorial orbit is considered, the position in the z-direction remains zero. The obtained orbital period is equal to the calculated value. Also, the radius and thus the magnitude of the acceleration remain constant. These results corresponds with a circular Kepler orbit, what verifies the translational motion simulation. Thereby, the rotational motion of the spacecraft and asteroid are tested in a torque free environment. By plotting the resulting quaternion elements of $\mathbf{q}_{A/I}$ and $\mathbf{q}_{B/I}$ against the time as a part of their set rotational period, Figure 4.11 is obtained. This figure shows the continuity in these quaternions and their repetitive behavior over two rotation periods. This is as expected according to quaternion theory, because two quaternions can indicate the same attitude (Razgus et al., 2017). The constant rotation was also observed in the obtained angular velocity vector over time. These results verify the working of the rotational motion simulation.

Gravitational acceleration

To verify the gravity field calculation using the heterogeneous polyhedron model, the resulting gravity field is compared with the existing and verified polyhedron gravity field calculation by Razgus et al. (2017). The gravity field of the Eros simplified shape model over the XY-plane is visualized in Figure 4.12. This gravity field is also generated using the 3D-shape and the summation over the mass elements, all with the same density. As these gravity fields should be identical, the difference between the two gravity fields is calculated and visualized in Figure 4.13. The value range is similar to the gravity field of Eros as given in Chanut et al. (2014). As can be seen, the errors are minimal and of the range of numerical errors. This verifies the summation of the polyhedron elements in the calculation of the gravitational acceleration.

The next step is to test whether a heterogeneous mass distribution gives the expected change in acceleration with respect to the homogeneous case. When the shape has a clear mass distribution where one side has a higher density than the other side, the direction of the acceleration shall point towards the side with the higher density with respect to the homogeneous case. This can be visualized as done in Figure 4.14, where it is shown the gravitational acceleration points towards the higher density region. This corresponds with the expected behavior. This test has been performed at multiple positions with respect to the asteroid and the result appeared to be consistent. Taking the difference between the gravity field of a homogeneous asteroid and a heterogeneous asteroid with the same total mass, the effect can be visualized of the density distribution on the gravity field of the asteroid. It is expected

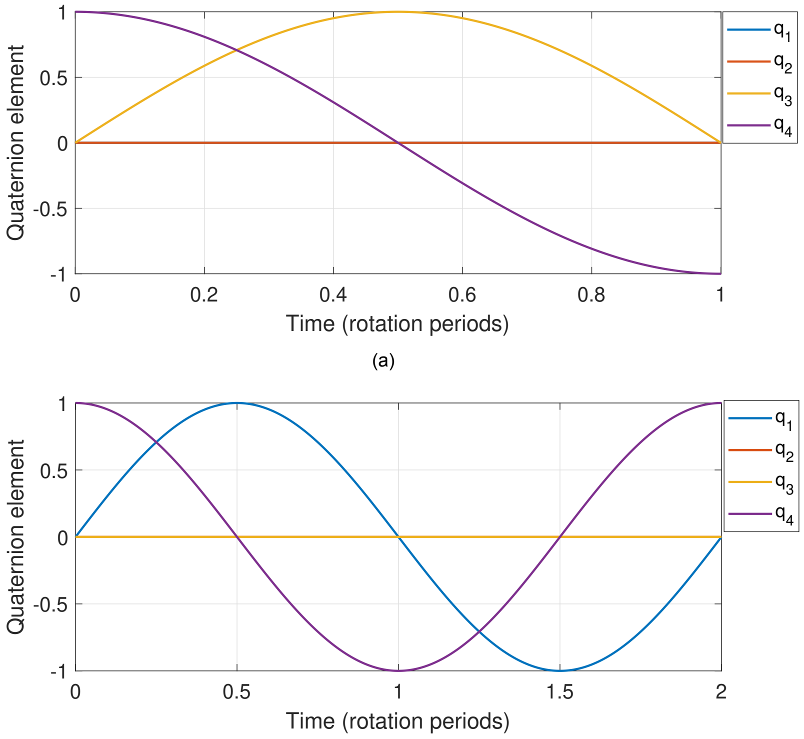

(a)

(b)

Figure 4.11: Plots of quaternion elements against the time for (a) asteroid attitude quaternion $\mathbf{q}_{A/I}$, and (b) spacecraft attitude quaternion $\mathbf{q}_{B/I}$, with respect to the inertial frame.

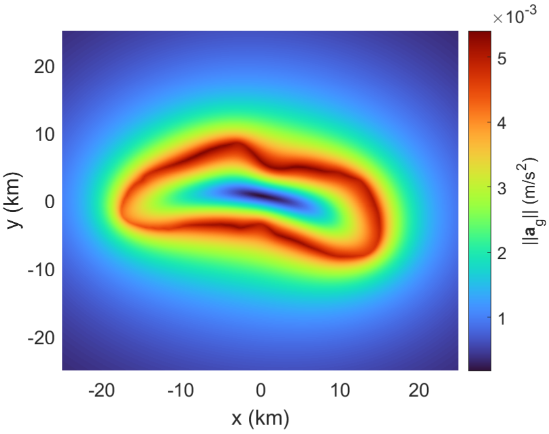

Figure 4.12: Polyhedron gravity field of 433 Eros over the XY-plane.

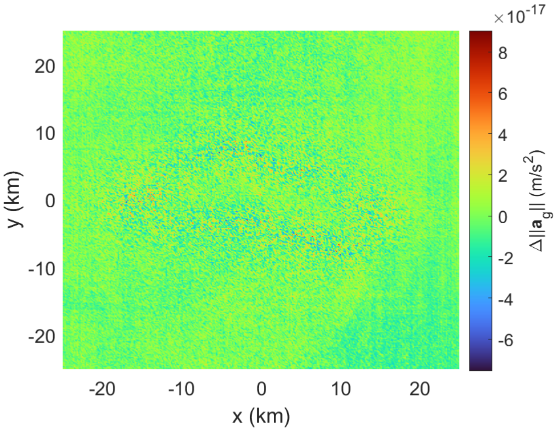

Figure 4.13: Difference between the polyhedron gravity field and the sum of the polyhedron gravity fields of each element.

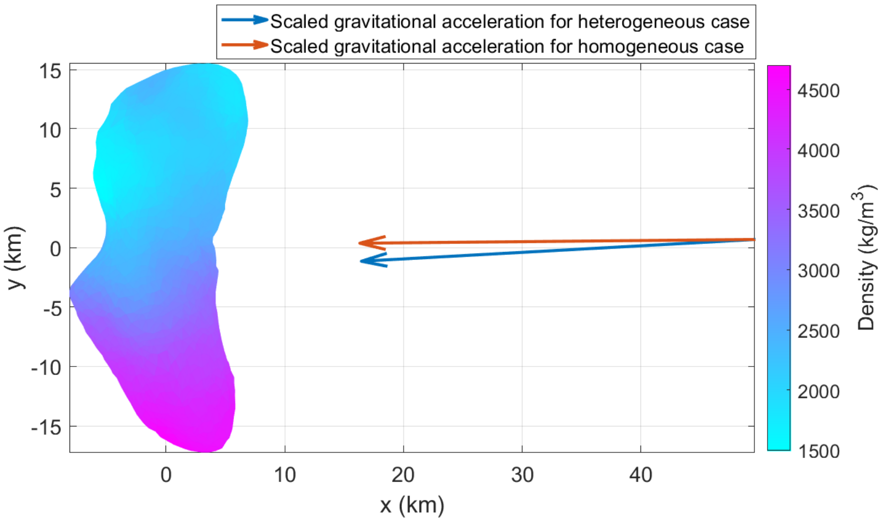

Figure 4.14: Comparison of gravitational acceleration direction between heterogeneous density distribution and homogeneous density distribution.

that the region with the higher density results in a higher gravitational acceleration with respect to the homogeneous case, and for the lower density region vice versa. In Figure 4.15, the used mass distribution is given. This distribution shows the same lateral distribution as the asteroid in Figure 4.14, but with total mass equal to the constant density model. To show the expected result is obtained, the difference between the obtained gravity field from the asteroid in Figure 4.15 and the homogeneous asteroid's gravity field has been calculated and visualized in Figure 4.16. This figure clearly shows the expected result, as the side with a higher density results into a higher gravitational attraction.

4.3. Navigation filter

As mentioned before, the EKF is considered as the better option for state estimation compared to the computationally more expensive UKF. To elaborate on this algorithm for the spacecraft situation, first a state has to be defined. The augmented state for the mascon model is written as:

$$\mathbf{x} = \begin{pmatrix} \mathbf{r} \\ \mathbf{v} \\ \mu_1 \\ \mu_2 \\ \vdots \\ \mu_N \end{pmatrix} \tag{4.10}$$

This state consists of the position, velocity, and N number of gravitational parameters of all point-masses. For state propagation the Euler step method is used. The nominal state thus gets propagated as follows:

$$\mathbf{x}_{k+1} = \mathbf{x}_k + \frac{\partial \mathbf{x}}{\partial t}\Delta t = \mathbf{x}_k + \dot{\mathbf{x}}\Delta t = \mathbf{x}_k + \mathbf{g}(\mathbf{x})\Delta t \tag{4.11}$$

Here, the time derivative of the state is defined as:

$$\dot{\mathbf{x}} = \mathbf{g}(\mathbf{x}) = \begin{pmatrix} \mathbf{v} \\ \mathbf{a} \\ 0 \\ 0 \\ \vdots \\ 0 \end{pmatrix} \tag{4.12}$$

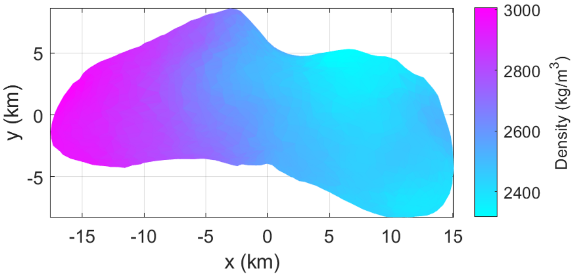

Figure 4.15: Visualization of heterogeneous asteroid.

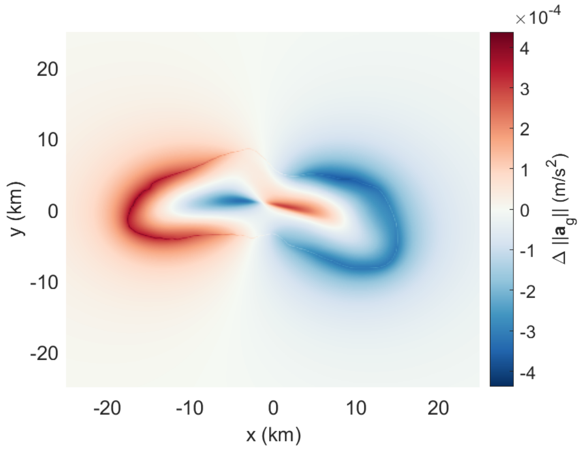

Figure 4.16: Surface plot over the XY-plane at Z=0 of differences in gravitational attraction between the homogeneous polyhedron gravity field and the heterogeneous polyhedron gravity field.

The equations of motion are used to determine the acceleration on the spacecraft. Using the mascon model, the accelerations on the spacecraft are defined as:

$$\mathbf{a}_{total} = \ddot{\mathbf{r}} = \mathbf{a}_{g,mascon} + \mathbf{a}_{SRP} + \mathbf{a}_{g,Sun}, \tag{4.13}$$

where gravitational acceleration by the mascons is defined as:

$$\mathbf{a}_{g,mascon} = \sum_{i=1}^{N} \frac{\mu_i}{|\mathbf{r} - \mathbf{r}_i|^3} (\mathbf{r} - \mathbf{r}_i) \tag{4.14}$$

The symbol μ_i indicates the gravitational parameter of the i^{th} mascon from a total of N mascons, and $\mathbf{r}_i$ indicates the position vector of the i^{th} mascon with respect to the inertial frame.

4.3.1. Measurements

As measurements, the position of the spacecraft over time with an added Gaussian noise is used, because the focus of this study is not to simulate the sensors. This is an assumption made in order to analyze the filter's dependence on the heterogeneity and used gravity model. The simulation itself would be made more realistic, if the sensors also would be simulated. However, since no control system is simulated, the orbit and thus measurements would be the same for every estimation filter. As, the focus of this study is to analyze the dependence of the performance of the navigation system on the used gravity model and its configuration and not the dependency on the accuracy of the measurements, the assumption is made. The noisy position-measurement can be written as:

$$\mathbf{z} = \mathbf{r} + \boldsymbol{v}_r \tag{4.15}$$

Here, the Gaussian noise $\boldsymbol{v}_r$ is added to the position $\mathbf{r}$. The simulation of the sensors is given as a recommendation for further research.

4.3.2. Extended Kalman Filter

The general algorithm of the EKF is explained in section 3.2 and visualized in Figure 4.17. As the state is propagated according to Eq. (4.11), the non-linear system as in Eq. (3.3) is described by this equation. The state transition matrix (Eq. (3.15)) then becomes:

$$\mathbf{\Phi} = \frac{\partial \mathbf{f}}{\partial \mathbf{x}} = \mathbf{I} + \frac{\partial \dot{\mathbf{x}}}{\partial \mathbf{x}} \Delta t = \mathbf{I} + \frac{\partial \mathbf{g}(\mathbf{x})}{\partial \mathbf{x}} \Delta t = \mathbf{I} + \mathbf{G} \Delta t \tag{4.16}$$

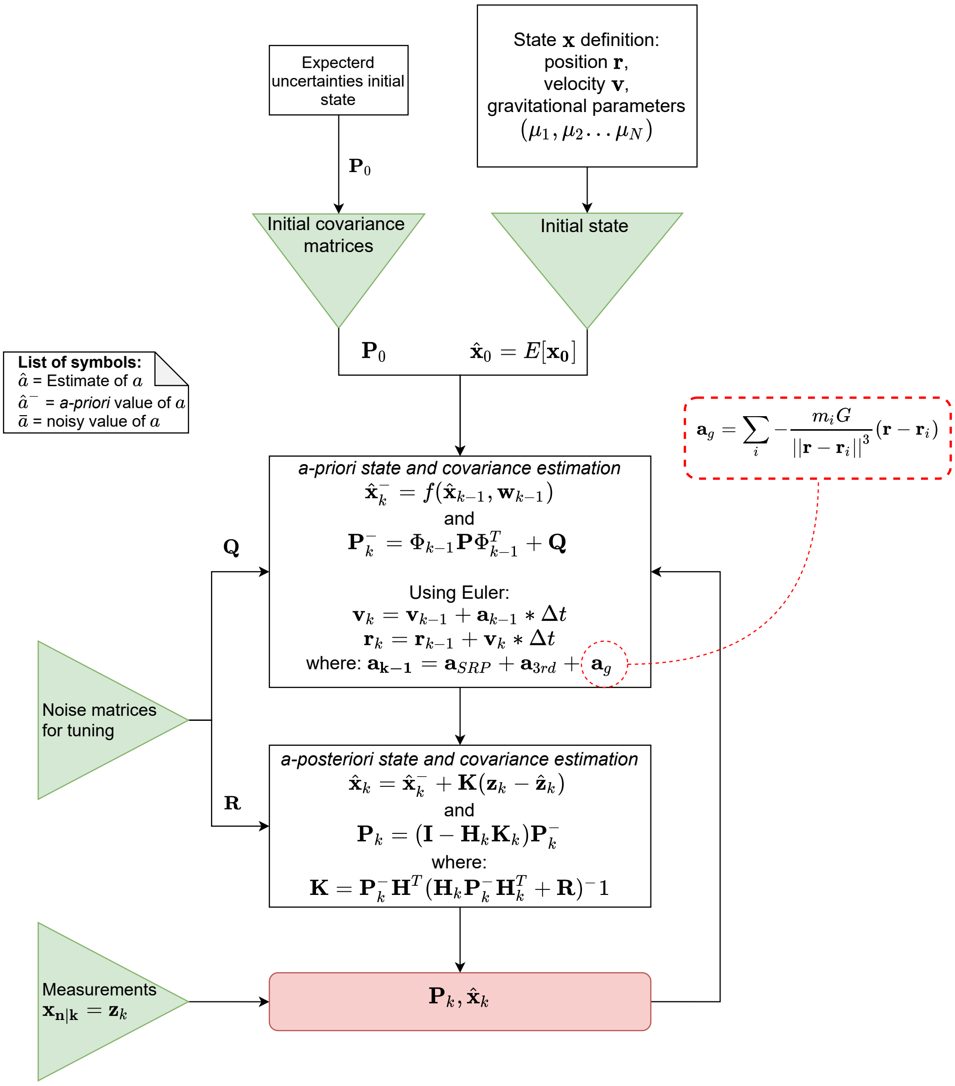

Figure 4.17: Navigation software structure

Here, knowing Eq. (4.13) and Eq. (4.12), the Jacobian matrix $\mathbf{G}$ is equal to:

$$\mathbf{G} = \frac{\partial \mathbf{g}(\mathbf{x})}{\partial \mathbf{x}} = \begin{bmatrix} 0 & 0 & 0 & 1 & 0 & 0 & 0 & \dots & 0 \\ 0 & 0 & 0 & 0 & 1 & 0 & 0 & \dots & 0 \\ 0 & 0 & 0 & 0 & 0 & 1 & 0 & \dots & 0 \\ \frac{\partial a_x}{\partial x} & \frac{\partial a_x}{\partial y} & \frac{\partial a_x}{\partial z} & 0 & 0 & 0 & \frac{\partial a_x}{\partial \mu_1} & \dots & \frac{\partial a_x}{\partial \mu_{(N-6)}} \\ \frac{\partial a_y}{\partial x} & \frac{\partial a_y}{\partial y} & \frac{\partial a_y}{\partial z} & 0 & 0 & 0 & \frac{\partial a_y}{\partial \mu_1} & \dots & \frac{\partial a_y}{\partial \mu_{(N-6)}} \\ \frac{\partial a_z}{\partial x} & \frac{\partial a_z}{\partial y} & \frac{\partial a_z}{\partial z} & 0 & 0 & 0 & \frac{\partial a_z}{\partial \mu_1} & \dots & \frac{\partial a_z}{\partial \mu_{(N-6)}} \\ 0 & 0 & 0 & 0 & 0 & 0 & 0 & \dots & 0 \\ \vdots & \vdots & \vdots & \vdots & \vdots & \vdots & \vdots & \ddots & \vdots \\ 0 & 0 & 0 & 0 & 0 & 0 & 0 & \dots & 0 \end{bmatrix}_{[N\times N]} \tag{4.17}$$

The complete derivatives of this matrix are given in Appendix A.

As explained before, the measurements are assumed to be the Cartesian position of the spacecraft with an added white noise. Therefore the gradient matrix $\mathbf{H}$ from Eq. (3.16) is defined as:

$$\mathbf{H} = \begin{bmatrix} \mathbf{I}_{3\times3} & \mathbf{0}_{3\times(N-6)} \end{bmatrix} \tag{4.18}$$

Knowing these matrices, the gain and covariance matrix can be determined using Eqs. (3.26) and (3.25), respectively. The measurement update can be done applying Eq. (3.24) and Eq. (3.27). As the measurement noise is known, following the example by Musoff and Zarchan (2009), the measurement noise matrix will be defined as the diagonal matrix:

$$\mathbf{R} = \begin{bmatrix} \boldsymbol{v}_r^2 & 0 & 0 \\ 0 & \boldsymbol{v}_r^2 & 0 \\ 0 & 0 & \boldsymbol{v}_r^2 \end{bmatrix} \tag{4.19}$$

The initial covariance matrix $\mathbf{P}_0$ can be based on the uncertainty in the initial guess. Since it includes a simulation of which the intial values are known, the initial state deviation is used to initialize this initial covariance matrix. As it appeared to be a consistent method, the covariance matrix is initialized as a diagonal matrix with the squared state deviations in the diagonal elements. By these choices, the tuning process is limited especially to adjusting the process covariance matrix $\mathbf{Q}$. The values in this matrix are tweaked by trial and error. The resulting values are given in Appendix A.

Equality constraint

During the simulations, there is applied an equality constraint once to see whether the results improves when fixing the total mass of the asteroid in the EKF. Such equality constraint can be applied easily by using the algorithm as described in Simon (2010) and Ungarala et al. (2007). An equality constraint is written as:

$$\mathbf{D}\mathbf{x} = \mathbf{d} \tag{4.20}$$

, where $\mathbf{d}$ is a known vector and $\mathbf{D}$ is a known matrix. The constrained *a-posteriori* state estimation is then given by:

$$\hat{\mathbf{x}}_{k,constr} = \hat{\mathbf{x}}_k - \mathbf{P}_k\mathbf{D}^T(\mathbf{D}\mathbf{P}_k\mathbf{D}^T)^{-1}(\mathbf{D}\hat{\mathbf{x}}_k - \mathbf{d}) \tag{4.21}$$

The constraint also has consequences for the covariance matrix, as this matrix is constrained according to the following equation:

$$\mathbf{P}_{k,constr} = \left(\mathbf{I}_{N\times N} - \mathbf{P}_k\mathbf{D}^T(\mathbf{D}\mathbf{P}_k\mathbf{D}^T)^{-1}\right)\mathbf{P}_k \tag{4.22}$$

Here, N is length of augmented state $\mathbf{x}$.

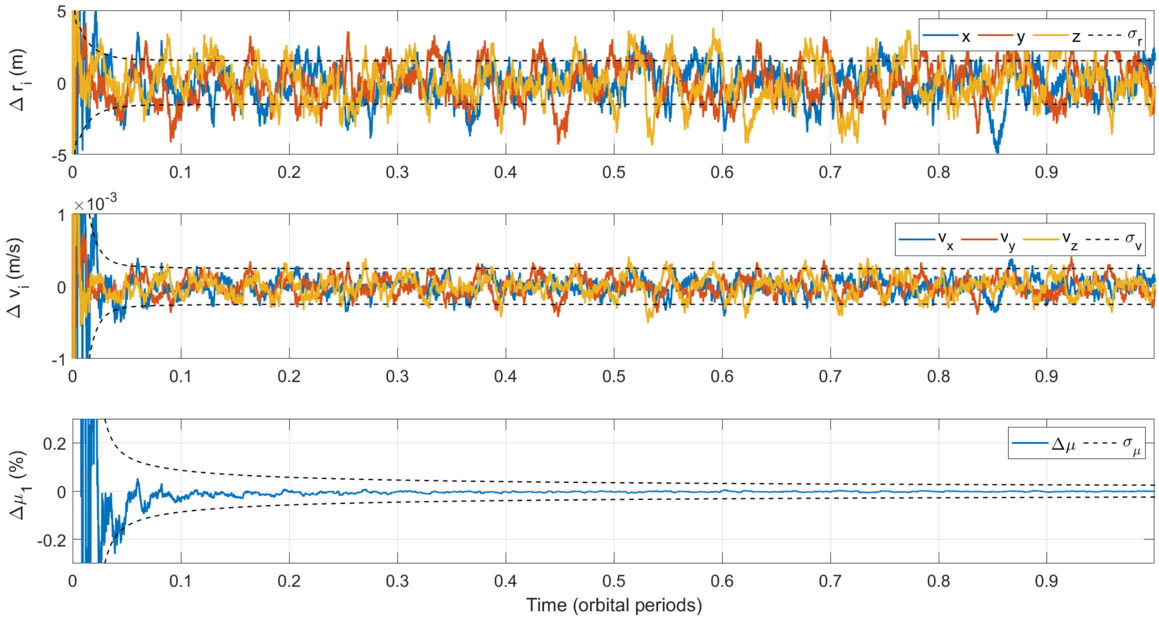

Figure 4.18: Estimation errors using one point-mass.

4.3.3. EKF verification & validation

The Kalman filter, with the mascon gravity field model implemented, is tested using a real-world which also uses the mascon gravity model, such that the estimated gravity field can directly be compared with the defined real world. For this test, the polyhedron model as described in section 4.2 is replaced by the same gravity field model as used in the navigation system, as described in section 4.3. If the state estimating EKF works as expected, the state-variables converge to the values defined in the real-world simulator.

The first test is estimating a single point-mass. For this case, the initial conditions for a circular orbit at with a radius of 200 kilometers are used as input for the real-world simulator. The resulting orbit is close to a Kepler orbit, because it only uses one point-mass for the gravity of the main body. It is no exact Kepler orbit as the third body perturbation and SRP are included in the dynamical environment. This orbit is given a noise with a standard deviation of 100 meter before using it as measurements. Using these measurements, the value for the gravitational parameter is estimated accurately as expected. The resulting errors are shown in Figure 4.18.

Next, the system is tested using more than one point-mass. Placing two point masses of both half the mass of Eros at the positions $(x\ y\ z) = (\pm 5,\ 0,\ 0)$ km gives the following results for a close to circular orbit at 200 kilometers with an inclination of 90 degrees. As shown in Figure 4.19, the error in the estimation of the gravitational parameters μ_1 and μ_2 is increased significantly compared for the one point-mass. However, looking at the sum of these parameters in the upper plot, one can see the total mass was estimated very accurately. This suggests that the lower-order term attraction, the total mass, is the dominant force and the spacecraft is experiencing the higher order terms relatively little.

However, this effect is observed with the set position measurement standard deviation of 100 meters. This seen effect should decrease when increasing the measurement accuracy from a standard deviation of 100 meters to a lower standard deviation of 1 meter. This effect is clearly seen in Figure 4.20. With this measurement accuracy, the influence on the trajectory of the higher order terms is also seen quite accurate.

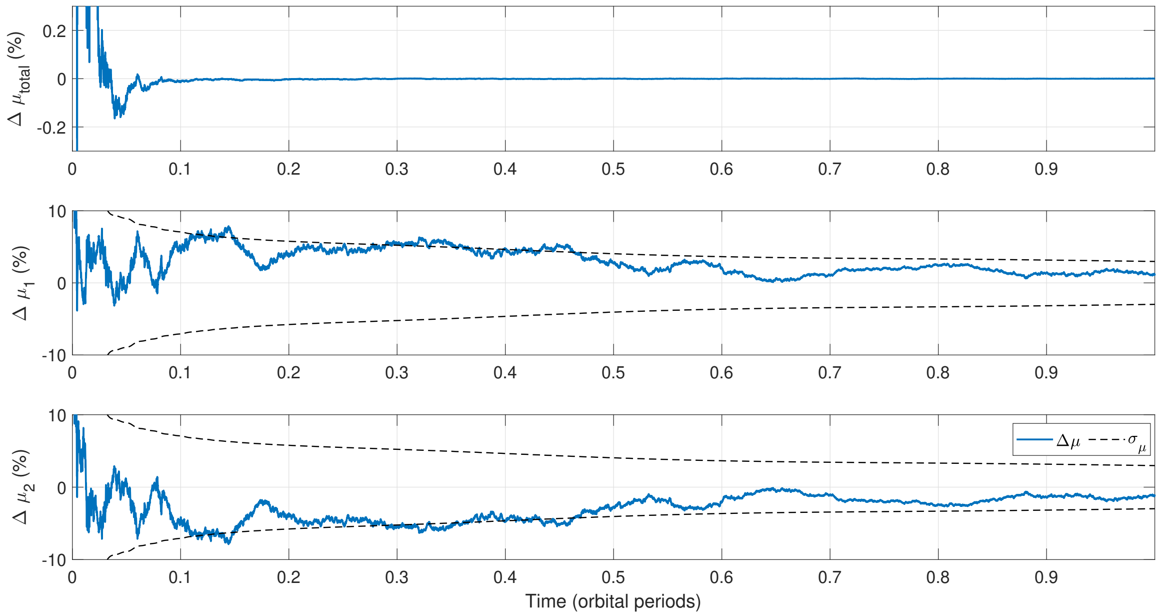

Figure 4.19: Estimation accuracies of the gravitational parameters and the error in the sum of these parameters, using position measurement with an accuracy of 1 meter. Applied for a circular polar orbit at 200 kilometers around 2 point masses placed on x-axis

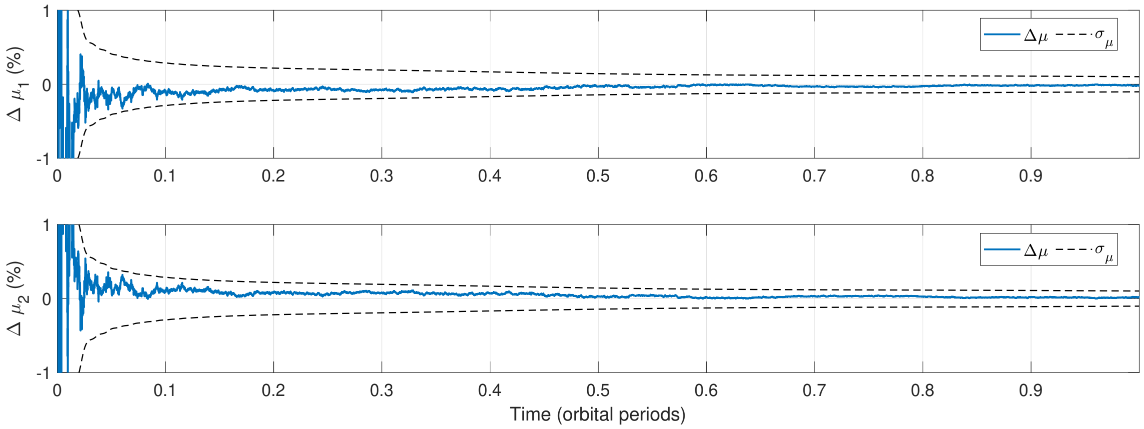

Figure 4.20: Estimation accuracies of the gravitational parameters, using position measurement with an accuracy of 1 meter. Applied for a circular polar orbit at 200 kilometers around 2 point masses placed on x-axis

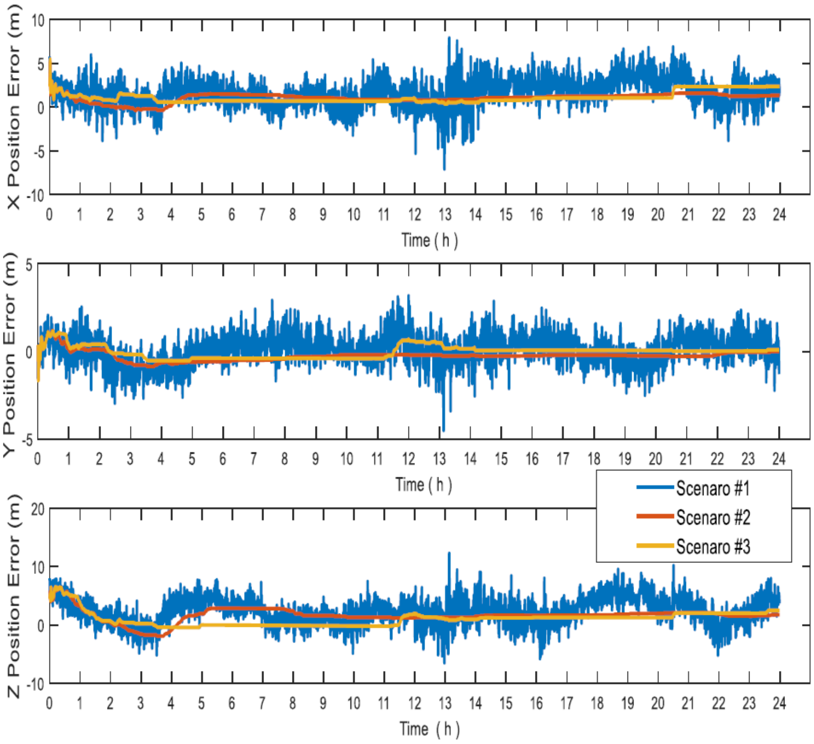

Figure 4.21: Plot of GNSS position accuracy over time from Ngoc et al. (2019), where scenario #1 has a relatively high **Q** and scenarios #2 and #3 have **Q** set close to its true values.

Tuning

As for example done in Musoff and Zarchan (2009), the behavior of the filter with respect to its tuning parameters is tested by observing the differences in the estimation accuracy for varying tuning parameter values. To validate the behavior of the filter, it is compared to tests done by Musoff and Zarchan (2009) and Ngoc et al. (2019).

Since **Q** is defined as the process noise covariance matrix, it refers to the uncertainty in the dynamical model. The higher the values in this matrix, the less confidence the system has in its dynamical model. The lower these values, the higher the confidence of the system in the dynamical model. The first case is clearly shown in the study by Ngoc et al. (2019). Figure 4.21 shows the obtained GNSS position accuracy over time for different tuning scenarios. Only scenario #1 has a high **Q**, where the other have **Q** set close to the correct values. The figure shows clearly a worse estimation for scenario #1, which is not stable and less smooth. This makes sense as there is put more weight on the measurements, which contain a certain noise. The opposite is shown in a test performed by Musoff and Zarchan (2009) where the process noise covariance matrix is set equal to a zero matrix. After 20 seconds the estimation clearly diverges as the error increases rapidly. This is explained as the filter ignoring new measurements after a certain time, because of a maximal confidence in its dynamical model.

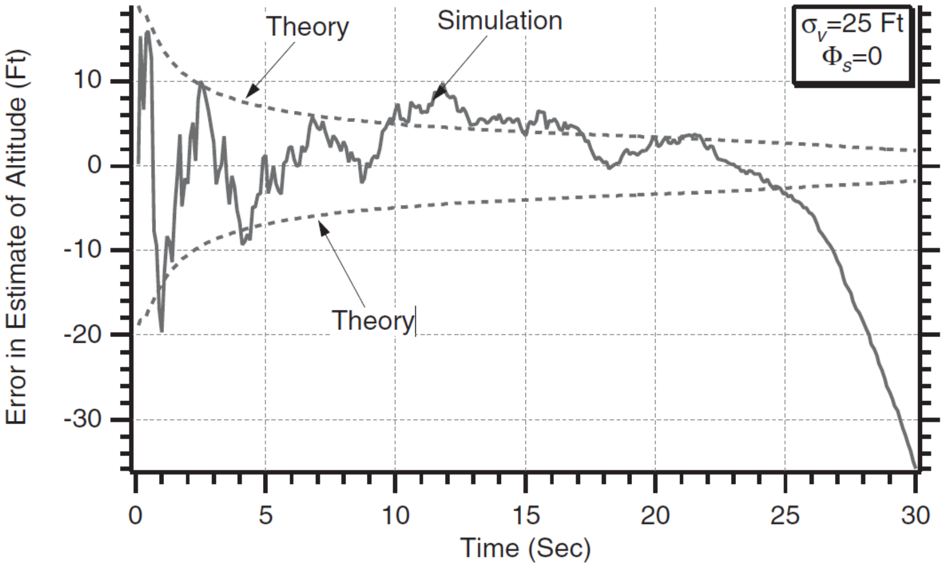

Figure 4.22: Plot of diverging altitude estimate of a falling object as performed by Musoff and Zarchan (2009), using the EKF with zero process noise (Φ_s) and noisy measurements (standard deviation σ_v).

To validate the designed EKF its behavior with respect to the tuning, it is tested whether the EKF shows similar behavior for very high and very low values for the process noise covariance matrix $\mathbf{Q}$. To be able to directly compare the estimated gravitational parameters, again a mascon model real world is defined with positions equal to the defined mascon model in the EKF. Using 3 point-masses, μ_1 positioned at $(5,\ 0,\ 0)^T$, μ_2 at $(0,\ 0,\ 0)^T$ and μ_3 at $(-5,\ 0,\ 0)^T$ km, a 100 meter measurement noise and initial deviations of 10 meter and 1 m/s in each direction, and 30% of the μ-values, the resulting errors for a 60 degrees inclined 50 km radius circular orbit for $\mathbf{Q} = \mathbf{I}$ and $\mathbf{Q} = \mathbf{0}$ are shown in Figure 4.23. These figures clearly show the expected results based on the mentioned examples. For a high process noise, Figure 4.23a shows the noise is dominant in the resulting accuracy. This is the result as expected, because the measurements are assumed to only have Gaussian noise with a standard deviation of 100 meters in each direction and, for example, has no bias or scaling errors. For zero process noise, Figure 4.23b also shows the expected result. Because the filter ignores the measurements after a certain time, the remaining errors are propagated and the estimation diverges from the real state. This behavior is similar compared to the results shown in Figures 4.21 and 4.22.

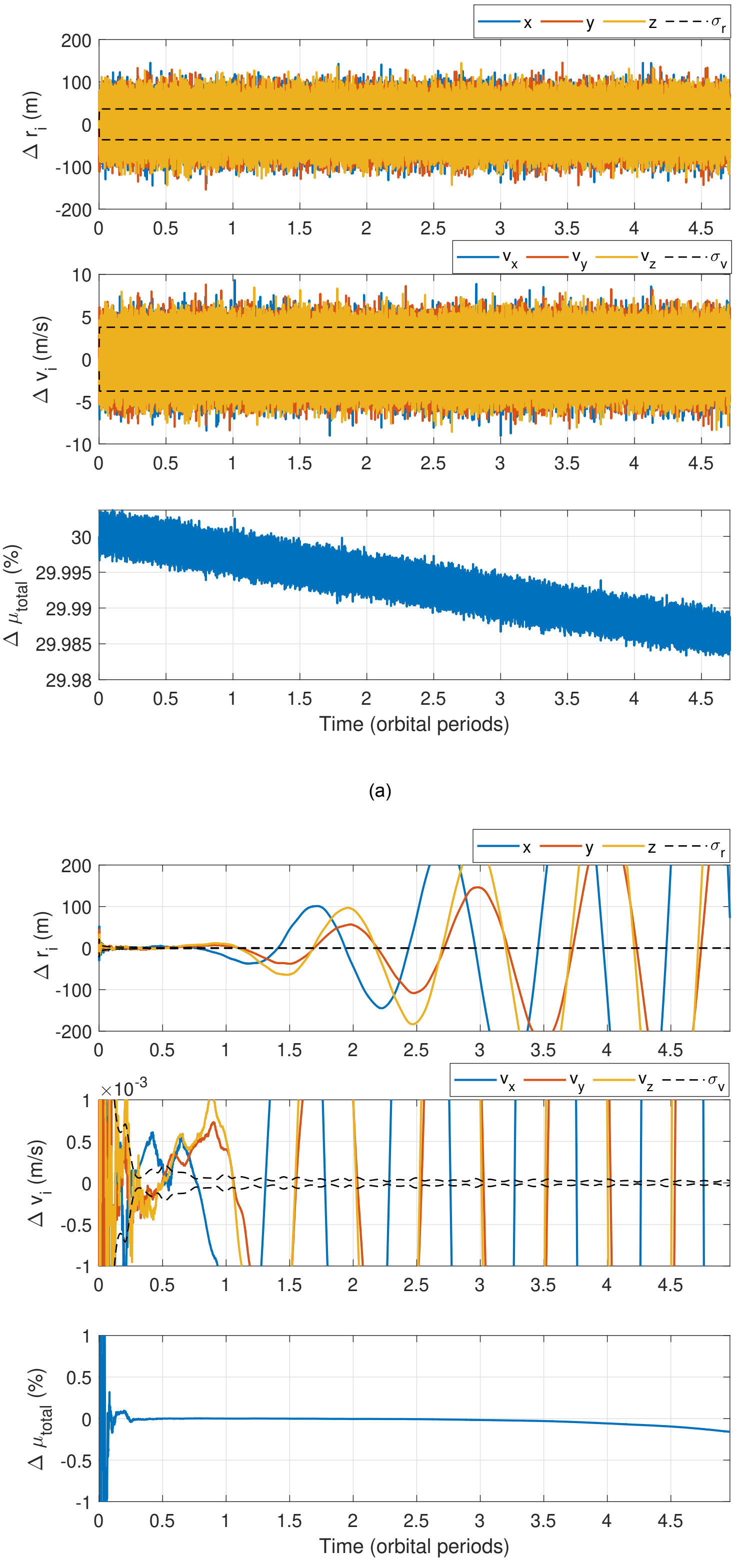

(a)

(b)

Figure 4.23: Plot of the position, velocity, and total μ error over time using (a) $\mathbf{Q} = \mathbf{I}$, and (b) $\mathbf{Q} = \mathbf{0}$.

5

Results

In this chapter, the results of the analysis are given. First, some insight in the tuning process is given in section 5.1. Next, the dependencies of the EKF performance on model parameters and orbit characteristics are analyzed in section 5.2. During this sensitivity analysis, the point mass model is applied in the simulator for reference. After this, in section 5.3 the performance of the EKF in a polyhedron real world is assessed for multiple mission phases. Here, a stepwise approach is applied to increase the model accuracy and estimation performance. Along this stepwise approach, relevant observed dependencies are highlighted. Multiple mascon models are tested in this section. In section 5.4, it is investigated whether the EKF performance depends on the level of heterogeneity in the asteroid's mass distribution. Also, it is tried to derive the density distribution from the estimated mass distribution. Finally, the model performance is assessed by comparing it with the performance of the spherical harmonics model in Bourgeaux (2020), and testing the system inside the Brillouin sphere.

5.1. Tuning

As the EKF has to be tuned properly, each scenario and filter setting is assessed based on the acquired accuracy and stability of the estimation. As measurement noise matrix $\mathbf{R}$ is defined using the set measurement accuracy (Eq. (4.19)), and the initial covariance matrix $\mathbf{P}_0$ diagonal elements is initialized according to the set initial estimation error, the tuning proces during this thesis is focused on manually tweaking the process noise matrix $\mathbf{Q}$. During the filter tuning process it is tried to minimize the set values for matrix $\mathbf{Q}$, such that the estimated position and velocity reach a converged solution toward a stable orbit, of which is at least about 68% of the state error inside the estimated 1σ error obtained from the *a-posteriori* covariance matrices. This process minimized the resulting position and velocity error while the *a-posteriori* variances give a correct approximation of the uncertainties in the estimation. The state error can be calculated for position and velocity as the real values are known. However, as the real world simulator uses a different gravity model than the EKF, the estimated gravitational parameters cannot be directly compared to the real-world. Therefore, the diagonal elements in the initial covariance matrix for the gravitational parameters are based on possible density ranges of a certain asteroid-type. More details on tuning the EKF are given in Appendix A.

5.2. Mascon model sensitivity

The EKF its basic dependencies are investigated simulating the spacecraft orbiting the mascon model with equal mascon positions as the defined mascon model in the EKF. By doing this, the resulting gravitational parameter estimations can directly be compared to the real-world values.

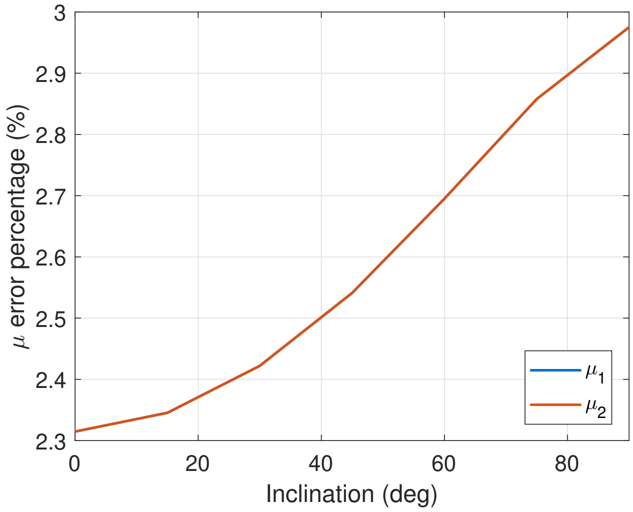

Figure 5.1: Resulting deviation from a-posteriori variances as a percentage of the parameter value plotted against orbit inclination. Done for 200 km circular orbit.

5.2.1. Estimation point mass gravity-field

As shown already during the verification of the EKF, with a higher deviation in the measurements, the system estimates the higher-order terms less accurately. To investigate how the resulting accuracy depends on the orbit characteristics, the orbit is altered. First, the inclination is changed. As the attraction is dependent on the distance between the spacecraft and the point-masses (Eq. (2.17)), a lower inclination would increase the change in relative distance between the spacecraft and the equatorial aligned point-masses. Comparing the resulting variances after estimation during one orbital revolution, Figure 5.1 is acquired. This figure clearly shows the expected increasing accuracy with decreasing inclination. The variances of the gravitational parameters are almost identical. As the gravity field of the two identical point masses is symmetric with respect to the YZ-plane, and the orbit is close to circular, this similarity in resulting variances is not unexpected. Defining a mass-difference between the two point-masses results in a higher estimation accuracy for the heavier point-mass, as the spacecraft is attracted more by this mascon. The incremental relation as in Figure 5.1 is still observed. Also, the relation is observed for circular orbits with a lower radius. The found relation between the inclination and the accuracy arguments for a well-thought orbit-design depending on the defined relative position between the point-masses.

Orbits relatively close to the surface result in higher accuracies for the gravitational parameters compared to orbits further away from the surface. This can be explained by a greater influence of an error in the gravitational model on the deviation of the expected acceleration with the felt acceleration, as the gravitational acceleration is larger when close to the surface relative to when at a large altitude. In Figure 5.2a, a surface plot is shown, which shows the relations between the resulting error in the estimated μ values, inclination and orbit radius. The figure clearly shows the decreasing error with decreasing altitude and inclination. However, when increasing the number of point-masses, the relation between accuracy and orbit inclination changes significantly. As shown in Figure 5.2b, the average error increases for decreasing inclination at most altitudes. This inverse of the relation found for a two point-mass model is caused by the addition of the extra point-mass in the middle. For an equatorial orbit, where the orbit plane is parallel to plane of the mascons' movement, such middle mascon is almost the complete time further away from the spacecraft than one of the outer point-masses and for a large part of the time hidden behind the other mascons from spacecraft perspective. Therefore, the estimation results in high uncertainties. At higher inclinations, the time in which the acceleration is dominated by one of the outer mascons and the time it is behind another mascon is decreased. Therefore, the estimation uncertainties of these mascons also decrease, what explains the observed relationship for

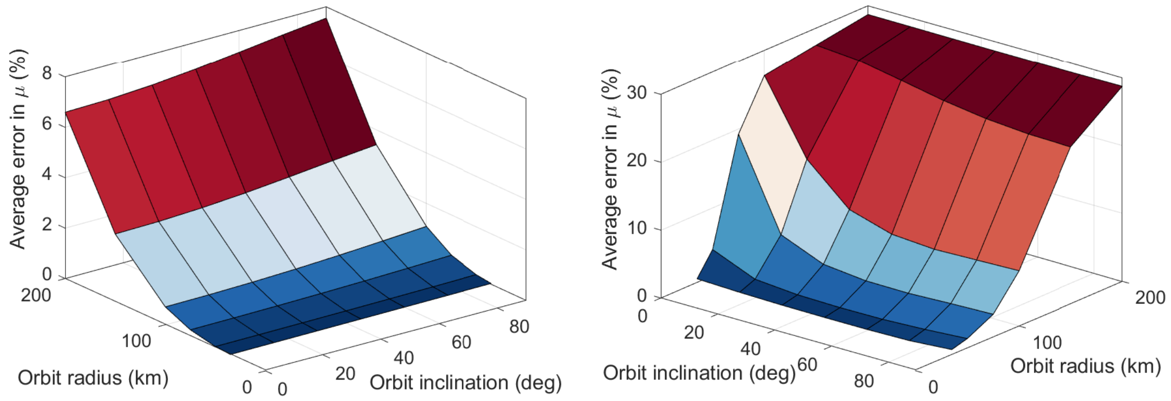

(a) (b)

Figure 5.2: Plot of the average error in the gravitational parameters against the orbit radius and inclination for (a) a two point-mass model and (b) a three point-mass model.

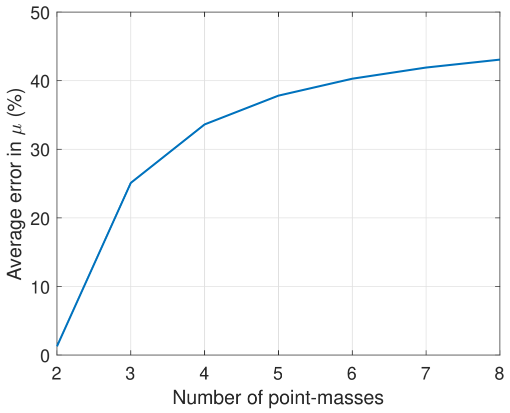

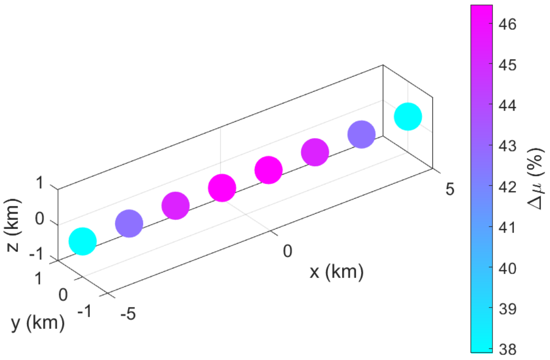

Figure 5.3: Error in estimated μ averaged over the number of point-masses, plotted over the number of point-masses.

Figure 5.4: Distribution of the estimation error over the eight point-masses.

more than two point masses. Also, the error increases when adding more point masses along the x-axis. This is shown by plotting the resulting error against the number of point-masses. Here, the total mass of the mascon model is kept constant and the mass of each mascon is equal. For example, for a circular orbit at an altitude of 100 kilometers, plotting the error in estimated μ, averaged over the number of point-masses, against the number of point-masses, as done in Figure 5.3, shows a clear increase in error with the number of point-masses. By looking at the spatial distribution of this error, as shown in Figure 5.4, it is observed that the error is lower when more on the outside of the mascon model. As the outer point-masses come closest to the spacecraft with respect for the inner point-masses, its acceleration influences the spacecraft most and these mascons are estimated most accurately. This corresponds with the explanation given for the observed relationship in Figure 5.2b.

5.2.2. Covariance analysis

Besides the resulting variances of the parameters, the EKF also gives covariances. Using the covariance matrices, given as output by the EKF, the correlations between the state parameters can be derived. Using the resulting covariances between state-parameters, the correlation between these two

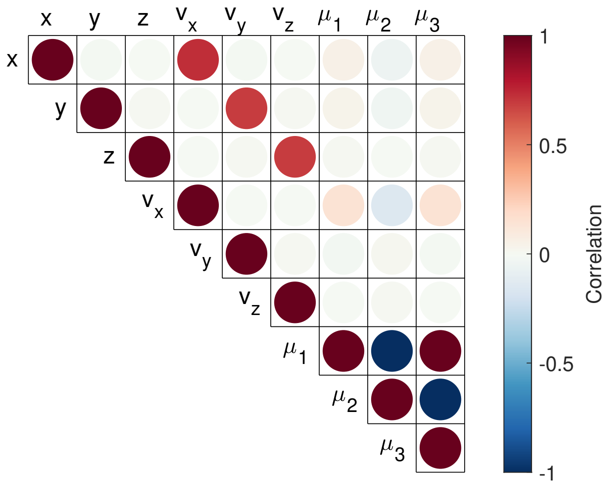

Figure 5.5: Correlation after convergence for three point-masses.

variables can be calculated using:

$$corr(X,Y) = \frac{cov(X,Y)}{\sigma_X \sigma_Y}, \tag{5.1}$$

where σ_X and σ_Y are the standard deviations of variables X and Y. If the estimation converges, for example, when using 3 point-masses, μ_1 positioned at $(5,\ 0,\ 0)^T$, μ_2 at $(0,\ 0,\ 0)^T$ and μ_3 at $(-5,\ 0,\ 0)^T$ km, a correlation matrix as visualized in Figure 5.5 is given by the EKF. It is observed that the outer two point-masses have a clear positive correlation. This makes sense, as the center of mass would be influenced when these would have an error independently from each-other. This change of center of mass would influence the direction of acceleration highly. The middle point-mass has a negative correlation with both the outer point-masses. This correlation is also as expected. If the correlated outer would have an error, the middle mass would have an opposite error which compensates for this mass error to obtain the same acceleration. However, such higher average error in estimated gravitational parameter for more point-masses does not necessarily mean a higher error in position and velocity.

Besides the gravitational parameters, there exist also correlations between position and velocity coefficients. The correlations in Figure 5.5 show that the velocity directions are correlated with the corresponding position directions. Because an error in the velocity in the x-, y- or z-direction, would result in a position error in this same direction, this is as expected. A converged solution, should give a similar correlation matrix.

To see what happens if the weight is put on the measurements and the estimation accuracy is dominated by the noise in the measurements, the diagonal elements of the process noise matrix **Q** are set to the relatively high value of 1. Since this refers to the test done in subsection 4.3.3, the resulting accuracies in position, velocity, and the sum of gravitational parameters were plotted in Figure 4.23a against the time. These plots clearly show a by noise dominated estimation in all state parameters. The resulting correlation matrix, as shown in Figure 5.6a, also shows the relation between the position and velocity, but the relation between the gravitational parameters and with any other state parameter is lost. This emphasizes the dominance of the measurements, as the relations between the dynamical model defining gravitational parameters are ignored by the filter.

The opposite can be done, by setting very low values for diagonal matrix **Q** and thus putting more weight on the dynamical system. When setting all values of **Q** equal to zero, as done in subsection 4.3.3 the accuracies in position and velocity as shown in Figure 4.23b are obtained. The plots clearly show divergence at some point. The final correlation matrix corresponding to the shown divergence is given

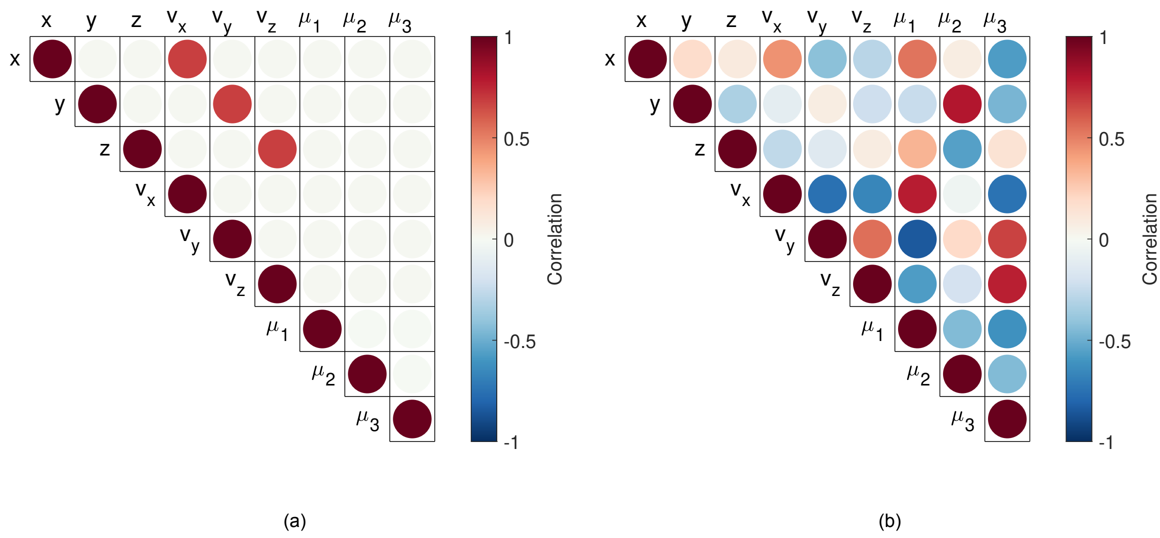

(a) (b)

Figure 5.6: Plot of the resulting correlation matrix using (a) $\mathbf{Q} = \mathbf{I}$, and (b) $\mathbf{Q} = \mathbf{0}$, corresponding to the results in Figure 4.23.

in Figure 5.6b. The matrix shows correlations between parameters, but distributed randomly. The correlation between position and velocity directions is almost gone and other correlations have appeared. This clearly shows the filter does not work as desired.

5.3. Mission phases

From this point on in the thesis, the EKF is tested using measurements from the real-world simulator using the polyhedron model. By using the polyhedron gravity model, the estimated mascon gravitational parameters cannot be directly related to the real world. The behavior of the gravitational parameter estimation is analyzed with respect to the orbit characteristics and mascon model definition. To see what final model precision results from gradually refining the mascon model, a three mission phases at different altitudes are simulated. Over time, the distance between spacecraft and asteroid is decreased during the mission. In this section, the performance of the EKF is analyzed along the asteroid mission consisting of three phases at an initial semimajor axis of 200, 50 and 35 kilometers.

5.3.1. Scenarios

As stated, the mission phases differ in initial altitude. Using the simulator, the spacecraft is initialized according to a circular orbit around a mascon of the mass of the defined asteroid Eros. The initial positions $\mathbf{r}_{in} = (x_{in}\ y_{in}\ z_{in})^T$ of the three mission phases are set on the x-axis, what implies y_{in} and z_{in} are equal to 0. The orbit radius is thus equal to x_{in}, which are set to 200, 50 and 35 kilometers for the first three mission phases. The initial velocity is then set using:

$$\mathbf{v_{in}} = \begin{pmatrix} 0 \\ \sqrt{\frac{\mu}{||\mathbf{r}_{in}||}}\cos(i) \\ \sqrt{\frac{\mu}{||\mathbf{r}_{in}||}}\sin(i) \end{pmatrix}, \tag{5.2}$$

where the orbit's inclination is indicated with i. For this analysis, an asteroid with a homogeneous density distribution is defined. Later, the results are compared with results using simulations around heterogeneous asteroids.

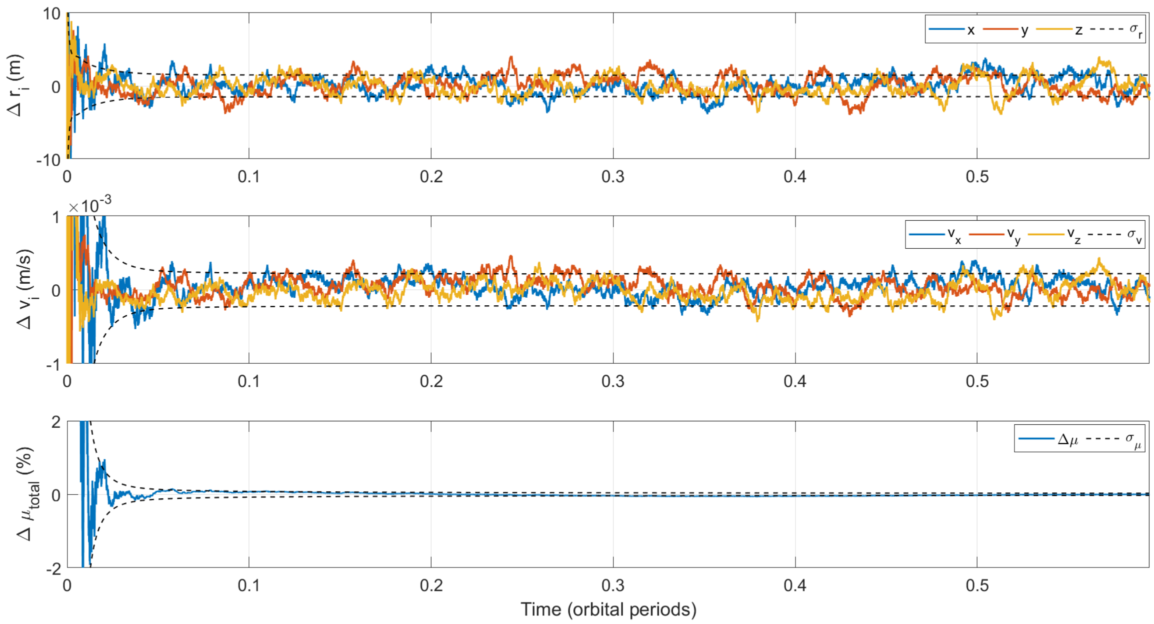

Figure 5.7: Errors in position, velocity and gravitational parameter plotted over time for a 200 km orbit using 1 point mass and position measurements with a standard deviation of 100 meters.

5.3.2. Increasing model accuracy

During a mission, the closer the spacecrafts gets, the higher the required accuracy in the gravity model becomes. Close to the asteroid, the gravitational pull from the asteroid is higher, what includes small differences in the gravity field due to the irregular asteroid shape and mass distribution also having more influence. The more point-masses, the higher the precision of the gravity field model. However, the first step is to define one point mass in the center of the asteroid, which should represent the total mass of the asteroid. An orbit with an inclination of 60 degrees is simulated for the first steps. The initial values for the simulator and EKF are given in Table 5.1.

Table 5.1: Initial values for the simulator and EKF.

Initial position (km)	$\mathbf{r}_{in}$	(200 0 0)
Initial velocity (m/s)	$\mathbf{v}_{in}$	(0 0.7473 1.2944)
Initial position estimate (km)	$\mathbf{r}_0$	(201 1 1)
Initial velocity estimate (m/s)	$\mathbf{v}_0$	(1 -0.2912 1.7455)

The initial error and uncertainty in the total mass are set to 30%, because it is assumed some preliminary knowledge is gained about the possible density ranges of the asteroid by spectroscopy. Assuming a carbonaceous asteroid, the density can vary from about 2000 to 3000 kg/m^3, would mean a spread of about +20 to -20%. With an additional buffer, the broad estimate is set to 30%. At 200 kilometers, the gravitational parameter $\mu = GM$ can be estimated up to high accuracy using noisy position measurements with a standard deviation of 100 meters. This is shown in Figure 5.7. Also, the position and velocity are improved significantly by the EKF compared to the measurement accuracy and initial errors. The next step is to see whether the model improves using two point-masses. As the felt gravitational attraction by the spacecraft is most sensitive for position, the defined position of the point-masses is of importance. Consequently, the estimated gravitational parameters are dependent

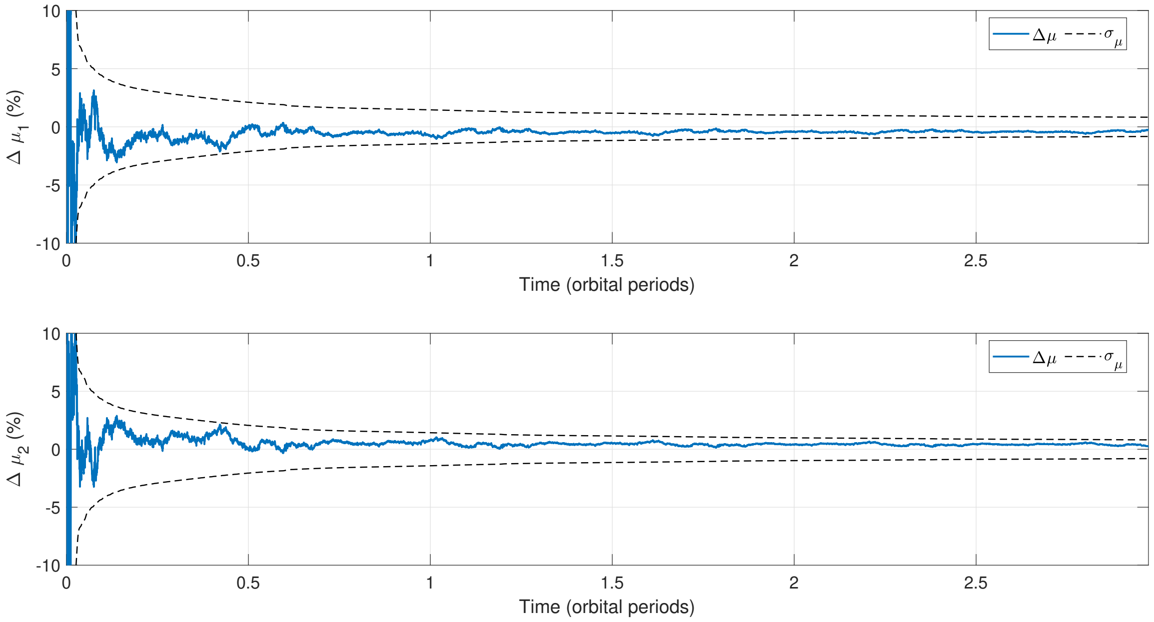

Figure 5.8: Estimation errors in the gravitational parameters plotted over time for a 2 point-mass model at 200 km.

on their position in the asteroid. Since the conversion from the polyhedron model towards the mascon model cannot be done analytically, single values for the gravitational parameters towards which the EKF should converge cannot be determined. An estimation is done using the 3D-volume shape model and summing up the mass elements in the asteroid closest to the mascon position. When defining the two point-masses on the x-axis of the asteroid-frame at +10 and -10 kilometer, the resulting estimated values agree with these expected values. Assuming the expected value is the correct value, the estimation error is plotted over time in Figure 5.8. The plot shows a clear decrease in convergence speed and accuracy with respect to the single point-mass model. This can be explained by the higher order gravity field effects being felt less accurately compared to the total μ. Nevertheless, the accuracy in estimation of the total mass as the sum of the two estimated values is similar to the result when using one point-mass. The variance over time can be calculated using the following equation (Park et al., 2010):

$$\sigma^2_{\mu,total} = \mathrm{var}(\mu_{total}) = \sum_i \sum_j \mathrm{cov}(\mu_i, \mu_j) \tag{5.3}$$

Here, it yields that $\mathrm{cov}(X, X) = \mathrm{var}(X)$. As the EKF gives the complete covariance matrix over time, this equation can be applied to calculate the 1σ error over time of the sum of the gravitational parameters. This smaller improvement for the individual point-masses compared to the total emphasizes the high negative correlation between the two point masses.

Using a lower measurement error, the estimation converges towards different values for the gravitational parameters. As the position and velocity is determined with higher accuracy when using a lower measurement error, the acceleration is also determined with higher accuracy. As the position and thus acceleration can be estimated more accurately, the EKF is expected to be more sensitive for the error in the estimated gravitational parameter. To see which measurement accuracy gives a better estimation, the differences between the real gravity field and the estimated gravity fields are given in Figure 5.9. For comparison: at 200 km, the point-mass acceleration is $1.117 \cdot 10^{-5}$ m/s^2. Comparing the two figures, it shows lower extrema in the gravity error for the higher measurement accuracy. This result is as expected, because a small measurement error increases convergence speed and accuracy,

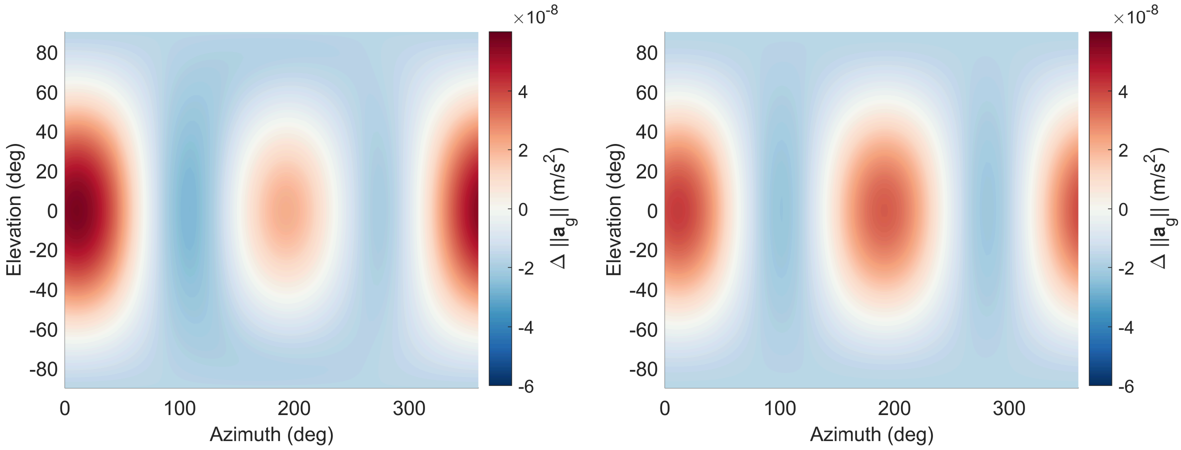

(a) Error of estimated gravity field using σ_z = 100 m.

(b) Error of estimated gravity field using σ_z = 10 m.

Figure 5.9: Difference in gravitational acceleration between real polyhedron gravity field and estimated mascon gravity field at R=200 km.

as higher order gravity field influences on the spacecraft position can be detected more accurately.

Dependency on mascon position

By increasing the mascon model to three point masses, the resulting variances show the importance of position. As seen earlier, point masses in the middle of other point-masses result in a more uncertain estimation. This is also the case when adding one mascon between the mascons of the 2 point mass model. Besides this option, Model 3-1, an alternative point-mass models is considered. The alternative model, Model 3-2, is chosen manually trying to represent the shape best as possible. This model does not have a middle point-mass, but all three mascons are placed near an extreme of the shape. The position vectors of the Model 3-2 mascons are (-14 -0.2 0), (-1.2 4 0), and (12 -4 0) km. Both models are visualized in Figure 5.10 with their resulting estimation uncertainty. The model was again initialized with a 30% error and uncertainty for both models in order to be able to compare the results. The figures shows a large improvement in its uncertainty when using, Model 3-2, with respect to Model 3-1. This shows the importance of the selected position for the point-masses. The difference between the two models is also shown in the resulting correlations between the point masses. Both models result in high correlations between the point-masses. However, Model 3-1 results in higher correlations with respect to Model 3-2. The absolute correlations between the point masses of Model 3-1 are all higher than 0.85, while these resulting correlations start from 0.53 for Model 3-2. This emphasizes the disadvantage of having middle point masses as already found in section 5.2, because a high covariance between point-masses makes it difficult for filter to decouple the estimates (Park et al., 2010).

Increasing the model to 4 point masses does not show clear convergence for measurements of 100 meters accuracy. Therefore, the altitude is decreased to 50 kilometers. As the higher order gravity terms influence the trajectory of the spacecraft more when the spacecraft is closer, the estimation converges faster and the uncertainties become smaller. Again, the positions of the point-masses appear to play a major role in obtaining estimated values which are in the range of expected values. Also for the 4 point masses, two approaches to distribute the point masses are assessed. The first model model, Model 4-1, splits the asteroid in four quarters by, first, dividing the shape in two halves using the YZ-plane at the center of mass. Subsequently, the center of mass of both halves is determined and each half is divided by the XY-plane through their center of mass. The center of mass of the four quarters determine the position of the mascons. The positions of the second model, Model 4-2, are selected manually based on the shape of Eros. The position vectors of the Model 4-2 mascons are (-12 -0.2 0), (-3.3 5 0), (7.5 2 0), and (10 -5 0) km.

Again, the choice of mascon positions is of influence on the estimation. The estimation results regarding μ-estimation are given in Table 5.2. Both models result in small uncertainties. However,

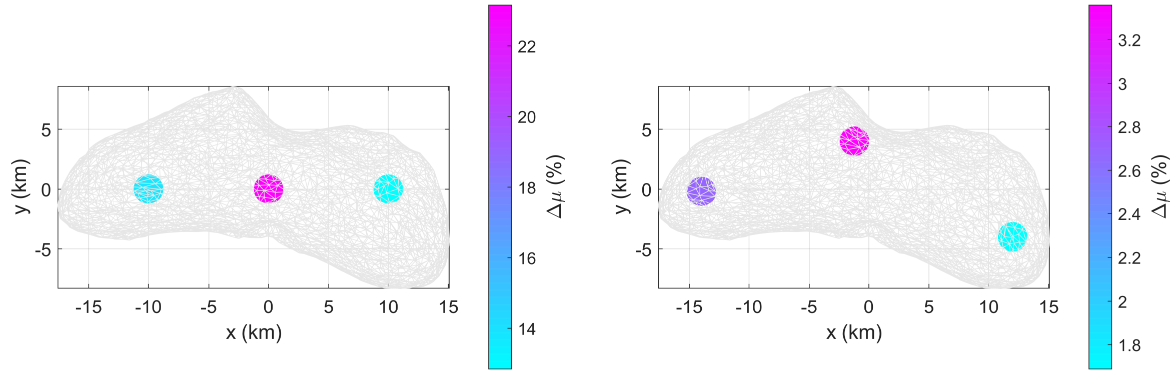

(a) Model 3-1.

(b) Model 3-2.

Figure 5.10: Resulting accuracy in μ estimation as a percentage of the resulting estimated value for a circular orbit with a 200 km radius.

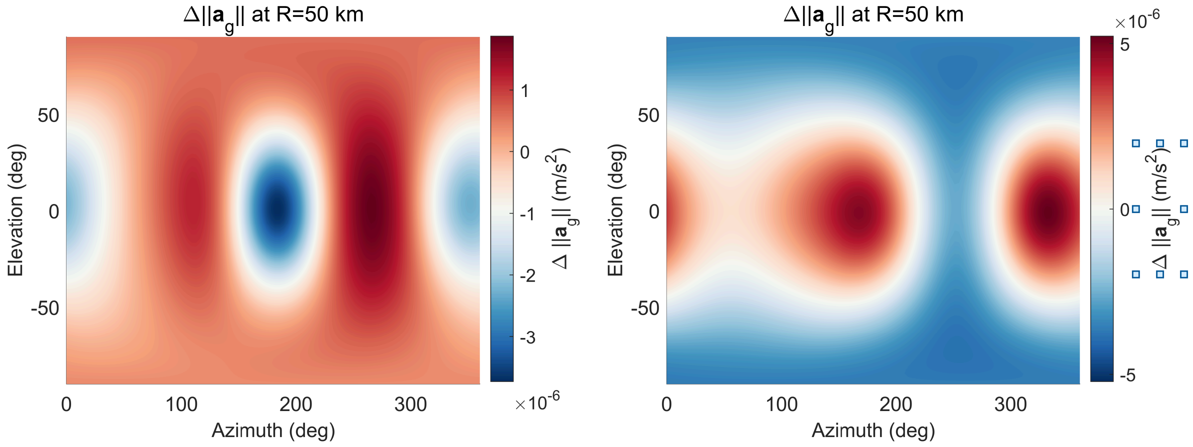

(a) Model 4-1

(b) Model 4-2

Figure 5.11: Surface plot of the error in gravitational acceleration magnitude on a sphere with a radius of 50 kilometers for the 4 mascons models.

again the manual model, Model 4-2, results in smaller uncertainties in the estimation of the gravitational parameters. Besides this smaller uncertainty, the estimated values resulting using Model 4-2 give values inside the range of expected values. If it is desired to relate the estimated distribution to the density distribution of the asteroid, these values seem more relatable to reality. However, when looking at the estimated accelerations, Model 4-1 results in a more accurate gravity field. Using Model 4-2 results in a less accurate total mass estimation, what could cause this higher error in the gravity field. Therefore, a constraint is put on the sum of the estimated parameters. Although the small error ($\approx$ 0.1 %) in the total mass of the point-masses is eliminated, the asteroid gravity field using Model 4-2 is still worse than Model 4-1. This is shown in Figure 5.11. For comparison: at 50 km, the point-mass acceleration is $1.787 \cdot 10^{-4}$ m/s^2. The on the centers-of-masses based Model 4-1 does represent the gravity field better as the resulting error in gravitational acceleration is lower.

As the results converged for four point-masses, the complexity of the gravity model is increased to eight point-masses. Again, two models are tested. Model 8-1 uses the same method as Model 4-1, but splits the asteroid in eight parts by splitting each part of Model 4-1 by the XZ-plane through their center of mass. The eight mascons are placed in the center of mass of each part. Model 8-2

Table 5.2: Results for the 4 point mass models at a 50 km orbit with 60 degrees inclination after a simulation time of 1,500,000 seconds.

Model	Final covariance (%)	RMSE (10^{-6} m/s^2)	RMSPE (%)	MAE (10^{-6} m/s^2)	MAPE (%)	Maximum error (%)
4-1 unconstrained	1.9250	1.2626	0.6949	1.1024	0.6149	1.9410
4-1 constrained	1.9247	1.2651	0.6971	1.1125	0.6209	1.9227
4-2 unconstrained	1.2279	3.0791	1.7297	2.9761	1.6765	2.9039
4-2 constrained	1.2274	3.1103	1.7506	3.0075	1.6956	2.8248

Table 5.3: Results for the 8 point mass models at a 50 km orbit with 60 degrees inclination after a simulation time of 1,500,000 seconds.

Model	Final covariance (%)	RMSE (10^{-6} m/s^2)	RMSPE (%)	MAE (10^{-6} m/s^2)	MAPE (%)	Maximum error (%)
8-1	10.7836	1.5907	0.8797	1.4711	0.8234	2.2222
8-2	9.8824	2.6702	1.4985	2.5612	1.4421	2.5382

uses the chosen X and Y positions of Model 4-2, and defines a point mass at +2 and -2 km in the Z-direction for each X-Y combination of Model 4-2. The results are given in Table 5.3. According to these results, Model 8-1 based on the centers of mass gives the best gravity field estimation. However, the gravitational parameters are not yet completely converged towards one solution. For model 8-2, the estimation clearly converges towards certain values. The observations that Model 8-1 did not converge towards one solution in the set simulation time, but the acceleration does, which are shown in Figures 5.12 and 5.13, respectively, emphasizes the ambiguity of the mascon model. The μ values converge towards values which minimize the acceleration error as far as possible, but this is not a clear single stable optimum. The gravitational parameters seem to slowly converge from this state towards their final value. However, coming closer to this value does not seem to increase the accuracy of the acceleration prediction. The variation in the acceleration error is due to the spacecraft position during the simulation with respect to the asteroid body. As the asteroid rotates around the z-axis and the spacecraft orbits the asteroids, the relative spacecraft position changes quickly over time. As can be seen in, for example, Figures 5.9 and 5.11, the discrepancy between the mascon model and real-world polyhedron model varies over the relative position. Especially near the elongated poles, the errors becomes largest, what explains the periodic peaks in Figure 5.13. Since lowering the measurement accuracy, and consequently increasing position and velocity estimation accuracy, does not increase the acceleration accuracy, the error in this acceleration estimation dominated by the discrepancy of the defined model with the polyhedron model. Decreasing the altitude does not solve the problem of convergence for Model 8-1. The values for the gravitational parameters show the same behavior as for Model 4-1.

Dependency on orbit characteristics

As shown before, the estimations converge more quickly at low altitudes, because the gravitational pull is higher closer to the asteroid. Also the uncertainty of the gravity estimation decreases faster and further when orbiting the asteroid at a lower altitude. However, the uncertainty in the estimation of the position and velocity increases with lowering the altitude. Nevertheless, also this behavior is as expected, because the influence of the gravity field increases and the difference between the used gravity model and the reference real-world model becomes more dominant. Increasing the number of point-masses should decrease this error, as the accuracy of the gravity field should increase.

To test whether the position and velocity estimates increase when using more point-masses, the obtained errors are plotted over the number of mascons. To obtain these plots, the mascon models 3-2, 4-2 and 8-2 are used besides the single and double point-mass models as described above. For a fair comparison, initial state-errors are kept equal, with an initial position error of 100 meters in each direction and an initial estimated error of 30% of the expected value, which is calculated as stated before. The used measurement standard deviation is 100 meters and each 60 degrees inclined trajectory is simulated for 500,000 seconds.

The resulting Figures 5.14a and 5.14b show a decrease in the estimated 1-σ errors with increasing

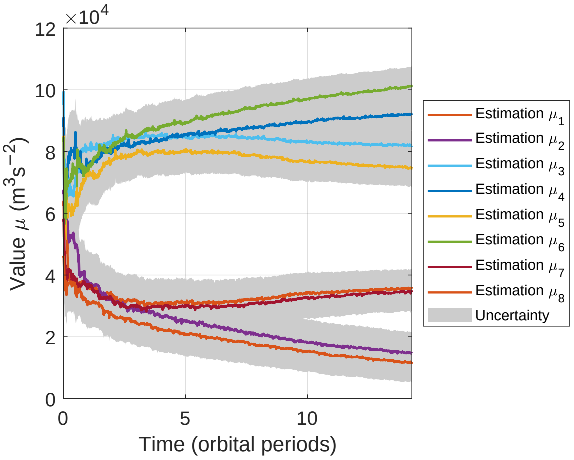

Figure 5.12: Estimations of the gravitational parameters over time with their uncertainties using Model 8-1 at 50 kilometers.

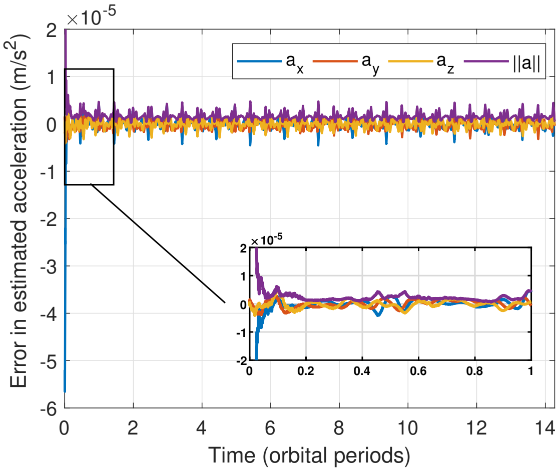

Figure 5.13: Error in acceleration plotted over time using Model 8-1 at 50 kilometers.

the number of point masses. This estimated accuracy is dependent on the process noise matrix **Q**. It appeared that the more elements used in the mascon model, the lower the tuning values can be set, and thus the more the filter can rely on its dynamic model. For an orbit radius of 200 kilometer, the gravity field seems to be modeled quite well using one or two mascons, as the accuracies do not to consistently improve with increasing the number of point masses. Looking at the obtained acceleration accuracy in Figure 5.14c confirms this explanation. For the orbits closer to the asteroid, a similar behavior as in the position and velocity estimated accuracy is shown in the observed acceleration accuracy, while the acceleration at a radius of 200 kilometer the acceleration does not follow the same trend over the number of mascons.

Besides the their uncertainties, also the estimated values for the gravitational parameters appear to be dependent on the orbit characteristics. In Figure 5.15, the estimated values after 500,000 seconds are plotted against the orbit inclination for multiple altitudes, using Model 3-2. This model is chosen as it showed convergence for each altitude. The figure shows the model depends on the orbit characteristics. The figure shows a variation in the estimation values over the inclination of a orbit. However, the variation over orbit inclination decreases when lowering altitude, as also the estimated error decreases. This decrease in variation can be explained by the higher order gravity terms having more influence on the spacecraft's trajectory at lower altitude and therefore more consistent estimation. With respect to the orbit radius, the estimated values vary significantly, as most values do not lay in the error margins the values estimated at a higher orbit. Such variation can be explained by the discrepancy between the gravity model and the real world. As the assumed mascon gravity model does not model the real gravity field correctly, lowering orbit could require the estimated values to adjust to different values as the influence of higher order terms increases. These findings imply the estimated values for cannot be assumed true before going to a different orbit without doing more research.

5.3.3. Stepwise approach

When using three different mission phases at 200, 50 and 35 kilometers, the resulting model estimations of one phase can be used as a starting point for the next mission phase. Each mission phase consists of initially circular orbits of the inclinations 90, 60, 45 and 0. When a change of inclination is made, the resulting position error is used as the initial error and the resulting covariance matrix is used as the initial covariance matrix. When decreasing altitude, the initial position and velocity error are estimated to be about 100 meters and 0.01 m/s. Using information from earlier results when increasing the number of mascons to describe the asteroids gravity field appears to be quite difficult. To be able to use the information of an earlier estimation, the number of mascons is doubled each improvement. In this way,

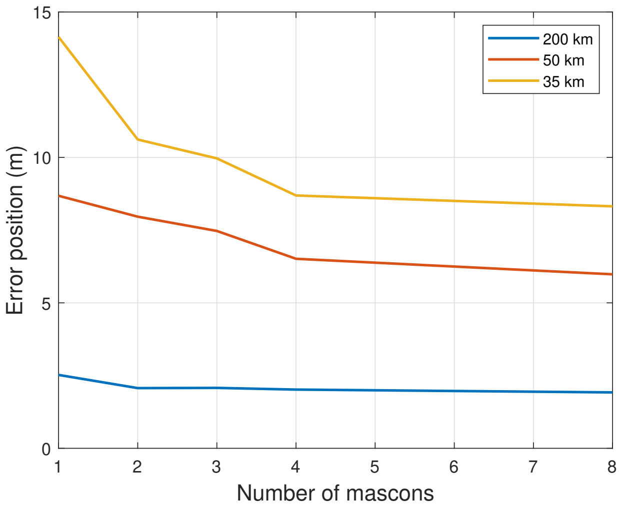

(a)

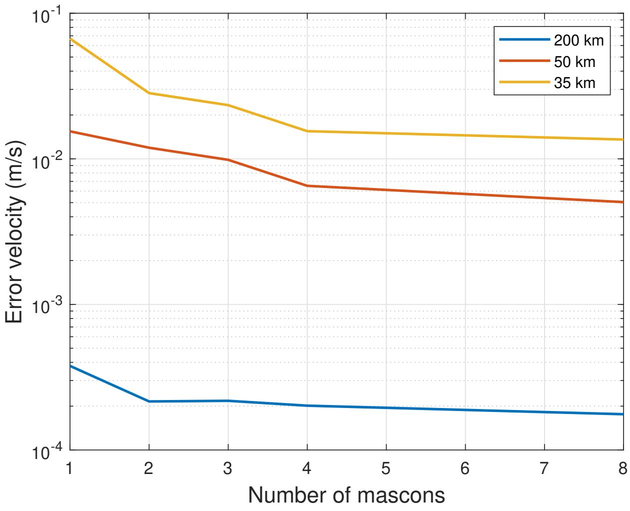

(b)

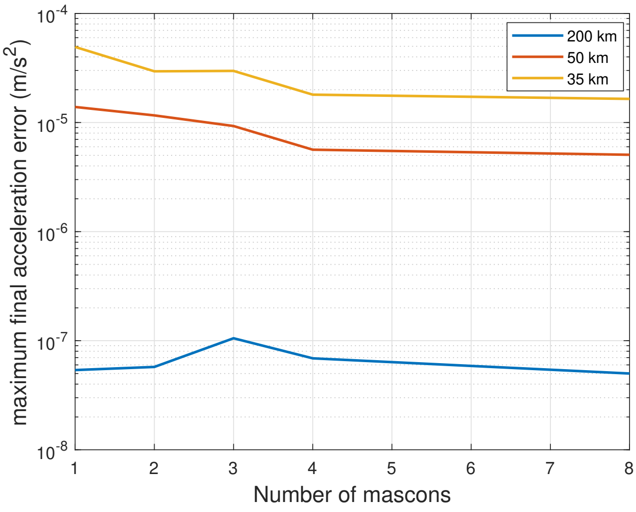

(c)

Figure 5.14: Plots of (a) the estimated accuracy in position, (b) the estimated accuracy in velocity, and (c) maximum acceleration-error of the last period, plotted over the number of mascons for different altitudes.

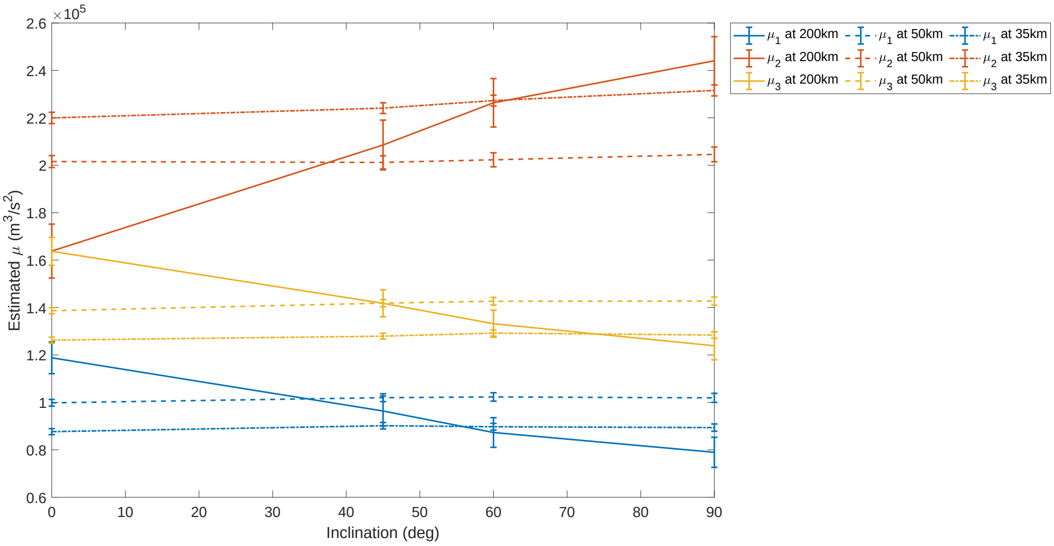

Figure 5.15: Resulting value and uncertainty of gravitational parameter after 500,000 seconds using the Model 3-2 plotted over orbit inclination.

a point mass can be split in two and used as initial guess for the next step. The method used for splitting the asteroid in parts, as used for Model 4-1 and 8-1, based on the centers of mass of asteroid parts is used when defining the mascon positions. The initial guess for the μ-values of these new mascons is based on the estimated density, using the volumes of the 3D-volume elements which are closest to the particular mascon position. This estimated density is then used to calculate the estimated mass of the new mascon with a smaller assigned volume. The initial guess for the deviation of the gravitational parameter values are based on the possible density-differences between the two parts that formed one part a step earlier, assuming a carbonaceous asteroid with a maximum density of 3000 and minimum density of 2000 kg/m^3. Hereby it is assumed there is some knowledge about the possible composition by spectroscopy. For example, the estimated single point-mass gives an average density ρ_{avg} for the whole asteroid. Knowing this average density and having the shape model available, the extreme cases where one half of the asteroid only consists of the highest possible and the other of the lowest possible density can be calculated. In other words, the highest and lowest possible μ's are calculated and the largest difference between the average and these maxima are used as initial covariance. At 200 kilometers, the estimations are performed for the one and two mascon model. At 50 kilometers, the two and four mascon models are used for estimation. Finally, at 35 kilometers, the four and eight point-mass gravitational parameters are estimated. When repeating an estimation of a certain mascon model at lower altitude, the values and estimated covariances for this model are used as initial conditions.

The estimated values and their uncertainty using the eight-point-mass model are given in Figure 5.16a. The initial values for these mascon parameters are based on the estimations of the four mascon model. As can be seen, some μ-values go below zero. These point masses represent a negative mass. Although these estimated values give no direct expectation about the mass distribution inside the asteroid, the resulting gravity field at 35 kilometers is quite similar to the polyhedron gravity field. The difference between the resulting gravity field and the real gravity field, calculated for 100,000 points over a sphere with a radius of 35 kilometers, is given in Figure 5.16b. The point mass acceleration at 35 kilometer is $3.647{\cdot}10^{-4}$ m/s^2 The RMS error and mean error of the gravity field are $6.9041{\cdot}10^{-6}$ and $6.2497{\cdot}10^{-6}$ m/s^2 (1.8521 and 1.7173%), with a maximum error of $2.2123{\cdot}10^{-5}$ m/s^2 (5.1694%). The relatively large difference between the maximum and mean error indicates the small area in which the relatively high errors occur, which can be seen in Figure 5.16b, indicated by the blue area.

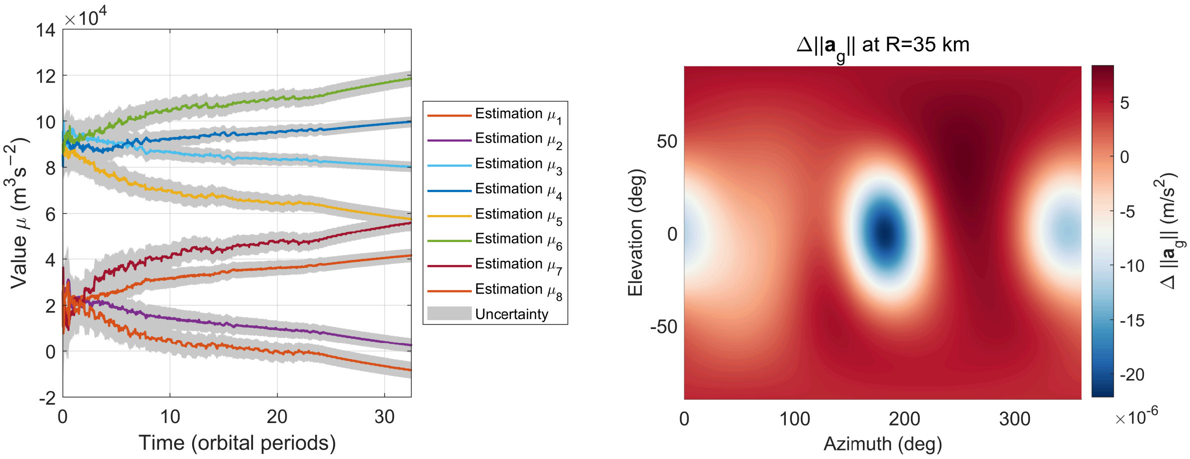

(a) Gravitational parameter estimated value plotted against the time for a 35 kilometer orbit.

(b) Surface plot of the error in the estimated gravity field.

Figure 5.16: Gravitational parameter estimation results for asteroid configuration 2 using the CoM-based model.

Using the chosen models, as in Model 4-2 and Model 8-2, and using the same technique as for the above assuming a split of a part of the asteroid when doubling the number of mascons, different results are observed. The results of this model are given in Figure 5.17. The RMSE and MAE of this result are equal to $1.1121 \cdot 10^{-5}$ m/s^2 and $1.0687 \cdot 10^{-5}$ (3.1347 and 2.9982%), with a maximum error of $1.5712 \cdot 10^{-5}$ (4.7265%).

5.4. Heterogeneity

To analyze the dependence of the Kalman filter on the asteroid interior, the spacecraft is brought into orbits around three different asteroid-configurations. These asteroid-configurations differ in their degree of heterogeneity, expressed by its density-range. The first asteroid is the homogeneous case, which has an uniform density and is already analyzed intensively. This homogeneous distribution is indicated as distribution 1. The two other configurations are heterogeneous asteroids. The density distributions are generated using the Matérn covariance function, all with the same random seed 1. This seed is selected based on its longitudinal characteristic. This longitudinal distribution represents a hypothetical contact-binary asteroid.

Density distribution number 2 is defined using a smoothness parameter of 1.5, a scaling parameter of 2 and a standard deviation of 300. It is made sure the total mass of the homogeneous asteroid is equal to the mass of this asteroid. The range of densities is based on the range of average bulk densities determined in carbonaceous chondrite types CM and CO, according to Table 2.2 (Consolmagno et al., 2008). The asteroid and its density distribution is visualized in Figure 5.18a. Because of the longitudinal distribution, the +X-side of the asteroid has a lower density than the −X-side. The third used density distribution, distribution 3, is highly heterogeneous. The range of densities of this hypothetical extreme case is based on the densities of an average M- and C-type asteroid as mentioned in Table 2.3 (Consolmagno et al., 2008). To obtain such distribution, the maximum is set equal to the iron-rich M-type average bulk density value of 4700 kg/m^3 and the standard deviation σ is increased to 1400 kg/m^3. This gives the distribution as visualized in Figure 5.18b. As shown, the longitudinal distribution is applied again.

As for the homogeneous case, the EKF is tested on he three mission phases at 200, 50 and 35 kilometers. The same models are defined and the same steps are taken during the mission as described in subsection 5.3.3 for the homogeneous case. The initial conditions follow Equation 5.2, with μ according to the defined asteroid mass.

During the high orbit phase, the point-mass gravity $\mu = GM$ is estimated. This high-orbit phase is

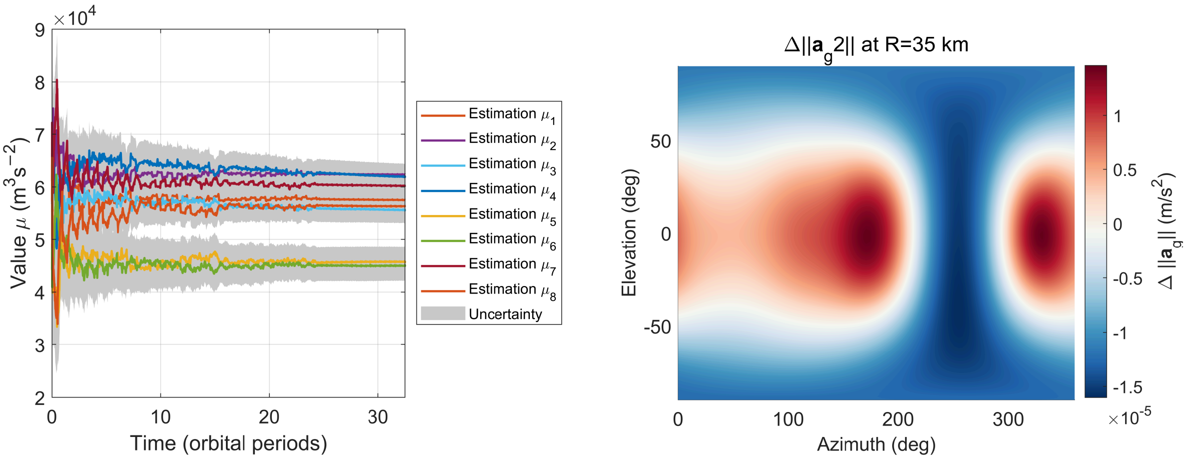

(a) Gravitational parameter estimated value plotted against the time for a 35 kilometer orbit.

(b) Surface plot of the error in the estimated gravity field.

Figure 5.17: Gravitational parameter estimation results for asteroid configuration 1 using the chosen model.

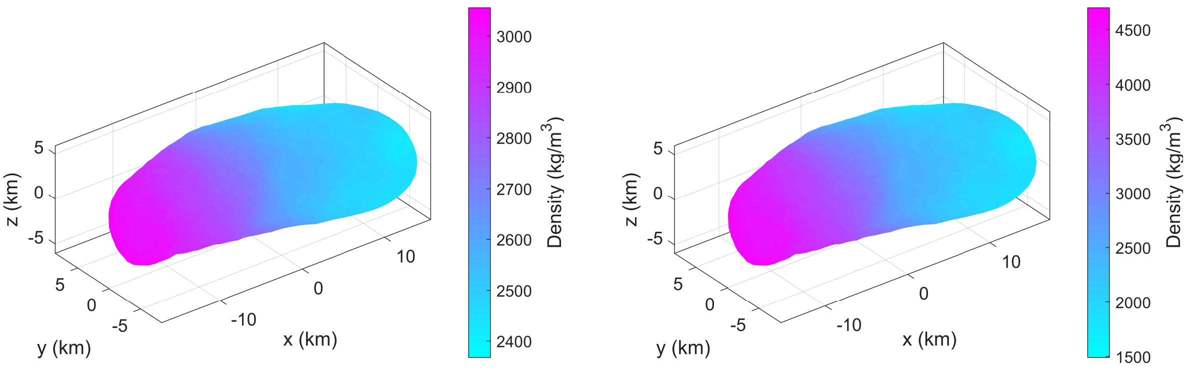

(a) Distribution 2.

(b) Distribution 3.

Figure 5.18: Heterogeneous density distributions

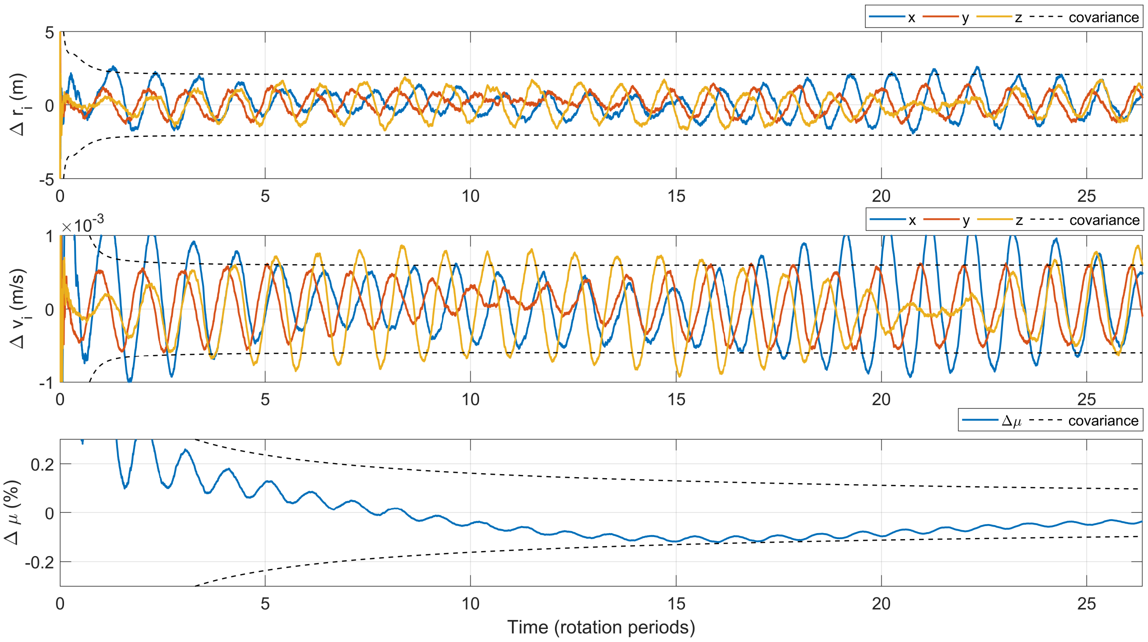

Figure 5.19: Estimation errors over time in position, velocity and gravitational parameter for 200 kilometer with point mass located at the CoF.

a circular orbit with a semi-major axis of 200 km with an inclination of 90 degrees. In Figure 5.19, the errors in estimated position and velocity components, and gravitational parameter are plotted against the time in orbital revolutions. Because of the great distance from the asteroid, the orbit is almost completely circular, whereby the asteroid can be approximated by a single point-mass effectively. This causes the estimation to be quite accurate. However, compared to the homogeneous case the accuracy is worse and a fluctuation is observed. As can be seen in the figure, the fluctuation in the figures corresponds with the rotation period of the asteroid. This is because the single point-mass is set at the CoF. One should mind, that the CoM of heterogeneous asteroids is misaligned with the CoF. As bodies rotate around their center of mass, which in this case is not the center of figure, the asteroid real world is unrealistic. Therefore, an adaptation to the asteroid model is made. The new center of mass of these mass-distribution is manually aligned with the origin of the asteroid and inertial reference frame. In other words, the asteroid shape model its vertices are all shifted with the difference between the CoF and CoM. As the shape model used for the real-world simulator is shifted, consequently, also the chosen point-mass models for the navigation system are shifted with the same displacement.

5.4.1. Outcomes

For each density distribution and model, the estimation of the gravitational parameters are plotted over time with their estimated uncertainty, and the resulting gravity field at 35 kilometers are plotted. A summary of these results is given in Table 5.4, in which the corresponding figure is referenced per distribution-model combination. As can be seen in this table, comparing the results of the different density distribution, quite similar accuracies are observed for each model. This implies there are no disadvantages found of having a heterogeneous density distribution.

5.4.2. Density estimation

It appeared difficult to make a link between the estimated mascons and the asteroid's density distribution. Assigning the mass elements in the asteroid 3D volume shape model to the closest mascon and summing up the volume of the elements for each mascon, gives an estimated density distribution.

Table 5.4: Summary of results

Distribution	Model	Figure	Final covariance (%)	RMSE (10^{-5} m/s^2)	RMSPE (%)	MAE (10^{-5} m/s^2)	MAPE (%)	Max error (10^{-5} m/s^2)	Max error percentage (%)
1	CoM	5.16	5.5769	0.69041	1.8521	0.62497	1.7173	2.2123	5.1694
2	CoM	A.1	6.2058	0.70778	1.9110	0.65431	1.8022	2.0406	4.7750
3	CoM	A.3	5.7906	0.75989	1.8797	0.69086	1.7437	1.9417	4.2445
1	Chosen	5.17	3.8051	1.1121	3.1347	1.0687	2.9982	1.5712	4.7265
2	Chosen	A.2	4.6331	1.1119	3.1389	1.0667	2.9951	1.6183	4.7738
3	Chosen	A.4	4.1004	1.2988	3.3379	1.2157	3.1275	2.5839	5.6334

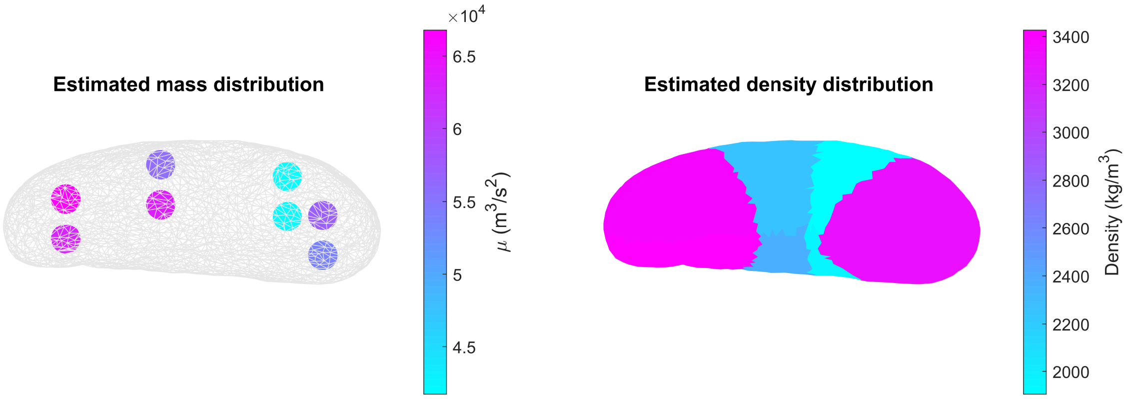

Figure 5.20: Estimated mass and density distribution for asteroid configuration 2.

Unfortunately, resulting density distributions do not relate directly to the real density distribution inside the asteroid. However, when looking at the resulting mass distributions, a comparison can be made between distributions 1 and 2.

As stated before, the chosen mascon model results in more relatable estimations for the gravitational parameters. The resulting mass and density distribution estimates for distribution 2 are shown in Figure 5.20. The real distribution is shown in Figure 5.18a. The estimated mass distribution shows more mass at the more dense side of the asteroid. However, it cannot be related directly to the interior of the asteroid. Using the volumes assigned to the mascons, the resulting density distribution in Figure 5.20 does not show a similar distribution as the real distribution.

Meanwhile, when looking at the difference between the estimated values for a homogeneous asteroid and the heterogeneous asteroid of the same mass (distributions 1 and 2, respectively), constraints could be made about the density distribution. As can be seen in Figure 5.21, the differences show a similar distribution as the real distribution. However, this only worked for the quickly towards relatable values converging chosen models. Although these chosen models resulted in a worse gravity field estimation, this indicates the advantage of this model. Using these found differences, possibly density constraints could be put on the target asteroid's interior.

5.5. Model performance

In earlier work, performed by Bourgeaux (2020), the spherical harmonics coefficients were estimated for different position noises. The spacecraft was launched into a polar 45 kilometer orbit for 10^7 seconds. It appeared that the spherical harmonics coefficients could be estimated up to degree 8 when using a position noise of 10 meters. The eighth degree spherical harmonics coefficients splits the sphere in eight parts in both directions, what defines 64 parts on the sphere. To be able to compare this precision with the point-mass model, a link between this spatial precision and the precision acquired with the point-mass model shall be made. Since analytical solution is found, this is done by defining a

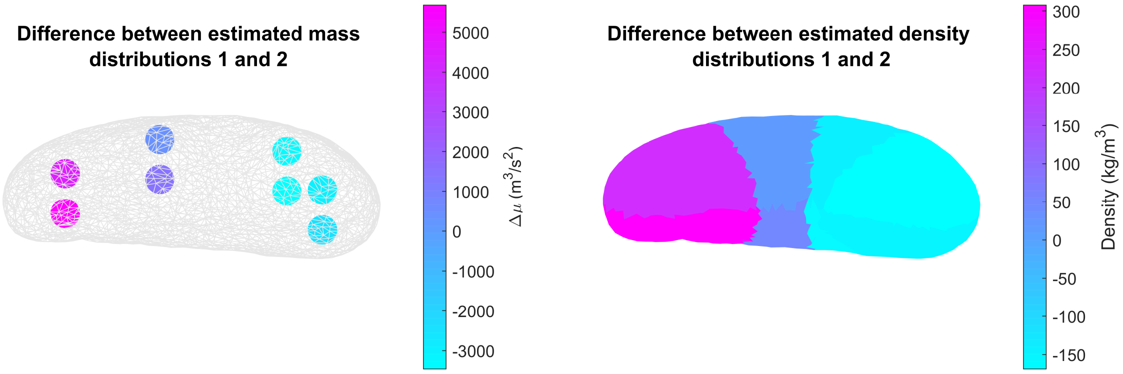

Figure 5.21: Difference between mass and density distributions 1 and 2.

mascon model out of 64 point masses. As it was observed that inner point-masses enclosed by other point-masses give high uncertainties, the approach studied by Chanut et al. (2015) is used, which is described in subsection 2.3.1. Here, a mascon model is defined using the shape model. This model connects the vertices with the center of the asteroid, such that a tetrahedron is formed for each face of the polyhedron shape model. Then, a mascon is placed at the center of each tetrahedron, by which the mascon model represents the shape of the asteroid. As the used shape model in the simulator consists of about five thousand faces, the shape model is first simplified further to a 64-faced shape model. The resulting shape model, containing the formed tetrahedra and point-masses, is visualized in Figure 5.22.

As this mascon model has a much higher precision with respect to the eight point-mass models, the added process-noise can be set much lower and the position and velocity error decrease significantly. Where, the position is estimated accurate up to about 2.5 meters using a measurement noise of 10 meters and eight point masses, the shape based 64 mascons model results in a maximum error of about 0.9 meter after 500,000 seconds. The velocity decreases from a max error of 4.9 mm/s to 0.36 mm/s.

The improvement because of the higher precision gravity model is especially observable in the acceleration. In Figure 5.23, the acceleration-error is plotted over time. This plot shows the improvement of the expected acceleration over time because of the increasing accuracy in the gravity model. Unfortunately, this improvement in the acceleration estimation is not observed in the estimated variances for the gravitational parameter estimation. As the average initial error in the gravitational parameters was set to 30%, this value only converges to an average estimated error of 20.7%.

Although this relatively high uncertainty from covariance analysis, the resulting gravity field appears to be quite accurate relatively to the degree 8 spherical harmonics gravity field. Using the estimated values for the gravitational parameters and the 64 mascons model, the error in the gravity field with the polyhedron gravity field on a sphere with a radius of 20 kilometer is calculated and visualized in Figure 5.24. At 20 kilometer, the point-mass acceleration has a magnitude of $1.1{\cdot}10^{-3}$ m/s^2. The RMS of the error in gravitational acceleration is $1.0772{\cdot}10^{-5}$ m/s^2. For comparison, the difference between the 15th and 8th degree and order measured gravity field of Eros on a sphere with a radius of 20 kilometers is given in Figure 5.25. The shown error in the spherical harmonics gravity fields is of a similar order as the error in the estimated gravity field. The RMS of the error is $2.9684{\cdot}10^{-5}$ m/s^2, which is higher than that of the estimated gravity field. This shows the mascon model can obtain a similar accuracy in gravity field estimation as the spherical harmonics gravity field.

Using the approach by Chanut et al. (2015), the theoretical model is defined by calculating the masses of the 64 point masses by multiplying the asteroid density with the tetrahedron volume which is scaled with the volumes with the volume of the polyhedron used for simulation divided by the total

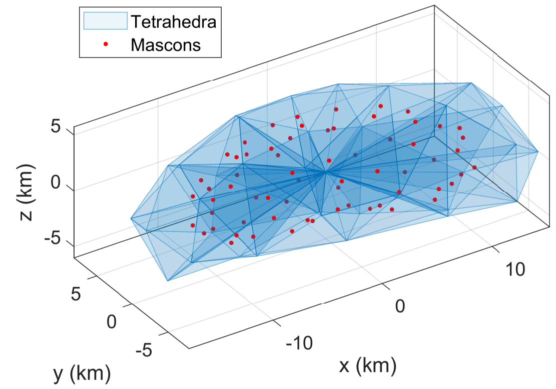

Figure 5.22: 64 faced shape model of Eros divided in tetrahedra with mascon placed at the centroid of each tetrahedron.

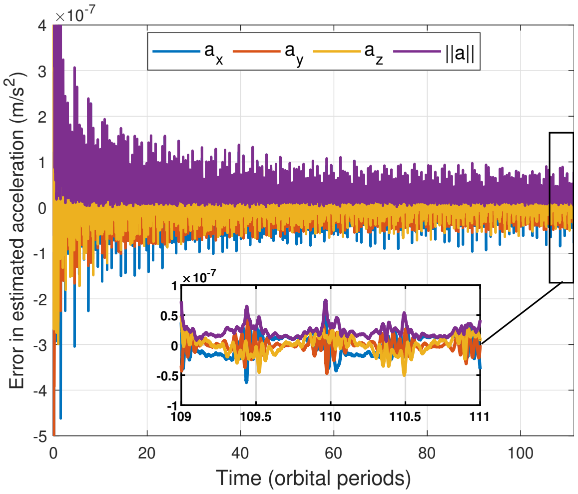

Figure 5.23: Acceleration error over time for a 45 km orbit using a 64 mascons model.

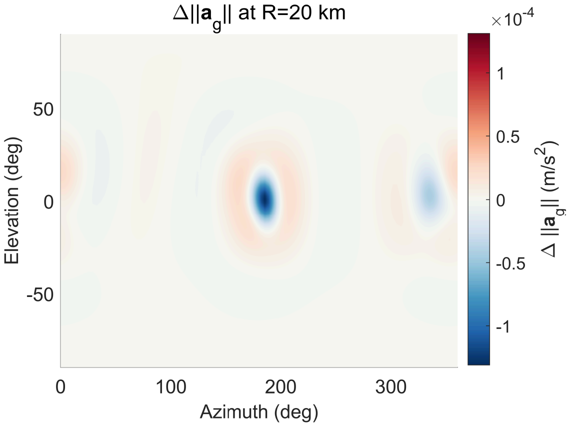

Figure 5.24: Surface plot of the error in the estimated 64 mascons gravity field on a sphere with a radius of 20 kilometers.

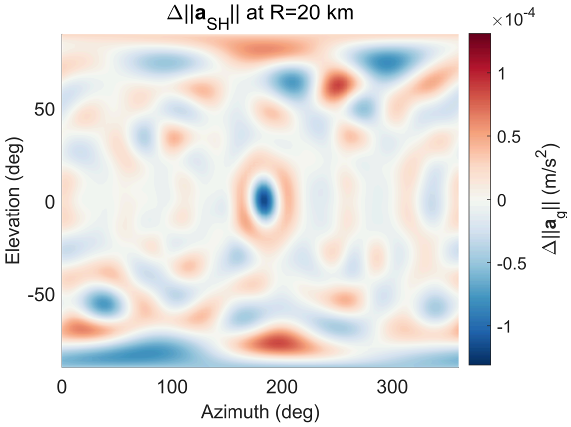

Figure 5.25: Differences between the Eros real measured gravity fields of spherical harmonics degree 15 and 8 on a sphere with a radius of 20 kilometers.

volume of the 64-faced polyhedron to eliminate the volume difference between the shape models. On a sphere of 20 kilometers, the error in the gravity field obtained by this model has a RMS of $5.0120{\cdot}10^{-5}$ m/s^2 and MAE of $2.9611{\cdot}10^{-5}$ m/s^2. The MAE of the found gravity field is $5.0864{\cdot}10^{-6}$ m/s^2. Both values show an increase in the obtained gravity field.

In the situation where no gravity field estimation would be done assuming the single point-mass gravity field, the error in the gravity field at 20 kilometers would have a RMS error of $2.7368{\cdot}10^{-4}$ m/s^2. Compared to the found gravity field, this is an improvement of a factor 10. Considering the MAE, this improvement is even larger. A single point mas results in a MAE of $2.4007{\cdot}10^{-4}$ m/s^2. This emphasizes the importance of gravity field estimation.

5.5.1. Inside Brillouin Sphere

As it is difficult to find a stable orbit inside the Brillouin with a fast-rotating asteroid without a guidance and control system, the asteroid is assumed to have no rotation for this test. A polar orbit with a radius of 15 kilometers is initialized. The resulting orbit is shown in Figure 5.26, which goes inside the Brillouin sphere. Using the estimated μ-values from the results at 35 kilometer as initial estimation,

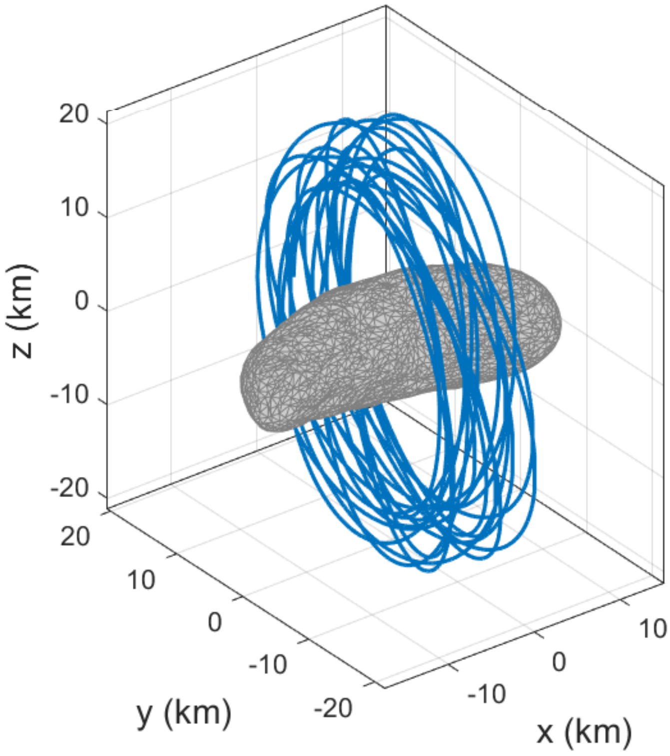

Figure 5.26: Polar orbit with an initial radius of 15 kilometers, which is inside the Brillouin sphere of Eros.

the gravitational parameters decrease from a 30% uncertainty to an average error of 4.5705% in the gravitational parameters, where position and velocity converge towards a stable orbit estimation with 1-σ errors of about 1.1 meter and 9 mm/s using position measurements with a 10 meter standard deviation. However, when using the 64-point mass model estimations, these errors are decreased to 0.8 meter in position and 1 mm/s in velocity. After an estimation of 500,000 seconds, the estimated error in the sum of the gravitational parameter was decreased from 20.7% to 14.3%. These found accuracies indicate the system also works for altitudes below the minimum Brillouin sphere of Eros.

5.6. Additional discussion

Although some promising effects are investigated of having the mascon gravity field implemented in the dynamical model for state estimation, the performed research should be put into perspective. Some limitations and made assumptions influenced the study.

It was shown that, using position measurements with a 10 meter Gaussian noise in each direction, the gravity field could be estimated more accurate than a eight degree and order spherical harmonics estimation. However, this was shown by comparing the resulting gravity fields on a sphere with a radius of 20 kilometers. As the analytical derivation between the polyhedron or spherical harmonics gravity model and the mascon model to find the correct mass distribution is lacking, the accuracy in the estimated values has to be shown in an alternative way. Compared to the results in Bourgeaux (2020), the obtained gravity field resolution exceeded the estimation accuracy using the spherical harmonics model in a similar setting. However, Bourgeaux (2020) limited the estimation to the eighth degree and could have possibly also obtained an even more accurate gravity field.

Compared to the results by Park et al. (2010), the designed EKF showed similarities to their covariance analysis. As observed in the results from Park et al., outer point-masses were estimated with a higher estimated precision than the inner point masses. Also, it was shown that lowering the orbit radius and increasing measurement accuracy, increase the estimated accuracy in the gravitational parameters. Both relations were also observed during this thesis, what confirms their observations.

The main benefit with respect to the spherical harmonics model is the ability to reach the space inside the Brillouin sphere without divergence of the dynamical model. However, as the inversion from the measured gravity field to asteroid interior knows ambiguity, this ambiguity was also observed in the obtained mascon distributions. This ambiguity was expressed, for example, in estimations that converged to negative values. As the mascons are correlated, a positive mass can, for example, correct for a negative mass to obtain the felt acceleration. It was shown that such estimated gravity field, which does not represent the real mass-distribution in the asteroid, can represent the real gravity field more accurate than a gravity field estimation with values that could represent the real mass-distribution. This emphasizes that the found solution does not limit the state estimation inside the Brillouin sphere.

An important assumption that was made are the noisy position measurements, what makes it a loosely coupled system. By choosing not to model the spacecraft sensors, the found results are different from the expected results during a real mission. Simulating the sensors would make the measurement accuracy, for example, be dependent on the spacecraft attitude with respect to the asteroid attitude. However, the performed study, using the ’ideal situation’ of measurements with a known noise, eliminates this measurement accuracy variation, what helps in understanding dependencies of state estimation using the mascon model but represents reality less.

It should also be mentioned that the acquired performance has been obtained assuming a known solar radiation pressure and rotational rate of the asteroid. A next step would be to also estimate these properties and analyze the influence of these additions to the estimation performance. As the solar radiation also depends on the spacecraft attitude, the spacecraft’s attitude could, for example, be estimated using appropriate sensors.

Also, it should be kept in mind that the tuning is done with human interpretation and can possibly be improved further by optimization. However, the used trial and error method appeared to be a suitable option to obtain the desired results.

From the performed analysis, it is experienced that it requires effort to take gained information from estimation when increasing model precision. Thereby, when it is required to obtain mass distributions relatable to real masses, human interference is most likely required. This makes the model less suitable for autonomous navigation, as this requires minimal human interference.

6

Conclusions and Recommendations

During this study, the steps taken are performed to be able to answer the research questions defined in chapter 1. In this chapter, the research done is reflected on. In section 6.1, the main research question is answered with the help of its sub-questions. Since this study has a scope in, for example, time, there are points of improvement. As a result of these points of improvement and follow-up questions risen during this thesis, recommendations are formalized in section 6.2.

6.1. Conclusion

To evaluate the performance of the mascon gravity model implemented in a navigation system, an Extended Kalman Filter has been designed and tested among different circumstances. The gravitational parameters of these mascons representing the asteroid's gravity field are estimated by the EKF, along with the spacecraft's position and velocity. The benefit of this gravity model is that it does converge below the body's circumscribing sphere, while the commonly used spherical harmonics model does not.

The dependencies of the EKF performance on the number of point masses and orbit characteristics were analyzed by defining a real world with a target body modeled as a mascon model, whose mascon positions are equal to the model defined in the EKF. The EKF uses noisy position measurements. From covariance analysis, it appeared that models of three or more mascons give a lower estimated variance with a higher inclination because of a higher coverage. Thereby, central mascons between other mascons closer to the spacecraft resulted in higher uncertainties. From covariance analysis, strong correlations between the point masses are found. The correlations between the mascons can approach perfect correlation.

To test the EKF in a more realistic situation, the spacecraft is simulated around a polyhedron model of asteroid 433 Eros. This created a discrepancy between the real gravity field and the gravity field modeled in the filter. At high altitude, a lower precision in the implemented gravity model is required and a model consisting of one or two point-masses could suffice. When getting closer to the asteroid, this model should be increased as higher order terms in the gravity field of the asteroid have more impact on the spacecraft's trajectory. From analysis, the defined mascon positions appear to have a major influence on the estimated distribution. As a distribution of eight point masses resulted in solutions with a wide range of mascon masses from negative masses up to 30% of the total mass, the other distribution gave values corresponding to more realistic density ranges. Nevertheless, the seemingly unrealistic estimated mass distribution can be closer to the real polyhedron gravity field than the distribution with more realistic estimated values. However, these solutions with a high range of masses take a much longer time to converge to its final distribution with respect to the fast converging solution towards the seemingly realistic density values.

The EKF can handle asteroids with a non-uniform density. To test this ability, the asteroid polyhedron model has been divided into mass elements. Each mass element is assigned a density according to the Matérn Covariance function, which is dependent on the distance between the elements. This covariance function provides a smoothed density distribution inside the asteroid body. The polyhedron gravity model has been altered such that it includes each element with specific density. Comparing the estimated distributions for the heterogeneous asteroid with the homogeneous estimated distribution gave a similar change in density distribution as assigned to the heterogeneous asteroid.

Finally, the performance of the EKF is assessed by comparing the estimated gravity field after 10^7 seconds at 45 kilometers with the degree and order 8 spherical harmonics gravity field. The estimated gravity field using a mascon model with 64 point masses placed according to the shape of Eros was more accurate with respect to the defined real polyhedron gravity field than the eighth degree and order gravity field of Eros with respect to the fifteenth degree and order gravity field.

With the findings of the previous chapter, the research questions are answered below:

a) **What is the best approach to implement the mascon gravity field model during a multi-phase mission.**
During the research, a stepwise approach is performed decreasing the altitude and increasing the defined number of point-masses. Multiple orbit inclinations were combined for each mission phase. In general a higher inclination appeared to give a smaller variance. As, for a low number of mascons, the estimated values can vary somewhat over orbit characteristics, it is advised to not increase the model precision directly after lowering altitude. The found estimations can be used as initial model gravitational parameter values for the next step in the mission. One should not set these parameter values fixed, as changing altitude can give different estimated values due to the discrepancy between the set gravity field model and real-world gravity field.

The mascon model definition can depend on the objectives of the mission, since the defined positions of the mascons influence the range of estimated gravitational parameters. If it is desired to gather information about the asteroid's interior, it could be beneficial to use mascon models that result in relatable values for the gravitational parameters. From a different perspective, if an as accurate as possible distribution is desired, it could be beneficial to use the mascon model that converges to a distribution not directly relatable to a mass distribution, but representing the asteroid gravity field more accurate.

b) **What is the effect of gravity field estimation on the accuracy and convergence speed of the estimation?**
Gravity field estimation clearly showed an increase of accuracy in the expected gravitational acceleration, on which the velocity and position estimation depend. As a more precise gravity field model enables the estimation filter to rely more on its dynamical model, the effect of measurement errors can be reduced further.

As not estimating the gravity field would apply a constant environmental model. The errors of this model with reality would remain constant and become more dominant when getting closer to the asteroid. This would require the filter to become more and more dependent on its measurements, which have limited accuracy. For example, when assuming a single point-mass model as asteroid gravity field in the estimation filter would give no large issues when at large distance from the asteroid as the higher order terms do not alter the orbit of the spacecraft significantly. However, when getting closer to the asteroid, its deviation from a single point-mass has a higher influence on the spacecraft's orbit. For example, estimating the gravity field using the mascon model consisting of 64 masses resulted in a gravity field, which had a mean-absolute error with the used Eros polyhedron model at 20 kilometer of about 50 times smaller than that of a single point mass. As a consequence of such large error in the not-estimated gravity field, the a-priori estimation error becomes larger, what would require the filter to be more dependent on its measurements in order to not have a diverging estimation.

As the point-masses are correlated, the total mass is estimated quickly. Because of this, the convergence time in position and velocity is not altered much when increasing model precision. On the contrary, gravitational parameter estimations can take a long time in reaching their final solution. In general, the convergence time increases with model precision. However, this convergence time also depends on the mascon positions. Some mascon models converge to a less stable optimum, what causes the filter to take longer to converge towards a final distribution.

c) **How does heterogeneity influence the estimation performance?**
The EKF appeared capable of handling heterogeneous asteroid distributions. No difference was observed between estimation in orbit around asteroids with a homogeneous or heterogeneous density distribution.

As the gravity field is related to the mass distribution of an asteroid, the estimated mascon model can be used to develop expectations and possibly put constraints on the density distribution inside the asteroid body. Unfortunately, the conversion from the mascon model to a density distribution along the polyhedron shape appeared not to be straightforward. This is due to the ambiguity and the mass distribution.

A suggested approach is to compare the estimated gravitational parameters with the estimated gravitational parameters from simulation around a homogeneous polyhedron model. Comparing the estimated gravitational parameters from a simulated orbit around a heterogeneous asteroid with the estimated values from a simulated orbit around a homogeneous asteroid gave promising results. The mass difference between the two estimations did correspond with the defined mass distribution in the heterogeneous asteroid. Unfortunately, this only worked for a mascon model that converges to values relatable to real masses. Therefore, although the promising results, it cannot be concluded that the estimated mascon distributions can be directly linked to the density distribution inside the asteroid body.

With these answers on the sub-questions, the main research question is answered below:

Can the implementation of the mascon gravity field model for estimation make autonomous navigation more robust inside the Brillouin sphere of a heterogeneous asteroid?

In this thesis, it is shown the EKF using the mascon model converges inside the Brillouin sphere. This ability of the model is beneficial in comparison with the spherical harmonics model.

Whether this model is suitable for autonomous navigation cannot be concluded. Autonomous navigation requires the system to be able to navigate without human interference. The mascon model appeared to be dependent on the chosen mascon positions and would benefit from interim human evaluation. Thereby, a shape model is required to include the asteroid's shape into the mascon model. Such model could be made preliminary to the mission, but can be made more precise using optical measurements from the mission.

The polyhedron model is often used for the mission phases going inside this circumscribing sphere. However, this model is computationally expensive in comparison with other gravity models. In earlier research by Chanut et al. (2015), it was already shown the mascon model can reduce the computational time significantly. The computational time using the mascon model depends on the number of mascons defined to model the asteroids. The higher the number of mascons, the more computationally expensive the model is. Therefore, the precision of the model can be adjusted to a required accuracy. The polyhedron gravity model assumes a constant density in the complete asteroid. As no difference between the performance of the EKF near a homogeneous or heterogeneous asteroid density distribution is shown during this thesis, it is demonstrated that another benefit of the mascon model, with respect to the polyhedron model, is the ability to include heterogeneity.

6.2. Recommendations

Below, recommendations for further research, arisen due to lack of time are given.

Changes to the model:

- As stated in the discussion, the sensors are not simulated. To obtain a realistic assessment of the expected navigation system performance during an asteroid mission, required sensors shall be modeled.
- To decrease computational time and increase precision, the spherical harmonics and mascon model could be combined. In Wittick and Russell (2019) such hybrid model was studied for Eros, what gave promising results. This could be an extension on the mascon model as modeled for this thesis.
- The SRP, spacecraft attitude and asteroid rotation shall be included in the estimation, as this will be required for a real mission. Also, the gravity gradient torque shall be included in the simulation as it influences the rotation. Especially, when getting very close to the asteroid.
- The asteroid rotation is now modeled as a rotation around its z-axis at a constant rate. As heterogeneity could influence this rotation, the effect of heterogeneity shall be investigated. For example, knowledge about the rotational axis and the center of figure of the shape model could acquire some initial estimation of the rate of heterogeneity in the density distribution.
- As the designed heterogeneous polyhedron model for the simulator is very expensive in terms of CPU time, this method shall be improved or possibly simplified to an extend that is acceptable.
- The system can be extended by including a guidance and control system. Because of the relatively low gravitational attraction of asteroids, this can be required to stay in orbit around the target body. Thereby, asteroids often rotate relatively fast. To decrease altitude towards inside the Brillouin sphere could require a guidance and control system to not hit the asteroid body.
- The EKF should be assessed on its CPU efficiency. As the computational load increases with the number of mascons defined, it should be investigated what precision the system could reach, while satisfying requirements on CPU effort.

Additional analysis

- The system should be analyzed around bodies with a different mass, shape and semi-major axis. For example, an interesting use case could be Itokawa, which is expected to have some density differences.
- The system should be tested on the dependency of the measurement time step. As the measurements during the estimation were given as input each evaluation step (1 second), the influence on the system with a different measurement input frequency as the estimation frequency should be evaluated. Also, the time step of estimation can be varied for further analysis.
- The tuning of the filter shall be analyzed further. As the process noise matrix is now assumed as a diagonal matrix, it could possibly be improved further by adding noises to the non-diagonal elements.
- The model performance should be assessed during a landing-phase or Touch-And-Go phase. Since this analysis is limited to reaching the Brillouin sphere, the question remains whether it can reach the required accuracy to properly travel down to the surface.

Additional work

- As only the UKF and EKF were evaluated in the choice for a navigation filter, it is not sure whether the EKF is the most suitable filter. Therefore, it should be evaluated what filter is the best performing filter for missions towards asteroids.
- It shall be studied how density differences inside asteroids can best be modeled. For example, it shall be studied how so-called void spaces are present in asteroids. The system can then be tested on such different realistic situations.
- To relate the estimated masses with the real-world polyhedron model, a way to connect these models shall be studied.
- An algorithm should be designed which gradually increases the mascon model precision and could be applied autonomously. As during a real mission, the shape model will possibly be inaccurate or not available at all, a method to develop the mascon model over time should be developed.
- It should be studied how to implement a constrained Kalman filter properly to obtain mass distributions directly giving information about the inner mass distribution in the asteroid.
- To optimize the tuning process, an optimization algorithm could be designed.
- Since the mascon position definitions influences the mascon performance, this position could possibly be estimated or given some sort of degree of freedom. It should be studied whether this can increase the performance of the model.

Bibliography

Antreasian, P.G., Chesley, S.R., Miller, J.K., Bordi, J.J., and Williams, B.G. (2002). The design and navigation of the near Shoemaker landing on Eros. *Advances in the Astronautical Sciences*, *109 II*, 01–372.

Bachoc, F. (2013). *Parametric estimation of covariance function in Gaussian-process based Kriging models. Application to uncertainty quantification for computer experiments* (Doctoral dissertation). Université Paris-Diderot. Paris. https://tel.archives-ouvertes.fr/tel-00881002

Bolatti, D. (2020). *Spacecraft Orbit-Attitude Coupled Dynamics in Close Proximity to Small-Bodies* (Doctoral dissertation). Ryerson University. Toronto, Canada.

Bourgeaux, A. (2020). Autonomous estimation of the gravity field for asteroid missions. (MSc Thesis).

Brophy, J.R., et al. (2014). Synergies of Robotic Asteroid Redirection Technologies and Human Space Exploration. *65th International Astronautical Congress*, IAC-14.A5.3–B3.6.7, x26388.

Bus, S. (2002). Phase II of the Small Main-Belt Asteroid Spectroscopic Survey A Feature-Based Taxonomy. *Icarus*, *158*(1), 146–177.

Chanut, T.G.G., Aljbaae, S., and Carruba, V. (2015). Mascon gravitation model using a shaped polyhedral source. *Monthly Notices of the Royal Astronomical Society*, *450*(4), 3742–3749.

Chanut, T.G.G., Winter, O.C., and Tsuchida, M. (2014). 3D stability orbits close to 433 Eros using an effective polyhedral model method. *Monthly Notices of the Royal Astronomical Society*, *438*(3), 2672–2682.

Consolmagno, G., Britt, D., and Macke, R. (2008). The significance of meteorite density and porosity. *Geochemistry*, *68*(1), 1–29.

Furfaro, R., Barocco, R., Linares, R., Topputo, F., Reddy, V., Simo, J., and Le Corre, L. (2021). Modeling irregular small bodies gravity field via extreme learning machines and Bayesian optimization. *Advances in Space Research*, *67*(1), 617–638.

Gaskell, R.W., et al. (2008). Characterizing and navigating small bodies with imaging data. *Meteoritics & Planetary Science*, *43*(6), 1049–1061.

Gaskell, R. (2008). Gaskell Eros Shape Model V1.0. *NASA Planetary Data System*, NEAR-A-MSI-5-EROSSHAPE–V1.0.

Gil-Fernandez, J., and Ortega-Hernando, G. (2018). Autonomous vision-based navigation for proximity operations around binary asteroids. *CEAS Space Journal*, *10*(2), 287–294.

Haykin, S. (2001). Kalman Filters. *Kalman filtering and neural networks* (pp. 1–20). John Wiley & Sons, Inc.

Hechler, M. (1997). ROSETTA mission design. *Advances in Space Research*, *19*(1), 127–136.

Hesar, S.G., Scheeres, D.J., McMahon, J.W., and Takahashi, Y. (2016). Surface proximity gravitational field analysis of the asteroid 433 Eros. *Advances in the Astronautical Sciences*, *157*.

Hofmann-Wellenhof, B., and Moritz, H. (2006). *Physical Geodesy*. Springer Vienna.

Julier, S., and Uhlmann, J. (2004). Unscented Filtering and Nonlinear Estimation. *Proceedings of the IEEE*, *92*(3), 401–422.

Kanamaru, M., and Sasaki, S. (2019). Estimation of Interior Density Distribution for Small Bodies: The Case of Asteroid Itokawa. *Transaction of the Japan Society for Aeronautical and Space Sciences, Aerospace Technology Japan*, *17*(3), 270–275.

Kanamaru, M., Sasaki, S., and Wieczorek, M. (2019). Density distribution of asteroid 25143 Itokawa based on smooth terrain shape. *Planetary and Space Science*, *174*, 32–42.

Kato, T., and van der Ha, J.C. (2012). Precise modelling of solar and thermal accelerations on Rosetta. *Acta Astronautica*, *72*, 165–177.

Kubota, T., Hashimoto, T., Kawaguchi, J., Uo, M., and Shirakawa, K. (2006). Guidance and Navigation of Hayabusa Spacecraft for Asteroid Exploration and Sample Return Mission. *2006 SICE-ICASE International Joint Conference*, 2793–2796.

Lissauer, J.J., and de Pater, I. (2013). *Fundamental Planetary Science*. Cambridge University Press.

Margot, J., Pravec, P., Taylor, P., Carry, B., and Jacobson, S. (2015). Asteroid Systems: Binaries, Triples, and Pairs. *Asteroids iv*. University of Arizona Press.

Markley, F.L., and Crassidis, J.L. (2014). *Fundamentals of Spacecraft Attitude Determination and Control*. Springer New York.

Mastrodemos, N., Rush, B., Vaughan, A., and Owen, W. (2011). Optical Navigation For The Dawn Mission At Vesta. *Advances in the Astronautical Sciences*, *140*.

Michel, P., DeMeo, F.E., and Bottke, W.F. (2015). Asteroids: Recent Advances and New Perspectives. *Asteroids iv*. University of Arizona Press.

Michel, P., et al. (2018). European component of the AIDA mission to a binary asteroid: Characterization and interpretation of the impact of the DART mission. *Advances in Space Research*, *62*(8), 2261–2272.

Miller, J., et al. (2002). Determination of Shape, Gravity, and Rotational State of Asteroid 433 Eros. *Icarus*, *155*(1), 3–17.

Montenbruck, O., and Gill, E. (2000). *Satellite Orbits* (Vol. 1). Springer Berlin Heidelberg.

Mooij E. (2019). *AE4870B - Re-entry Systems (Lecture notes)*. Astrodynamics; Space Missions, Delft University of Technology.

Musoff, H., and Zarchan, P. (2009). *Fundamentals of Kalman Filtering: A Practical Approach, Third Edition*.

Nelson, M.L., Britt, D.T., and Lebofsky, L.A. (1993). Review of Asteroid Composition. *Resources of Near Earth Space*, 493–522.

Ngoc, T.T., Khenchaf, A., and Comblet, F. (2019). Evaluating Process and Measurement Noise in Extended Kalman Filter for GNSS Position Accuracy. *13th European Conference on Antennas and Propagation, EuCAP 2019*, 18775798.

Park, R.S., Werner, R.A., and Bhaskaran, S. (2010). Estimating Small-Body Gravity Field from Shape Model and Navigation Data. *Journal of Guidance, Control, and Dynamics*, *33*(1), 212–221.

Razgus, B. (2016). Relative Navigation in Asteroid Missions Dual Quaternion Approach. (MSc Thesis).

Razgus, B., Mooij, E., and Choukroun, D. (2017). Relative Navigation in Asteroid Missions Using Dual Quaternion Filtering. *Journal of Guidance, Control, and Dynamics*, *40*(9), 2151–2166.

Scheeres, D.J. (1999). Satellite Dynamics about Small Bodies: Averaged Solar Radiation Pressure Effects. *The Journal of the Astronautical Sciences*, *47*(1-2), 25–46.

Scheeres, D.J., et al. (2020). Heterogeneous mass distribution of the rubble-pile asteroid (101955) Bennu. *Science Advances*, *6*(41), eabc3350.

Siddiqi, A.A. (2018). *Beyond Earth: A Chronicle of Deep Space Exploration, 1958-2016* (Second). National Aeronautics; Space Administration, Office of Communications, NASA History Division.

Simon, D. (2010). Kalman filtering with state constraints: a survey of linear and nonlinear algorithms. *IET Control Theory & Applications*, *4*(8), 1303–1318.

St-Pierre, M., and Gingras, D. (2004). Comparison between the unscented kalman filter and the extended kalman filter for the position estimation module of an integrated navigation information system. *IEEE Intelligent Vehicles Symposium, 2004*, 831–835.

Takahashi, Y., Scheeres, D.J., and Werner, R.A. (2013). Surface Gravity Fields for Asteroids and Comets. *Journal of Guidance, Control, and Dynamics*, *36*(2), 362–374.

Thor, R. (2016). Mapping the thickness of the Martian elastic lithosphere using maximum likelihood estimation. (MSc Thesis).

Ungarala, S., Dolence, E., and Li, K. (2007). Constrained Extended Kalman Filter For Nonlinear State Estimation. *IFAC Proceedings Volumes*, *40*(5), 63–68.

Wakker, K.F. (2015). *Fundamentals of Astrodynamics*. Institutional Repository, Library, Delft University of Technology.

Wan, E., and Van Der Merwe, R. (2000). The unscented Kalman filter for nonlinear estimation. *Proceedings of the IEEE 2000 Adaptive Systems for Signal Processing, Communications, and Control Symposium (Cat. No.00EX373)*, 153–158.

Welch, G., and Bishop, G. (2001). An Introduction to the Kalman Filter. *Siggraph 2001 course 8* (p. 41). University of North Carolina at Chapel Hill, Department of Computer Science.

Werner, R.A. (1997). Spherical harmonic coefficients for the potential of a constant-density polyhedron. *Computers & Geosciences*, *23*(10), 1071–1077.

Werner, R., and Scheeres, D. (1997). Exterior gravitation of a polyhedron derived and compared with harmonic and mascon gravitation representations of asteroid 4769 Castalia. *Celestial Mechanics and Dynamical Astronomy*, *65*, 313–344.

Wie, B. (2008). *Space Vehicle Dynamics and Control, Second Edition*. American Institute of Aeronautics; Astronautics.

Williams, B., et al. (2018). OSIRIS-REx Flight Dynamics and Navigation Design. *Space Science Reviews*, *214*(4), 69.

Williams, B.G. (2002). Technical challenges and results for navigation of NEAR Shoemaker. *Johns Hopkins APL Technical Digest (Applied Physics Laboratory)*, *23*(1), 34–45.

Wittick, P.T., and Russell, R.P. (2019). Mixed-model gravity representations for small celestial bodies using mascons and spherical harmonics. *Celestial Mechanics and Dynamical Astronomy*, *131*(7), 31.

Yeomans, D.K., et al. (2000). Radio Science Results During the NEAR-Shoemaker Spacecraft Rendezvous with Eros. *Science*, *289*(5487), 2085–2088.

Yoshimitsu, T., Kawaguchi, J., Hashimoto, T., Kubota, T., Uo, M., Morita, H., and Shirakawa, K. (2009). Hayabusa-final autonomous descent and landing based on target marker tracking. *Acta Astronautica*, *65*(5-6), 657–665.

A

Appendix

A.1. EKF Equations

Knowing the equations of motion of the dynamical model of the estimator, which is repeated below:

$$\mathbf{a}_{total} = \ddot{\mathbf{r}} = \mathbf{a}_{g,mascon} + \mathbf{a}_{SRP} + \mathbf{a}_{g,Sun}, \tag{A.1}$$

the elements of Jacobian matrix **G** can be derived. The equation for this Jacobian matrix is also repeated below:

$$\mathbf{G} = \frac{\partial \mathbf{g}(\mathbf{x})}{\partial \mathbf{x}} = \begin{bmatrix} 0 & 0 & 0 & 1 & 0 & 0 & 0 & \dots & 0 \\ 0 & 0 & 0 & 0 & 1 & 0 & 0 & \dots & 0 \\ 0 & 0 & 0 & 0 & 0 & 1 & 0 & \dots & 0 \\ \frac{\partial a_x}{\partial x} & \frac{\partial a_x}{\partial y} & \frac{\partial a_x}{\partial z} & 0 & 0 & 0 & \frac{\partial a_x}{\partial \mu_1} & \dots & \frac{\partial a_x}{\partial \mu_{N-6}} \\ \frac{\partial a_y}{\partial x} & \frac{\partial a_y}{\partial y} & \frac{\partial a_y}{\partial z} & 0 & 0 & 0 & \frac{\partial a_y}{\partial \mu_1} & \dots & \frac{\partial a_y}{\partial \mu_{N-6}} \\ \frac{\partial a_z}{\partial x} & \frac{\partial a_z}{\partial y} & \frac{\partial a_z}{\partial z} & 0 & 0 & 0 & \frac{\partial a_z}{\partial \mu_1} & \dots & \frac{\partial a_z}{\partial \mu_{N-6}} \\ 0 & 0 & 0 & 0 & 0 & 0 & 0 & \dots & 0 \\ \vdots & \vdots & \vdots & \vdots & \vdots & \vdots & \vdots & \ddots & \vdots \\ 0 & 0 & 0 & 0 & 0 & 0 & 0 & \dots & 0 \end{bmatrix}_{[N\times N]} \tag{A.2}$$

As the acceleration due to SRP is assumed known and given to the system as a constant. The derivative of the accelerations can be split into two parts: the derivative of the asteroid gravity and that from the Sun as follows:

$$\frac{\partial \mathbf{a}}{\partial \mathbf{x}} = \frac{\partial \mathbf{a}_{g,mascon}}{\partial \mathbf{x}} + \frac{\partial \mathbf{a}_{g,Sun}}{\partial \mathbf{x}} \tag{A.3}$$

Here, the derivatives of the mascon model are:

$$\frac{\partial a_{g,m}}{\partial r_m} = \sum_{i=1}^{N} \mu_i \left(3\frac{(r_m - r_{i,m})^2}{||(\mathbf{r}-\mathbf{r}_i)||^5} - \frac{1}{||(\mathbf{r}-\mathbf{r}_i)||^3} \right) \tag{A.4}$$

$$\frac{\partial a_{g,m}}{\partial r_n} = \sum_{i=1}^{N} 3\mu_i \frac{(r_m - r_{i,m})(r_n - r_{i,n})}{||(\mathbf{r}-\mathbf{r}_i)||^5} \tag{A.5}$$

where $m, n \in \{1, 2, 3\}$ indicating the element of the position vector $\mathbf{r} = (x\ y\ z)^T$ and acceleration vector $\mathbf{a} = (a_x\ a_y\ a_z)^T$, and N is the length of the state. The derivatives of the third body perturbation by the Sun is given by:

$$\frac{\partial a_{g,m}}{\partial r_m} = \mu_{Sun} \left(3\frac{(r_{m,Sun} - r_m)^2}{||\mathbf{r}_{Sun}-\mathbf{r}||^5} - \frac{1}{||\mathbf{r}_{Sun}-\mathbf{r}||.^3} \right) \tag{A.6}$$

$$\frac{\partial a_{g,m}}{\partial r_n} = 3\frac{\mu_{Sun}(r_{m,Sun} - r_m)(r_{n,Sun} - r_n)}{||\mathbf{r}_{Sun} - \mathbf{r}||^5} \tag{A.7}$$

The derivatives of the acceleration towards the gravitational parameters are:

$$\frac{\partial a_m}{\partial \mu_i} = -\frac{1}{||\mathbf{r} - \mathbf{r}_i||^3}(r_m - r_{i,m}) \tag{A.8}$$

A.2. Tuning

In this section the values for the process covariance matrix are given. The process covariance matrix is defined as:

$$\mathbf{Q} = \begin{bmatrix} \mathbf{I}_{3\times3}\cdot\sigma_1^2 & 0 & 0 \\ 0 & \mathbf{I}_{3\times3}\cdot\sigma_2^2 & 0 \\ 0 & 0 & \mathbf{I}_{3\times3}\cdot\sigma_3^2 \end{bmatrix} \tag{A.9}$$

Where the values of σ_i are tuned till a convenient estimation performance. It is observed that σ_2 has the most influence on the estimation. For the other two scalar values, it appeared that these should be given a sufficient low value, such that σ_2 could be tweaked till convenience.

Table A.1: Tuning values for process noise matrix **Q**.

Orbit radius	**number of mascons**	σ_1^2	σ_2^2	σ_3^2	ν_r
200	1	$1{\cdot}10^{-7}$	$5{\cdot}10^{-12}$	$1{\cdot}10^{-15}$	100
	2	$1{\cdot}10^{-14}$	$1{\cdot}10^{-12}$	$1{\cdot}10^{-18}$	100
	3	$1{\cdot}10^{-14}$	$1{\cdot}10^{-12}$	$1{\cdot}10^{-18}$	100
	4	$1{\cdot}10^{-7}$	$8{\cdot}10^{-13}$	$1{\cdot}10^{-5}$	100
	8	$1{\cdot}10^{-7}$	$5{\cdot}10^{-13}$	$1{\cdot}10^{-5}$	100
50	1	$1{\cdot}10^{-7}$	$1{\cdot}10^{-7}$	$1{\cdot}10^{-5}$	100
	2	$1{\cdot}10^{-7}$	$5{\cdot}10^{-8}$	$1{\cdot}10^{-5}$	100
	3	$1{\cdot}10^{-7}$	$3{\cdot}10^{-8}$	$1{\cdot}10^{-5}$	100
	4	$1{\cdot}10^{-7}$	$1{\cdot}10^{-8}$	$1{\cdot}10^{-5}$	100
	8	$1{\cdot}10^{-7}$	$5{\cdot}10^{-9}$	$1{\cdot}10^{-5}$	100
35	1	$1{\cdot}10^{-7}$	$5{\cdot}10^{-6}$	$1{\cdot}10^{-5}$	100
	2	$1{\cdot}10^{-7}$	$5{\cdot}10^{-7}$	$1{\cdot}10^{-5}$	100
	3	$1{\cdot}10^{-7}$	$3{\cdot}10^{-7}$	$1{\cdot}10^{-5}$	100
	4	$1{\cdot}10^{-7}$	$1{\cdot}10^{-7}$	$1{\cdot}10^{-5}$	100
	8	$1{\cdot}10^{-7}$	$7{\cdot}10^{-8}$	$1{\cdot}10^{-5}$	100
15	8	$1{\cdot}10^{-5}$	$1{\cdot}10^{-6}$	$1{\cdot}10^{-5}$	10
45	64	$1{\cdot}10^{-17}$	$5{\cdot}10^{-12}$	$1{\cdot}10^{-15}$	10

A.3. Additional figures

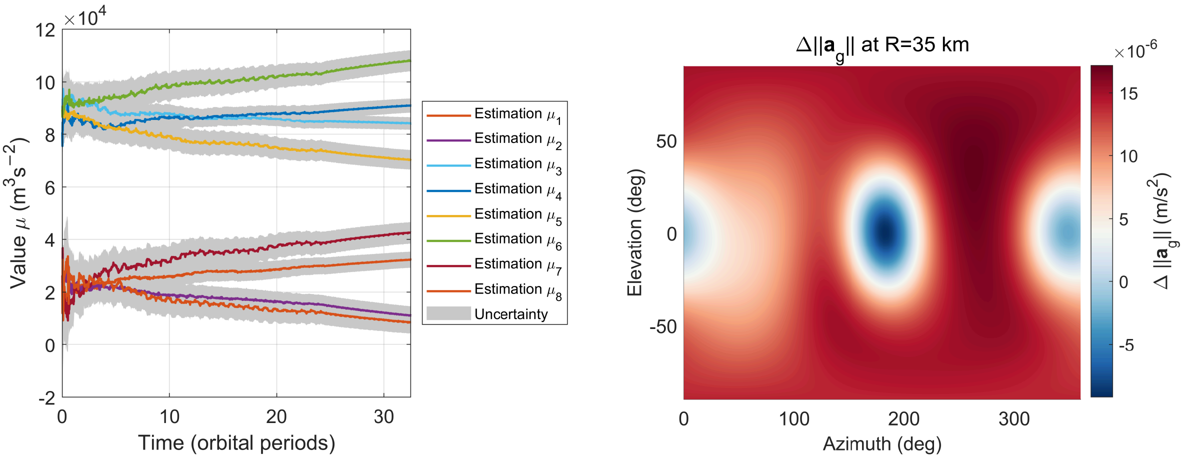

(a) Gravitational parameter estimated value plotted against the time for a 35 kilometer orbit.

(b) Surface plot of the error in the estimated gravity field.

Figure A.1: Gravitational parameter estimation results for asteroid configuration 2 using the CoM-based model.

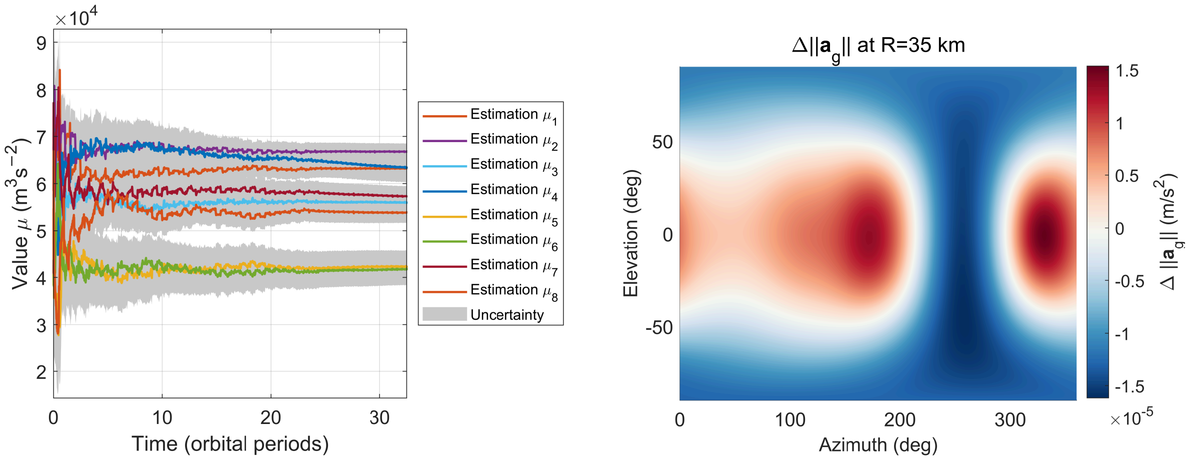

(a) Gravitational parameter estimated value plotted against the time for a 35 kilometer orbit.

(b) Surface plot of the error in the estimated gravity field.

Figure A.2: Gravitational parameter estimation results for asteroid configuration 2 using the chosen model.

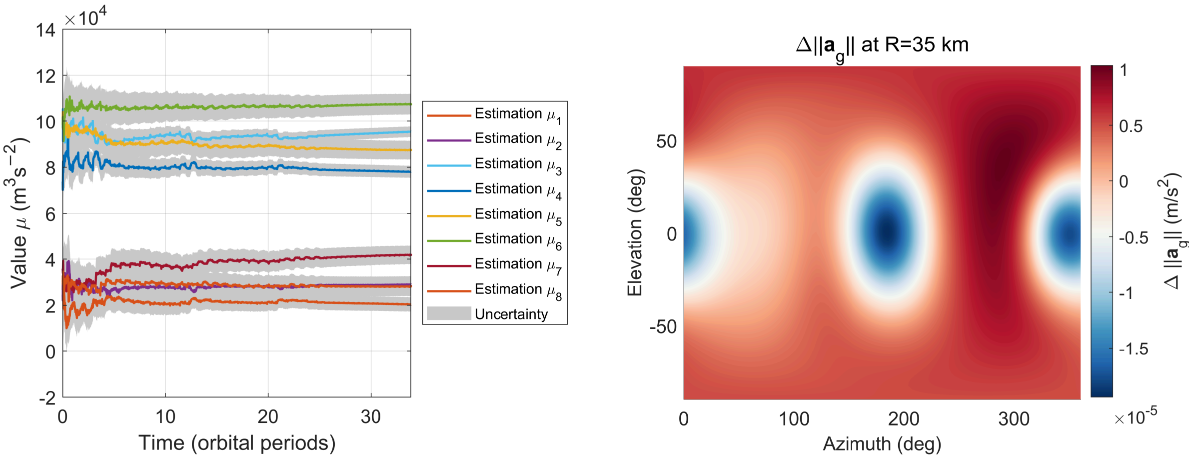

(a) Gravitational parameter estimated value plotted against the time for a 35 kilometer orbit.

(b) Surface plot of the error in the estimated gravity field.

Figure A.3: Gravitational parameter estimation results for asteroid configuration 3 using the CoM-based model.

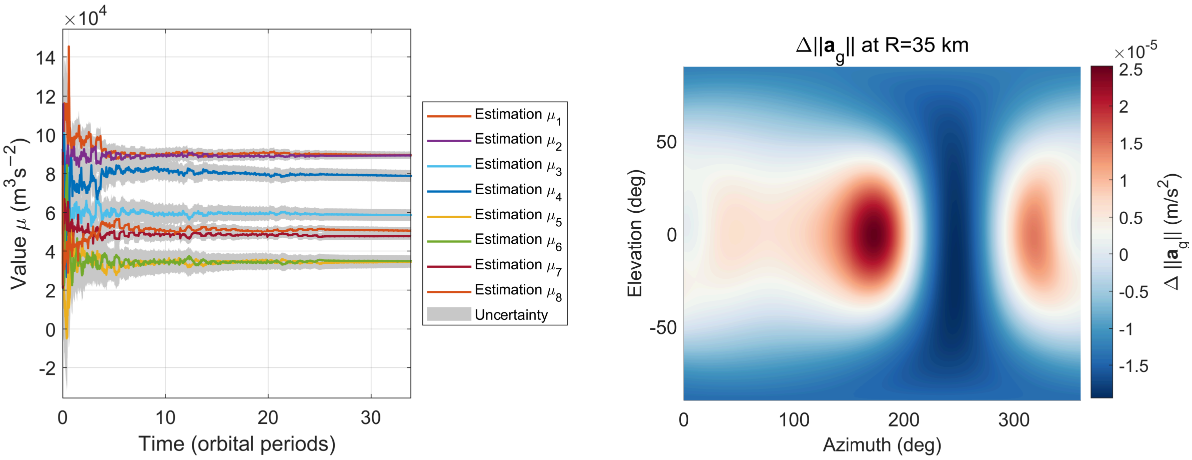

(a) Gravitational parameter estimated value plotted against the time for a 35 kilometer orbit.

(b) Surface plot of the error in the estimated gravity field.

Figure A.4: Gravitational parameter estimation results for asteroid configuration 3 using the chosen model.